Modeling Aeolian Dune and Dune Field Evolution

by

Serina Diniega

A Dissertation Submitted to the Faculty of the

GRADUATE INTERDISCIPLINARY PROGRAM IN APPLIED MATHEMATICS

In Partial Fulfillment of the Requirements
For the Degree of

DOCTOR OF PHILOSOPHY

In the Graduate College

THE UNIVERSITY OF ARIZONA

2 0 1 0

Acknowledgements

First, of course, I thank my advisors. Thank you, Karl, for taking on the dune project so long ago, for showing me how to be a mathematician within an interdisciplinary field, and for teaching me the importance of telling "a good story." Thank you, Shane, for letting me rope you into being my minor advisor and for always finding the time and energy to be my sounding board (and emotion-validator) through a wide range of discussion topics.

I also thank the rest of my committee: Dr. Tabor, thank you for guiding me throughout my graduate career. Kevin, thank you for being my fourth member!

I heartily thank my friends and family for supporting me through all of the tough times. I don't know that I would have made it to this point without you; I do know that I wouldn't have had this much sanity and self-confidence intact without your help. You all were highly influential as I found my path through the rabbit-hole of graduate school and research.

Finally, I thank Abe. Thank you for supplying hugs, food, and footrubs whenever needed; for listening to the frustrated rants, excited research plans, and everything in-between; for encouraging me through the disappointments and for celebrating the accomplishments. In short: thank you, love, for everything.

Dedication

I dedicate this dissertation to my family – the most important part of my life and my primary source of strength and inspiration. In particular, I dedicate this work to the members of the younger generations – I pray that I will provide assistance and support to your life's journey, as was provided to me.

Table of Contents

TABLE OF CONTENTS—*Continued*

TABLE OF CONTENTS—*Continued*

List of Tables

List of Figures

List of Figures—*Continued*

Abstract

sand hops and bounces –
see the dunes grow, run, collide –
form the field's pattern.

Aeolian sand dune morphologies and sizes are strongly connected to the environmental context and physical processes active since dune formation. As such, the patterns and measurable features found within dunes and dune fields can be interpreted as records of environmental conditions. Using mathematical models of dune and dune field evolution, it should be possible to quantitatively predict dune field dynamics from current conditions or to determine past field conditions based on present-day observations.

In this dissertation, we focus on the construction and quantitative analysis of a continuum dune evolution model. We then apply this model towards interpretation of the formative history of terrestrial and martian dunes and dune fields. Our first aim is to identify the controls for the characteristic lengthscales seen in patterned dune fields. Variations in sand flux, binary dune interactions, and topography are evaluated with respect to evolution of individual dunes. Through the use of both quantitative and qualitative multiscale models, these results are then extended to determine the role such processes may play in (de)stabilization of the dune field. We find that sand flux variations and topography generally destabilize dune fields, while dune collisions can yield more similarly-sized dunes. We construct and apply a phenomenological macroscale dune evolution model to then quantitatively demonstrate how dune collisions cause a dune field to evolve into a set of uniformly-sized dunes. Our second goal is to investigate the influence of reversing winds and polar processes in relation to dune slope and morphology. Using numerical experiments, we investigate possible causes of distinctive morphologies seen in Antarctic and martian polar dunes. Finally, we discuss possible model extensions and needed observations that will enable the inclusion of more realistic physical environments in the dune and dune field evolution models.

By elucidating the qualitative and quantitative connections between environmental conditions, physical processes, and resultant dune and dune field morphologies, this research furthers our ability to interpret spacecraft images of dune fields, and to use present-day observations to improve our understanding of past terrestrial and martian environments.

1. INTRODUCTION

Interactions between wind flow, transported granular sediment, and bedform morphology (Figure 1.1) create aeolian landforms which record contemporaneous environmental conditions and processes, over a range of spatial and temporal scales. For example, the sizes and shapes of terrestrial dunes strongly reflect surface and atmospheric conditions throughout their evolution, which can span seasons to decades and decameters to kilometers (Sauermann et al. 2001, Sauermann et al. 2003, Bourke et al. 2009). On much larger scales, the spatial distribution of and complexity within martian and terrestrial dune fields are studied as records of regional conditions over long timescales (Kocurek & Ewing 2005, Bishop 2007, Hayward et al. 2009).

Within the last few decades, much progress has been made towards quantitatively connecting environmental conditions with resultant dune morphology and behavior. This is primarily due to the increased availability of spacecraft images of dune fields on different planetary surfaces, and the development of a detailed continuum dune evolution model. The combination of these two advances has greatly aided dune evolution studies as images of dunes evolving within a range of environmental conditions have allowed for better validation of model assumptions and structures and the application of these models has improved landform image interpretation.

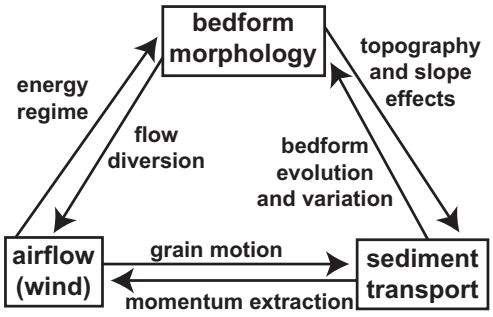

FIGURE 1.1. Interactions and feedbacks that occur in the evolution of an aeolian bedform system (based on a figure in Walker & Nickling 2002). Aeolian bedforms form over a wide range of scales, from ripples (decimeters to meters wavelength) to dunes (decameters to kilometers), to dune fields and mega-dunes.

1.1. Motivation

Dune and dune evolution models have not been able to replicate all observations, however, which limits their use in connecting dune field morphology with environmental conditions. In particular, an important open question remains regarding the equilibrium or maximum size of dunes which creates the uniform dune sizes found within many dune fields (such as the crescentic dunes in White Sands National Monument, New Mexico or the martian dune field shown in Figure 1.2). It is generally accepted that these dune field patterns are indicative of evolution through a process of self-organization (Werner 1995, Kocurek & Ewing 2005, Bishop 2007) towards a steady state.

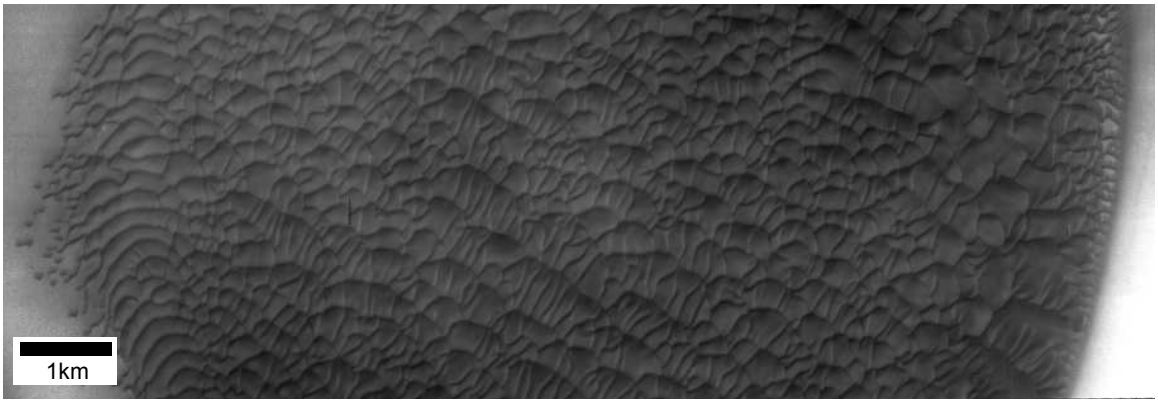

FIGURE 1.2. This image (HiRISE PSP_008628_2515) shows a martian dune field within a crater with two dominant dune sizes (200m and 600m), except for near the boundaries of the field (where topography is probably influencing dune evolution). Such pattern superposition can occur through multiple generations of dune construction and evolution, where in each generation the dune field tends towards a simple pattern through dune interaction (Kocurek & Ewing 2005).

Not all fields are patterned, however. Some fields, such as the Kelso dune field in California or the martian dune field shown in Figure 1.3, show signs of a disrupted initial pattern and scaling, with the majority of dunes being of similar sizes and a few dunes that are significantly larger. It is an open question if this is due to abrupt changes in environmental conditions, a slow and natural evolution within the field conditions or dynamics, or a scale-dependent effect of boundary conditions. Patterns (or lack thereof) within different fields may also result from localized influences and from a combination of processes and conditions.

Despite these complications, a quantitative understanding of how dune field patterns can form (or be disrupted) is needed as this directly relates to assumptions regarding the timescale over which dunes and dune fields record information.

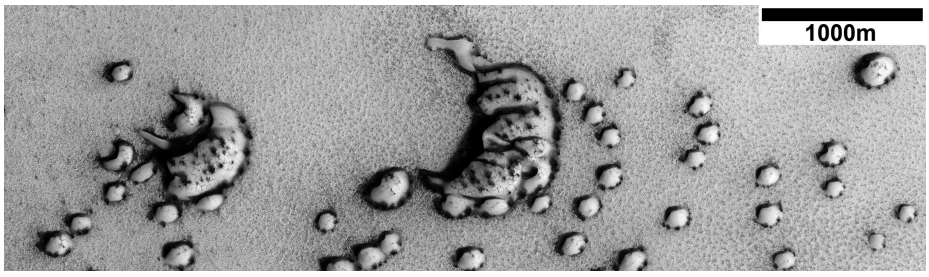

FIGURE 1.3. This image (HiRISE PSP_007172_2570) shows a martian dune field where runaway growth appears to be occuring. Many small, uniform barchan dunes (200m wide) populate this area, interspersed with a small number of large megabarchans (large, central one is ∼1040m wide). All dunes have left-facing slipfaces, suggesting that they formed under the same environmental conditions and were (are?) migrating towards the left. The megabarchans have sinuous crests and multiple slipfaces on the windward slope, suggesting that these dunes formed through collision of the barchans (a hypothesis also put forward by Bourke & Balme (2008)). The areas downwind of the two megabarchans shown are mostly devoid of other dune structures, implying that the collisions are predominantly resulting in coalescence. There are no apparent topographical or environmental reasons for the size disparity between the megabarchans and the barchan dunes.

In this research, we evaluate the influence of topography and dune collisions on dune and dune field evolution. We focus on the identification of characteristic lengthscales, and related environmental or dynamic controls, that may yield a maximum dune size. The conditions under which a dune field will not form similarly-sized dunes, but instead will contain a few that are significantly larger, are also explored.

1.2. Previous Studies

The first rigorous studies of aeolian bedforms were completed by Bagnold (1941) who showed that aeolian sand ripples evolve into bedforms of characteristic spacing and heights, and that these lengthscales are controlled in a consistent manner by grain size and wind conditions. As dunes exhibit similar morphologies and behaviors as ripples, and are formed by the same physical processes, it is assumed that they can be modeled with a similar method. The first full formation and evolution models of dunes utilized a simple cellular automata model of wind-transported sand slabs where each transported slab would move a discrete distance during a time step; this saltation-type motion can be considered the large-scale and average motion of an accumulation of sand (Werner 1995, Momiji et al. 2000, Bishop et al. 2002). These minimal phenomenological models, surprisingly, yielded bedforms with dune shapes

that varied depending on sediment supply and wind variability (Figure 1.4), as observed in nature (Figure 1.5).

Numerical experiments with these discrete models aimed to identify the influence of non-linear effects, such as wind speedup and associated sand flux variations on the upwind slopes. Additional studies attempted to identify characteristic lengthscales within dune fields. Recent work by Pelletier (2009) argued that dunes saturate in size due to feedback between landform-induced surface roughness and saltation flux. Due to the discrete nature of these models, however, it is difficult to quantitatively connect the influence of specific environmental conditions on details of dune morphology, size, and behavior.

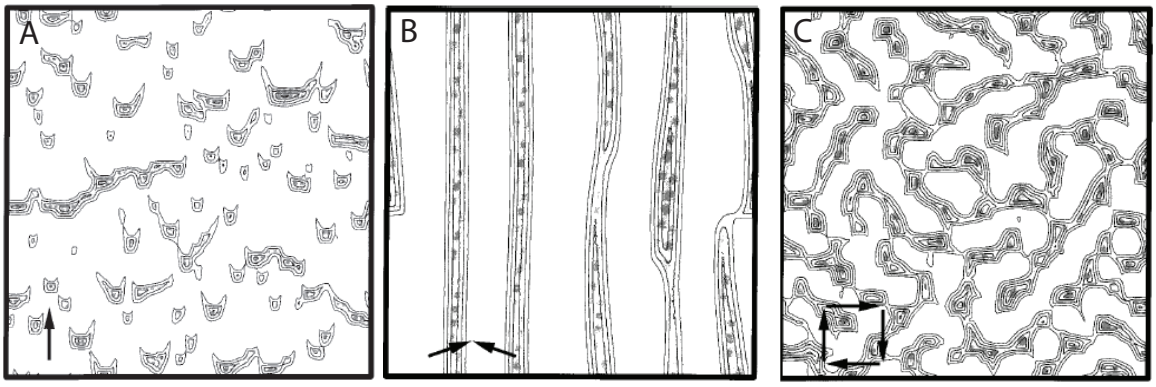

FIGURE 1.4. Dune fields created with a cellular automata model, under differing sequences of transport direction (indicated with arrows). Initial topography in all simulations was random in morphology. A: Simulated barchan dunes form under unidirectional wind. B: Simulated linear dunes form under bi-directional winds. C: Simulated star dunes form under four wind directions. Images taken from Werner (1995).

Continuum models of dune evolution were also developed which considered sand flux over topography and then related that flux to changes in topography (Howard et al. 1978, Stam 1996, Sauermann et al. 2001). The derivation and analysis of model equations allowed model parameters (and environmental conditions) to be quantitatively connected with characteristic landform scales and morphologies, yielding information about the minimum size of dunes (Kroy et al. 2002) and the initial growth of dunes (Andreotti et al. 2002*b*). However, these continuum models did not yield information about the maximum dune size. In fact, numerical simulations showed that dunes will grow without bound unless the sediment supply is limited. Based on these dynamics, Hersen et al. (2004) showed that if dunes interact with each other only through sediment flux, then dunes within that field will have no characteristic maximum lengthscale. Instead, dunes will coalesce, perpetually yielding smaller

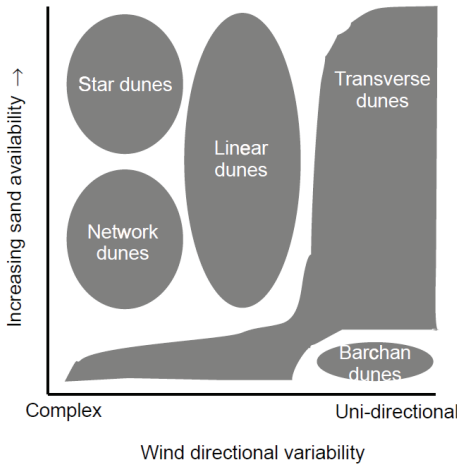

FIGURE 1.5. Diagram showing the dune types/shapes that form in different wind and sand availability regimes. Image is from Bishop et al. (2002).

numbers of larger dunes.

It appears that the largest dunes may be limited in size due to resonances with the atmospheric boundary layer (Andreotti et al. 2009). However, this does not account for the seemingly limited sizes and spacings of smaller dunes. One possibility is that stochastic processes, such as variations in wind strength and direction, may play a role in the stabilization of dune fields by preferentially destabilizing large dunes (Hersen et al. 2004, Elbelrhiti et al. 2005, Elbelrhiti et al. 2008). However, such processes, being stochastic, are difficult to quantify and to incorporate into generic analysis or simulation of dune fields. A study by Werner (1999) attempted to do this, by estimating rates of bedform defect merging and relating this to average dune sizes.

Another mechanism that has been proposed to regulate dune size and spacing, and that depends on sand and dune dynamics broadly common to all dune fields, is dune collision. When dunes collide, sand is redistributed between the dunes. As long as the net sand exchange is from the large to the small dune, it is possible for a dune field to evolve into a patterned structure after many collisions (Hersen & Douady 2005). Some studies have considered the evolution of dune fields through collisions between dunes (Lima et al. 2002, Parteli & Herrmann 2003, Lee et al. 2005) and have created fields containing similarly-sized dunes. However, these models generally rely on ill-defined assumptions and model-specific parameters, making it difficult to generalize their results.

1.3. This Work

In this dissertation, we aim to explore the influence of specific environmental conditions (i.e., sand flux, topography, and reversing winds) and dynamical processes (i.e., binary interactions, aeolian/cold climate process interactions), and to quantitatively connect these influences to dune and dune field morphology. These studies have relied on an iterative combination of model development, analysis, and numerical simulation. Generally, models have been run in non-dimensional space to view the dynamics and morphological trends without bias from environment-specific parameters. The scales are then reintroduced for comparison with observed terrestrial and martian dunes and dune fields.

In Chapter 2, the physical processes and environmental conditions that create dunes and dune fields are reviewed. These processes and environmental conditions are discussed again in Chapter 3 in the form of equations and parameters within the dune evolution model. This section also includes analysis and non-dimensionalization of the dune evolution model equations.

In Chapters 4 through 6, we investigate the influence of processes and environmental conditions on dune size regulation. In Chapter 4, we consider the influence of sand flux on and between dunes. In Chapter 5, we consider the influence of interactions between dunes. In particular, we couple the dune model with a simple, phenomenological dune field model to evaluate the effect dune collisions will have on dune size evolution within a field; most of this content is published in Diniega et al. (2010). Finally, in Chapter 6 we consider the influence of topography on dune migration, and shape and size stability. We do this by evaluating the effect a small hill or step will have on isolated dune evolution and a binary dune collision, and then extending those results to dune field evolution.

In Chapter 7, we consider an application of the dune evolution model, which is extended to include reversing winds and cold climate processes. We present preliminary investigations of the influence these additional processes will have on dune slope evolution. In particular, we aim to understand the formation of distinctive lee slope morphology observed within Antarctic and martian polar dunes.

2. THE PHYSICAL SYSTEM

Aeolian dunes develop whenever there is a source of granular material, wind of sufficient strength to move this material, and an "obstacle" to induce initial accumulation. These landforms have been found on Earth, Mars (e.g., Greeley et al. 2003), Venus (e.g., Greeley et al. 1992), and even the Saturnian satellite Titan (e.g., Lorenz et al. 2006). Dunes can also form underwater and are similar in morphology and behavior to aeolian dunes (Endo, Kobu & Sunamura 2004) after appropriate rescaling (Claudin & Andreotti 2006). In this study, however, we focus exclusively on aeolian dunes.

In this chapter, we briefly explain how dunes form and identify important physical processes and environmental conditions. This will help motivate the model we use to explore dune and dune field dynamics, which is discussed in Chapter 3.

2.1. Dunes and Dune Fields

Dunes are classified based on their large-scale morphology, which has been observed to be strongly correlated with two environmental conditions: the amount of sand available and the variation in wind direction (Figure 1.5). This correspondence indicates that sand flux dynamics and localized sediment and wind conditions are highly influential in determining the shape of dunes, and that these specific dune shapes are "attractor" or equilibrium states (Werner 1995, Hesp & Hastings 1998, Andreotti et al. 2002*a*). This allows dune morphology to be used to infer the environmental conditions during dune formation. Conversely, a lack of correlation between the present environment and a dune shape is indicative of changes in the wind and/or sediment parameters.

However, many dunes have complex shapes and dune fields may consist of superimposed dune forms. To reverse-engineer the environmental conditions throughout the evolutionary age of the dune field from complicated dune and dune field morphology, quantitative models are needed to determine exactly how a dune's size and shape will evolve. Such models are also essential in determining how a dune will respond to changes in the environment and to estimate the temporal and spatial scales of dune adjustment. Finally, models are needed to decouple the effects of changes in localized environmental conditions (e.g., due to natural evolution of sediment supply or seasonal wind variation) versus general dynamic processes (e.g., due to variations in sand flux between dunes as dunes grow and/or collide).

2.1.1. Dunes forming in unidirectional wind flow

The dune and dune field models considered in this study are two-dimensional. This restricts their application to dunes which form in unidirectional wind flow, and neglects processes and forces that occur transverse to the wind direction. In natural environments, even strongly unidirectional wind flow will have some variation, and this may need to be considered when examining detailed dune geomorphology. This study focuses only on general trends and scalings, however, which are assumed to be relatively invariant with respect to slight wind variation and sand flux in the third dimension (when averaged over sufficient time). Three-dimensional models have used to examine more complicated dune forms (Parteli, Schatz & Herrmann 2005, Parteli & Herrmann 2007, Reffet et al. 2010), but these models are usually based on simple extensions of the two-dimensional model (such as two-dimensional slices, coupled through transverse diffusion); it remains to be shown that these simple models adequately reflect the physical three-dimensional effects and processes.

Two dune types form in unidirectional winds: *transverse dunes* and *barchan dunes* (Figure 1.5). Transverse dunes are extensive, linear dunes with crest lines perpendicular to the wind direction; the dominant wind direction can be determined by locating the steeper slope (which faces downwind). These dunes form in regions of high sand supply, with small or non-existent sand-free interdunal areas (sand coverage of $\leq 10\%$; Lancaster 1995). Transverse dunes are found in 40% of terrestrial sand seas and over a majority of martian sand seas (Wiggs 2001, Schwämmle & Herrmann 2004). A reversing dune is a transverse dune that evolves under winds that periodically change direction 180°. Three-dimensional simulations of transverse dunes produce translationally invariant dunes (Schwämmle & Herrmann 2004), so two-dimensional simulations are generally assumed to be sufficient (e.g., unless defects occurring along a dune crestline are of interest; Werner 1999).

Barchan dunes, also known as *crescent dunes*, are often the focus of dune studies as they are one of the smallest dune forms, are often easily accessible by car, and form under "simple" conditions of low sediment supply and unidirectional wind (Andreotti et al. 2002*a*). These dunes are isolated bedforms, with large sand-free interdune areas (Lancaster 1995). Dominant wind direction can be determined easily from their shape, as their horns and their steepest slope point downwind. These dunes have an intrinsically three-dimensional shape (Schwämmle & Herrmann 2005), which causes important differences in sandflux (Hersen 2004) and dune collisions (Gay 1999, Endo, Taniguchi & Katsuki 2004), so care must be taken in applying two-dimensional model results towards the interpretation of these three-dimensional landforms.

2.1.2. Dune geomorphological terminology

The dune's *stoss* slope is the upwind (or windward) slope, and the *lee* slope faces downwind. The dune's *brink* is the location on the lee slope where flow separation

occurs and gravity-driven avalanching becomes the dominant process, causing the slope to abruptly steepen to the angle of repose ($\sim 34^{o}$). The dune surface that is at the angle of repose is called a *slipface*; this surface is always oriented downwind and rapidly adjusts to environmental changes, so is the best indicator of the recent wind direction (Bagnold 1941). The dune *crest* is the highest point on the dune, which does not always coincide with the brink (Schwämmle & Herrmann 2005, Parteli, Schwämmle, Herrmann, Monteiro & Maia 2005, Schatz & Herrmann 2006). These terms are illustrated in Figure 2.1.

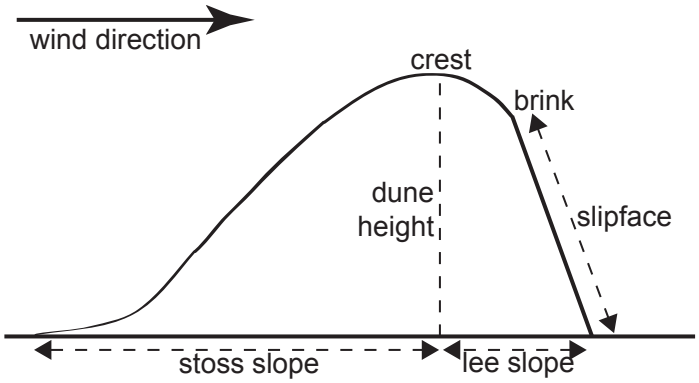

FIGURE 2.1. Schematic diagram illustrating some dune geomorphology terminology.

2.2. Relevant Processes and Environmental Conditions

When out in the field, especially under strong wind conditions, it is apparent that the sand transport is complicated and chaotic. It involves interaction between the (gusty) wind and surficial grains (through wind-exerted shear stress), and between moving grains and the stationary grains/ground (through granular impacts). Since Bagnold (1941), much work has gone into simplifying and averaging these small-scale and fast interactions into quantitative and simple relations between average wind strength and sand flux (e.g., Fryberger 1979, Iversen & Rasmussen 1999, Sorensen 2004). Other studies have then aimed at understanding how sand flux relates to dune evolution (e.g., Howard et al. 1978, van Dijk et al. 1999, Sauermann et al. 2001). Here we briefly outline dominant processes and conditions; we will consider these again in the next chapter as we construct the dune model.

2.2.1. Sand motion

Sand is transported primarily through interactions between the wind and the ground surface. As the wind blows over the sand surface, different sized particles are trans-

ported different distances via several processes (Figure 2.2), resulting in a natural size-sorting within dunes.

Dunes are composed of sand particles ($70 - 500\mu m$; Figure 2.3); in this context, *sand* defines a grain of a specific size (versus a particular composition, etc.) which has the lowest wind-exerted shear stress threshold for motion (Figure 2.4). This natural size-sorting results from the difficulty in moving grains of other sizes: larger particles are more difficult to move due to their higher mass, and smaller particles are more difficult to move due to higher intergrain cohesion (Bagnold 1941). Sand particles are lifted by the wind, but are too large to be kept aloft so are moved downwind via short jumps, in a motion called *saltation*. Impacting saltating grains will impart energy to the ground surface, resulting in additional particles moving in small, randomly-oriented ballistic jumps, in a motion called *reptation* (Lancaster 1995).

Other types of motion (*suspension* of smaller particles and *creep* of larger particles) are neglected in this dune evolution model, as non-sand-sized particles are more difficult to move. Additionally, once small grains (*dust* or *clay*) are suspended, they can be transported distances significantly larger than dunes or dune fields (Uno et al. 2009), and thus are effectively removed from the system.

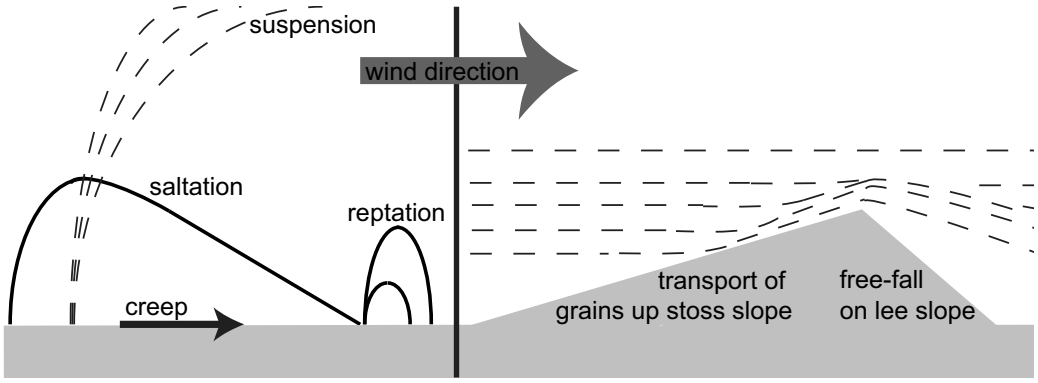

FIGURE 2.2. On the left are schematic illustrations of sediment transport processes. Dunes are primarily made up of sand-sized particles (diameter $\sim 100\mu$m), which are transported via saltation and reptation. On a dune (decameters to a kilometer in length), grains are transported over the brink of the dune by the wind. If the dune is sufficiently large to shelter the lee region and cause airflow separation (the shadow zone), then these grains free-fall onto the upper surface of the lee slope. As this region steepens beyond the angle of repose, small avalanches transport material down-slope – thus, creating a slipface at the angle of repose. These processes give the dune its distinctive, asymmetric shape and move the dune forward.

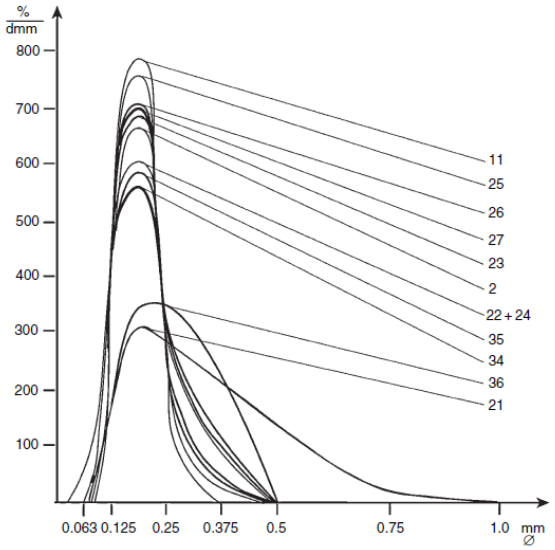

FIGURE 2.3. Diagram illustrating the sharply-peaked and narrowly-supported grain size distribution found within terrestrial dunes (image taken from Besler 2008) that forms due to natural process-driven grain size-sorting. As stated by Besler (2008), "the granulometeric distribution in an aeolian deposit is not a random or an ephemeral property, but represents a proper characteristic of the adjustment to the depositional environment."

2.2.2. Wind velocity profile and shear stress

The wind's shear stress velocity (u_*) quantifies the "strength" of the wind: the shear stress that it exerts upon the ground ($u_* = \sqrt{\tau/\rho_{air}}$, where τ is a scalar – the term within the shear stress tensor that refers to the vertical flux of momentum caused by the horizontal component of stress (σ_{xz})). Over a flat, non-vegetated plane and in conditions of neutral atmospheric stability, u_* is independent of height. It can be related to the wind velocity at a height z, however, via the Prandtl-von Kármán model:

$$u(z) = \frac{u_*}{\kappa} \ln \frac{z}{z_0}, \tag{2.1}$$

where κ is von Kármán's constant (~ 0.4), and z_0 is the aerodynamic roughness length. It is important to note that in natural conditions, such as unsteady winds or sediment transport, the measured wind velocity profiles do not correspond with the log-linear model close to the surface. However, this model is considered sufficiently accurate over long temporal and spatial averaging (Walker & Nickling 2002).

The log-linear model, where u_* and τ are constants in space and time, is also invalid within an internal boundary layer over large topography, as compression and

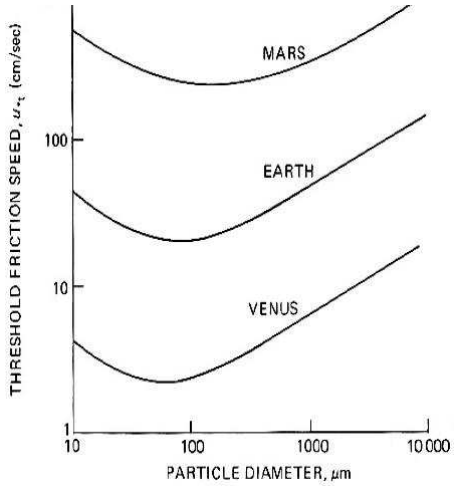

FIGURE 2.4. Diagram showing the shearstress velocity (u_*) needed to move particles of different diameters due to wind-exerted shear stress. This curve has been determined theoretically and empirically on the Earth, and it is assumed that a similar curve will be found on other planets. Note that the shown relation (based on a study by Iversen & White 1982) predicts that martian dune sand should be coarser than terrestrial dune sand, which is consistent with estimates of average grain size from thermal measurements (Edgett & Christensen 1991).

acceleration of airflow will alter the shear stress exerted (Frank & Kocurek 1996*a*): decreasing slightly at the base of a hill due to flow stagnation, and then increasing (up to doubling in magnitude) as it moves upslope towards the crest (Walker & Nickling 2002, Walker & Nickling 2003). This can be corrected by using a modified shear stress ($\tau = \tau_0(1 + \tilde{\tau})$) where the correction factor ($\tilde{\tau}$) is location- and slope-dependent (discussed more in subsection 3.1.2).

2.2.3. Sand flux

As the wind blows over a sandy surface, it exerts streamwise shear stress (Walker & Nickling 2002) and imparts momentum to grains at the surface, initiating a sand flux (transported via saltation and reptation; Figure 2.2). This sand flux will increase until the wind-borne momentum is just enough to maintain the sand flux (Owen 1964).

Since Bagnold (1941), much work has been done to quantify this saturated sand flux (also called the sand drift potential). Bagnold derived and empirically verified that sand flux is proportional to u_*^3. Other studies have refined these equations through laboratory and theoretical studies (e.g., Lancaster 1995, Bullard 1997, Ni et al. 2004, Sorensen 2004, Durán & Herrmann 2006), but a roughly cubic relation with the shear stress velocity is consistently found and will be used in the remainder

of this study.

It is important to note, however, that the relationship between wind speed and sand flux is discontinuous (Lettau & Lettau 1978, Fryberger 1979) as grains are not moved unless the shear stress exerted on the grains by the wind is above some threshhold (τ_t, the *fluid threshold* in Bagnold 1941). For example, a system of sand grains with a diameter of 250μm requires a minimum friction velocity of ~ 0.28m/s (Sauermann et al. 2001) to move the grains (on Earth). Generally, terrestrial modeling studies assume that the wind speed is sufficiently above the threshold amount that this is not a concern. When modeling martian dune evolution, this restriction may become more important, as discussed in Parteli & Herrmann (2007) and this study (Chapter 7).

An additional complication is that the windspeed threshold for sustaining grain motion (the *impact threshold* in Bagnold 1941) is less than τ_t. This suggests that although the initial ability of the wind to transport sand may depend primarily on higher gust velocities, sustained motion may depend on a (much) lower average velocity. This difference is especially important on Mars, where the ratio between the two thresholds is ~ 0.1 (Kok 2010). It has been proposed that this hysteresis effect has important implications for Mars (Almeida et al. 2008); measurements of wind speed imply that the wind speed may rarely be above the fluid threshold (Greeley et al. 1980, Parteli & Herrmann 2007) which is inconsistent with observations of saltation (Sullivan et al. 2008). On the Earth, the two thresholds are much closer together (ratio ~ 0.8) so this effect can be neglected in modeling studies (Kok 2010).

2.2.4. The shadow zone

As the wind passes over a dune brink, the (previously compressed and accelerated) airflow expands and decelerates, generating a drop in surface shear stress. This decrease in shear stress can be extreme if the change is slope is sufficiently abrupt; as the airflow passes the dune's brink, it can separate from the topography and create a region of low pressure, generally containing a weak recirculation flow (Figure 2.5; Frank & Kocurek (1996*b*), Walker & Nickling (2002)). This recirculation flow is generally too weak to move much sand, so we approximate it as a zone of stagnant air (Figure 2.2). Grains transported over the brink into this *shadow zone* simply fall directly down onto the top few meters of the slipface of the dune, piling up until the angle of repose is exceeded and avalanching occurs (Lancaster 1995).

It was originally assumed that the extent of the shadow zone would correspond to the distance necessary for flow to return to far-field velocity values. However, wind tunnel (Walker & Nickling 2002) and numerical modeling (Parsons et al. 2004) experiments indicate that a horizontal distance of tens of the upwind dune's height is needed for full boundary layer recovery, which is much larger than the observed spacing between dunes (4-10 times the upwind dune's height (Lancaster 1995)). Instead, this distance correlates roughly to the flow reattachment distance (Frank & Kocurek

1996*b*, Walker & Nickling 2002, Parsons et al. 2004, Schatz & Herrmann 2006) and it is now thought that full flow recovery may never occur over closely-spaced dunes (Walker & Nickling 2003). Implications of flow differences over closely-spaced dunes versus an isolated dune will be examined in more detail in subsection 5.1.2.

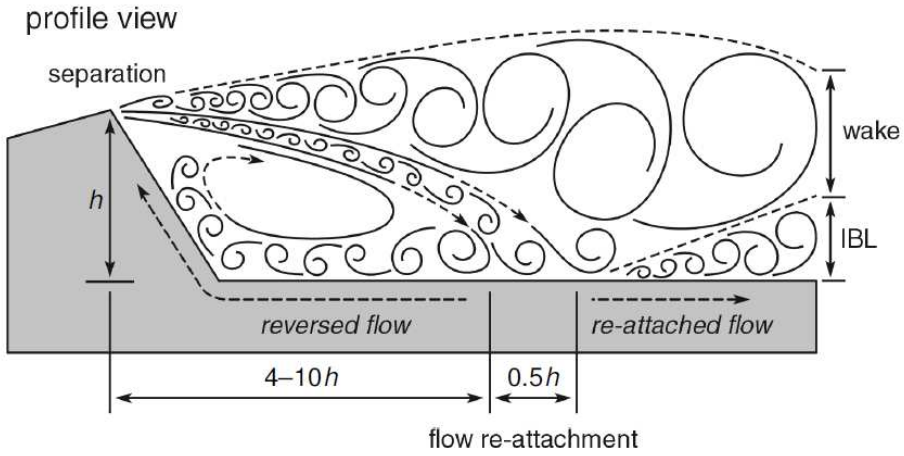

FIGURE 2.5. Schematic diagram showing flow separation as the wind flows over the dune brink, forming a recirculation zone, followed by the reattached flow. Image is from Walker & Nickling (2002).

Beyond the shadow zone, observations indicate that rapid erosion will occur as the wind is undersaturated and accelerating as it recovers (Fryberger et al. 1984, Baddock et al. 2007).

3. THE DUNE MODEL

The seminal work of Sauermann et al. (2001) is the basis for most current continuum models of the formation and evolution of sand dunes. This study constructed a two-dimensional model which considered the evolution of an wind-driven sand flux layer over a dune, and mass exchanges between this layer and the dune itself. Its main improvement over previous models (e.g., Stam 1996) was the inclusion of a spatial delay (the saturation length) over which the sand flux evolved toward the carrying capacity of the wind. This spatial delay had first been observed and measured by Bagnold (1941) and had been discussed in various modeling studies (e.g., Howard et al. 1978), but was not incorporated into previous models. Simulation and analysis have proven the value of including this spatial delay in the continuum dune evolution model, as it fixes the unphysical anchoring/lengthening of the foot of the dune seen in previous models and provides a characteristic length scale related to minimal dune size (Andreotti et al. 2002*b*, Claudin & Andreotti 2006). Later refinements considered linearized versions of the equations (Kroy et al. 2002, Andreotti et al. 2002*b*) as well as extension to 3-dimensions (Hersen 2004).

Such dune evolution models have been used to study the influences of wind and sand flux on details of dune morphology (Herrmann et al. 2005, Parteli et al. 2006) and the influence of vegetation and induration in stabilizing dunes (Herrmann et al. 2008). Additionally, many studies have examined the characteristic scaling of dune formation and evolution in different environments, such as underwater or on Mars (e.g. Claudin & Andreotti 2006, Parteli & Herrmann 2007).

In this chapter, we outline the continuum dune evolution model used in our studies. We also analyze model equations to determine appropriate model parameters and characteristic dune size scales.

3.1. Model Description

One drawback in the use of a continuum model is the large number of constitutive equations and environmental parameters that must be specified. In developing our own version of the two-dimensional continuum dune model, we have endeavored to identify the ingredients which have a significant quantitative effect on results. With respect to these ingredients (which are outlined below and illustrated in Figure 3.2), our model deviates little from assumptions used in other continuum dune models. As in those models, we evolve two layers of sand: the moving sand volume flux $q(x,t)$ and dune height $h(x,t)$.

3.1.1. Separation bubble

The profile of the near-surface airflow is a function of topography, and takes into account airflow separation in regions downwind of sharp changes in slope (the *shadow zone* described in subsection 2.2.4). Only weak recirculation occurs in these regions (Frank & Kocurek 1996*b*, Walker & Nickling 2002), so sand free-falls onto the lee slope, and then avalanches down, forming a slip face (Lancaster 1995). The upper-boundary of the shadow zone is the *separation bubble*, which extends downwind from the brink until the flow reattaches to the topography and aeolian sand transport resumes (Sauermann et al. 2001, Walker & Nickling 2003).

The precise details of flow separation can only be found through fluid dynamic calculations over the detailed dune topography, which is not well described and which evolves in time. Fortunately, it appears sufficient to phenomenologically approximate the separation bubble in calculations of wind-exerted shear stress upon the dune's stoss slope (Sauermann et al. 2003). We take this route in our continuum model and base our separation bubble shape on studies of airflow over simple dune-like geometries (Schatz & Herrmann 2006). We require only that:

- the separation bubble must match at the dune crest with the value and slope of the topography (C^1), and
- the separation bubble is scale-invariant, so will have fixed aspect ratio.

Past studies (e.g. Kroy et al. 2002) use a cubic polynomial as that is a simple functional that fits the requirements. In this model, we calculate the separation bubble (s_i describes the profile of the separation bubble extending downwind from the i$^{\text{th}}$ dune) as the upper-right portion of an ellipse with an semiminor to semimajor axis ratio of $\beta = 6.5$. This is based on the results of Schatz & Herrmann (2006), where CFD models were used to calculate actual streamlines over dune-type obstacles, and the streamline coming off the dune brink was fit to an equation.

We also conducted experiments with different types of functions for the separation bubble (parabolic, cubic, circular, elliptical functions). We found that the exact form of the function did not greatly change the calculated shear stress on the dune's stoss-slope as long it was sufficiently smooth (C^1) when paired with the original dune topography at the dune brink. One way in which the exact functional form of the separation bubble does matter is that it provides a "separation constraint" on the topography, as we define airflow separation as occuring when $h_i < s_i$ (equivalently, when the dune slope h_x extending downwind from the brink is steeper than the slope of s_i).

The overall separation bubble function s is defined then as a compilation of the separation bubble found over each individual dune:

$$s = \max(h, s_i).$$

Note that as s_i is only defined downwind of the i^{th} dune, the dune topography and the streamline always coincide on the upwind slope of the dune ($s_i = h_i$, excluding any area sheltered by an upwind dune's separation bubble); to the lee of a dune, $s_i \geq h_i$.

3.1.2. Shear stress

As described in subsection 2.2.2, the wind-exerted shear stress depends on the far-field strength of the wind (τ_0) and the topography-induced airflow compression ($\tilde{\tau}$), such that

$$\tau = \tau_0(1 + \tilde{\tau}). \tag{3.1}$$

Over a dune, $\tilde{\tau}$ is generally calculated through the use of boundary layer equations derived for airflow over a gently sloping, symmetrical hill (Jackson & Hunt 1975, Weng et al. 1991) involving a weighted-integral of the height gradient over the region and the local gradient itself:

$$\tilde{\tau} = A \int_{-\infty}^{\infty} \frac{s_x(x - \xi)}{\pi \xi} d\xi + B s_x(x). \tag{3.2}$$

Note the smooth airflow profile (s) is used to account for airflow separation; this has the benefit of avoiding numerical difficulties as the dune topography (h) is not differentiable at the brink.

The parameters A and B are generally treated as phenomenological parameters; physically, they relate to the logarithmic ratio between the dune and its surface roughness (discussed in Appendix A). Most studies assume that surface roughness depends primarily on sand grain diameter; in this case, A and B can be treated as constants, as the dunes change in size by a factor of 10^2 maximally, and the sand grains are $\geq 10^7$ times smaller than the smallest dune. A study by Pelletier (2009) considered that the effective surface roughness will depend on the dominant landform wavelength within a landscape: as ripples mature, they will dictate the surface roughness (not the grains), and so on. We have experimented with this approach, but did not find a large change in dune and dune field evolution.

Generally, we use $A = 4$, $B = 1$ in this study (Kroy et al. 2002). These expressions produce an acceptable approximation of the shear stress exerted along the stoss slope of an isolated dune (Figure 3.1; Sauermann et al. 2003). In the shadow zone to the lee of the dune, the near-surface wind is negligible so the shear stress is generally assumed to be zero and the sand flux simply decreases exponentially.

3.1.3. Saturated sand flux

The wind's shear stress is used to calculate the saturated sand volume flux, which is the equilibrium volume of sand the wind could move if the wind velocity and topography were homogenous. Equivalently, this is the sand flux that can be just maintained by the wind-borne momentum (Owen 1964).

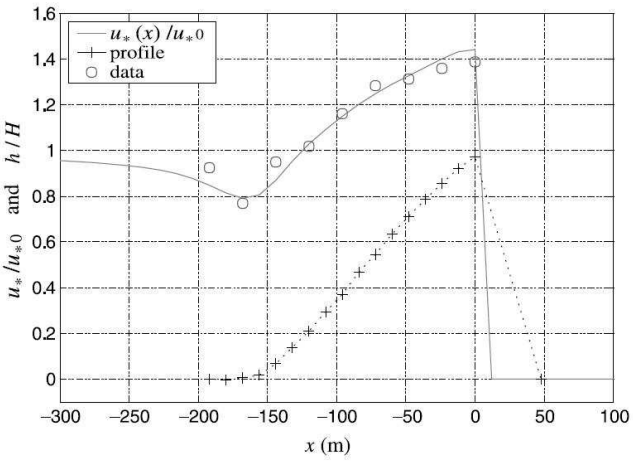

FIGURE 3.1. Circles show the measured shear velocity (u_*) over a dune, normalized by the far-field shear stress ($u_{*,0}$); these measurements show good agreement with the shear stress predicted by the Jackson-Hunt equation (solid line) over an isolated dune. To provide spatial context, the dune's profile is also shown (crosses, with height normalized by crest height: h/H). Image taken from Sauermann et al. (2003).

To calculate the saturated sand flux (q_s), we use Bagnold's relation ($q_s \sim \tau^{3/2}$; Bagnold 1941), which is a valid approximation as long as τ is sufficiently higher than the threshhold amount needed to initiate sand movement. We consider the simple linearized relationship:

$$q_s = (\tau_0(1+\tilde{\tau}))^{3/2} \tag{3.3}$$

$$\sim \tau_0^{3/2}(1+\frac{3}{2}\tilde{\tau}) \tag{3.4}$$

where the shear stress has been divided into a constant far-field parameter (τ_0, the shear stress exerted by a constant-velocity wind over a flat plane), and a topography-dependent perturbation term ($\tilde{\tau}(x,t)$, defined in subsection 3.1.2).

3.1.4. Sand flux

Due to the discrete nature of sand transport and the complex interactions of saltating and reptating grains, the actual sand flux evolves after a downwind spatial delay (called the *saturation length*) in comparison to the saturated flux:

$$q_x = \begin{cases} \frac{q_s - q}{l_s} & h > \epsilon \text{ and } h = s \\ 0 & h < \epsilon \text{ and } h = s \\ \frac{-q}{l_s} & h < s. \end{cases} \tag{3.5}$$

In these equations, l_s is the length over which the sand flux catches up to the saturated sand flux. Physically, it depends on the distance saltating/reptating sands bounce and on the ratio of saltating to reptating grains (Sauermann et al. 2001). The constraints on the different RHS cases correspond to several physical constraints:

- When airflow separation occurs ($h < s$; only on the leeside of the dune), then at the surface of the dune there is no effective wind flow and sand free-falls onto the lee slope.
- The limit ϵ is the height of sand above some "bedrock" layer ($h = 0$) below which we assume $h \sim 0$ and no erosion can occur. Thus, when this layer is exposed ($h < \epsilon$), q_x is constrained to be non-positive. Additionally, if the wind is exerting shear stress upon the surface ($h = s$), then it is assumed that moving grains will experience elastic collisions with the hard surface and continue moving (so $q_x = 0$).

It is important to note that the sandflux depends only on the dune and airflow profile (through the shear stress calculations), not on sandflux values found in previous timesteps. This assumption of "instantaneous" sandflux adjustment is based on the large difference in timescales over which the sand flow and the dune evolve; individual sand grains migrate tens of centimeters per second and dunes migrate tens of meters per year (a 10^6 difference).

3.1.5. Mass conservation and avalanching

Finally, we present the equation that couples our two layers of sand by relating the sand volume flux (q) to changes in dune height (h). This is a simple mass balance equation (also known as the Exner equation):

$$h_t = \text{-}q_x. \tag{3.6}$$

In our simulations, we use the modified equation:

$$h_t = \text{-}q_x + (D(h_x)h_x)_x, \tag{3.7}$$

where the added diffusion term accounts for avalanches. In most other studies (e.g. Sauermann et al. 2001), avalanching (within each time step) was accounted for through a separate BCRE-type (Bouchaud et al. 1994) diffusion model. In this work, the diffusion has been included directly in the model equation to simplify analysis and numerical simulation.

Avalanches occur only when the dune slope (h_x) exceeds the angle of repose (a maximum slope characteristic to piled cohesionless granular material, $\sim 34^\text{o}$). This is accounted for by letting the diffusion coeficient D vary as a function of h_x. When the angle of repose is reached or exceeded, D is chosen sufficiently large that the

timescale of avalanching dominates all other timescales. When h_x is smaller than the angle of repose, D is chosen small enough so as to operate over a very long timescale, reflecting small-scale smoothing processes such as turbulent air flow and the random orientations of reptating grains.

Both analysis and simulation testing were employed to select the values of $D(h_x)$. The Peclèt number of the system reflects the relative timescales of diffusion versus advection, and can be computed as:

$$Pe = LV/D.$$

We are interested in dune lee slope dynamics, so L is the length of the lee slope ($\sim H$, where H is the dune crest height) and V is the migration velocity of the dune. A simple geometric argument shows that $V \sim Q/H$, where Q is the sandflux over the dune crest (Bagnold 1941). Thus:

$$Pe \sim Q/D. \tag{3.8}$$

Diffusion (avalanching) should dominate when the dune slope exceeds the angle of repose, so we choose $D \sim Q$ (causing Pe to be small). D is chosen to be two orders of magnitude smaller than Q otherwise.

In Section 7.3, we will explore the effect and physical significance of this approximation in more depth.

3.1.6. Complete system

The complete and closed system of equations is as follows:

$$h_t = -q_x + (D(h_x)h_x)_x \tag{3.9}$$

$$q_x = \begin{cases} \frac{q_s - q}{l_s} & h > \epsilon \text{ and } h = s \\ 0 & h < \epsilon \text{ and } h = s \\ \frac{-q}{l_s} & h < s. \end{cases} \tag{3.10}$$

$$q_s = C_q \tau_0^{3/2} (1 + \frac{3}{2}\tilde{\tau}) \tag{3.11}$$

$$\tilde{\tau} = A \int_{-\infty}^{\infty} \frac{s_x(x-\xi)}{\pi\xi} d\xi + B s_x \tag{3.12}$$

where s is as defined in subsection 3.1.1. Typical parameters used in terrestrial and martian dune simulations are given in Table 3.1.

3.1.7. Non-dimensionalization

There are two natural length scales in these equations: the minimum sand depth at which saltating grains will not be influenced by the underlying bedrock (ϵ) and

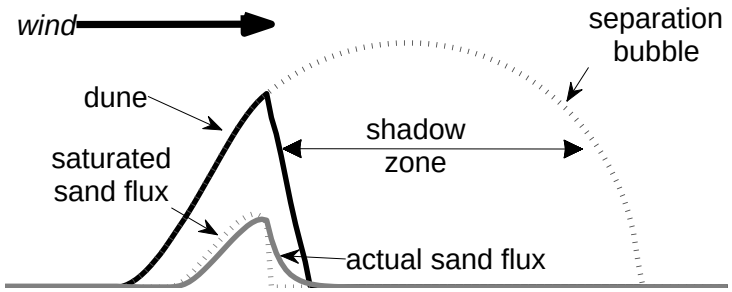

FIGURE 3.2. Schematic diagram showing the variables that are computed in a continuum dune model: dune topography → separation bubble/shadow zone → saturated sand flux (via shear stress calculation) → actual sand flux → dune topography. This diagram is the result of a simulation run, with the vertical scale of each parameter exaggerated for clearer superposition.

the saturation length (l_s). As $\epsilon \sim d \ll l_s$ (where d is a typical grain diameter), the minimal sand depth should be a small value even in the nondimensional model. Thus, l_s is taken as the characteristic lengthscale. The natural scale for the flux is the unperturbed/flat-plane saturation flux $= C_q \tau_0^{3/2}$.

This allows us to define a characteristic time of $l_s^2/(C_q \tau_0^{3/2})$, leaving just a few nondimensional constants:

- the parameters in our stress perturbation equation (A and B), which are unchanged.
- a new lower limit on h ($\epsilon/l_s \to \tilde{\epsilon}$),
- and a non-dimensional diffusion coefficient ($\frac{D(h_x)}{\tau_0^{3/2}} \to \tilde{D}(h_x)$) which is the inverse Peclét number (discussed in subsection 3.1.5).

The non-dimensionalized equations are (note abuse of notation: tilde's denoting non-dimensionalization have been dropped):

	Earth	Mars
saturation length (l_s) [m]	1	13
wind velocity threshold for saltation ($u_{*,th}$)	0.28	1.5
far-field saturation sand flux ($q_{s,\infty} = C_q \tau_0^{3/2}$) at $1.5u_{*,th}$ [m^2/s]	2e-3	4e-5
diffusion coefficient when avalanches occur ($D(h_x \geq 34^o)$) [m^2/s]	1e-2	1e-5
diffusion coefficient otherwise ($D(h_x < 34^o)$) [m^2/s]	1e-4	1e-7
lower limit on mobile sand (ϵ) [m]	1e-3	1e-3

TABLE 3.1. Typical parameters used in terrestrial and martian dune simulations, based on values found in Sauermann et al. (2001), Parteli & Herrmann (2007). The value for ϵ was approximated as 10 times the typical dune sand diameter, which appears comparable between Earth and Mars (Claudin & Andreotti 2006, Parteli & Herrmann 2007).

$$\tilde{\tau} = A \int_{-\infty}^{\infty} \frac{s_x(x-\xi)}{\pi \xi} d\xi + B s_x \tag{3.13}$$

$$q_s = 1 + \frac{3}{2}\tilde{\tau} \tag{3.14}$$

$$q_x = \begin{cases} q_s - q & h > \tilde{\epsilon} \text{ and } h = s \\ 0 & h < \tilde{\epsilon} \text{ and } h = s \\ -q & h < s. \end{cases} \tag{3.15}$$

$$h_t = -q_x + (D(h_x)h_x)_x \tag{3.16}$$

3.1.8. Simulation algorithm

The simulation evolves the non-dimensional dune profile h over a time step dt, via several steps:

1. Consider the dune profile $h(x, t_n)$;
2. Apply diffusion to the surface, causing "instantaneous" avalanches where the slope exceeds the angle of repose (this is done first to eliminate unrealistic steep slopes);
3. Calculate separation bubble $s(x)$;
4. Calculate shear stress perturbation $\tilde{\tau}(s)$;
5. Calculate saturated sand flux $q_s(\tilde{\tau})$;

6. Calculate actual sand flux via $q_x(q_s)$ equation;
   Note that it is this step which preserves nonnegativity of h, as $q_x \leq 0$ (only deposition can occur) as long as h is small (i.e., can't erode below the "bedrock" surface: $h < \epsilon$).

7. Calculate evolution in $dh(q_x)$;

8. Iterate for next time step: $h(x, t_{n+1}) = h(x, t_n) + dh$.

Further details of the numerical algorithm are given in Appendix A.

3.2. Model Analysis

Studies of isolated dune evolution are able to replicate reasonable dune profiles of many sizes and types, such as tranverse dunes (Figure 3.3) or three-dimensional barchans (e.g., Hersen 2004). Comparison between simulated dune forms and behaviors and observed dunes is the primary method used for validation of the model equations. A more quantitative exploration of observed relations is also done through numerical simulation and analysis.

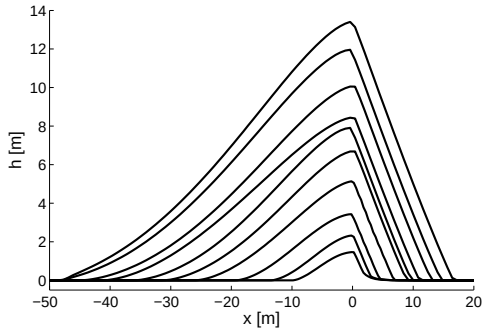

FIGURE 3.3. Sample steady-state two-dimensional terrestrial aeolian dune profiles calculated through numerical simulation. Different dune cross-sectional areas are shown, from a roughly minimum-sized transverse dune (dunes with height less than 1m consist of a convex windward slope with no slipface; these are known as *dome dunes*) to a dune 14m in height. Note that the vertical axis is exaggerated – the average windward slope for these profiles is $\sim 10^o$, which is comparable with measurements (Cook et al. 1993, Parteli, Schwämmle, Herrmann, Monteiro & Maia 2005).

3.2.1. Linear stability analysis

Linear stability analysis of similar model equations (without the diffusion avalanche term) about a perfectly flat plane with flux at the saturated flux value ($h(x, t) = H_0$

($> \epsilon$) and $q(x,t) = 1$) was originally done by Andreotti et al. (2002*b*). We simply restate the results here, as we assume the initial pertubation is sufficiently small that diffusion can be neglected (i.e., D remains small). For perturbations of the form:

$$h = H_0 + H\exp(\sigma t + ikx) \tag{3.17}$$
$$q = 1 + Q\exp(\sigma t + ikx) \tag{3.18}$$

we have a perturbation growth rate of:

$$\sigma = \frac{3k^2(-A|k| + B)}{2(1+k^2)} \tag{3.19}$$

Thus, the instability grows in time when

$$B > A|k| \Rightarrow |k| < B/A; \tag{3.20}$$

i.e., we expect a long wavelength instability. Taking just the linear portions of $d\sigma/dk = 0$ we see a maximal growth wavenumber:

$$k_{max} = \frac{2B}{3A} \tag{3.21}$$
$$2\pi/k = \lambda_{max} = \frac{3\pi A}{B} \tag{3.22}$$

Plugging in A = 4, B = 1, we have a wavelength of ~ 38, which is observed numerically to be the first wavelength of growth.

Redimensionalizing with $l_s \sim$ 1m for terrestrial dunes or $l_s \sim$ 13m for martian dunes (Claudin & Andreotti 2006), we approximately replicate the mean dune sizes observed on these two planets (Figure 3.4) of around 30m and 500m, respectively. This demonstrates that the model equations used do capture the initial dynamics of dune growth, which depends on the characteristic length scale l_s. Further dune growth is due to nonlinear effects, such as flow separation and dune interactions.

3.2.2. Reduced dimensional analysis

To further simplify the dune model, we neglect the detailed dune morphology and instead approximate the dune form with a piecewise linear shape (Figure 3.5). This allows us to describe the profile with just two variables: $m(t)$, the horizontal location of the dune brink, and $\sigma(t)$, the stoss slope:

$$h(\sigma(t), m(t)) = \begin{cases} \sigma(t)(x - m(t)) + H, & m(t) - H/\sigma(t) < x < m(t) \\ -\tan(34^o)(x - m) + H, & m(t) < x < m(t) + H/\tan(34^o) \\ 0, & \text{otherwise.} \end{cases} \tag{3.23}$$

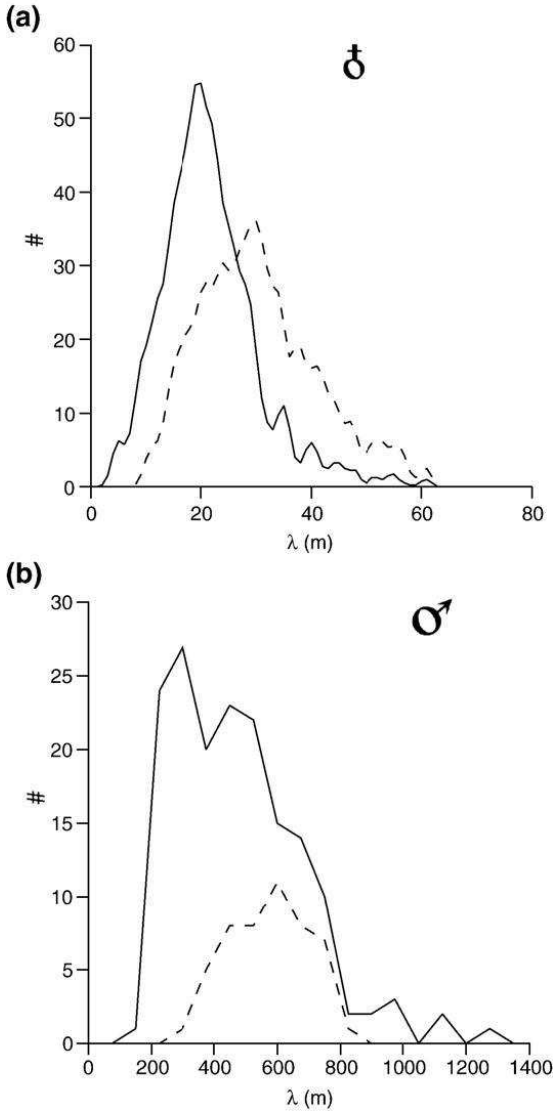

FIGURE 3.4. Histograms of the dune wavelengths measured on (a) Earth and (b) Mars. (a) The solid line shows barchan dune wavelengths throughout a Moroccon dune field, and the dashed line shows dune wavelengths on the windward side of a mega-barchan within that field. (b) The solid line shows dune wavelengths measured within in several intracrater fields, and the dashed line considers only Kaiser crater (19E, 47S) dunes. Averaged wavelength values are 20 m (solid line on panel a), 28 m (dash line on panel a), 510 m (solid line on panel b) and 606 m (dash line on panel b). Images taken from Claudin & Andreotti (2006).

The dune height H can be determined as a function of σ if the volume V (which is the area of the dune shape in one dimension) is specified and held constant:

$$H(\sigma) = \sqrt{\frac{2V}{1/\sigma + 1/\tan(34^{\circ})}}. \tag{3.24}$$

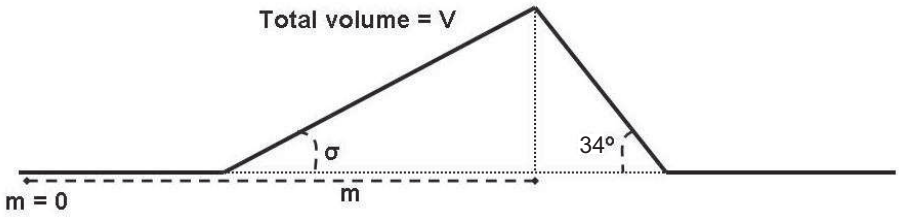

FIGURE 3.5. This is the simplest representation of a dune profile, where given an initial and constant dune area (V), only two variables (m and σ) are needed to define the dune shape and location.

We consider temporal evolution of m and σ by projecting the right hand side of Equation (3.6) ($dh/dt = (\partial h/\partial m)(dm/dt) + (\partial h/\partial \sigma)(d\sigma/dt) = \text{-}q_x$) onto the space spanned by $\partial h/\partial m$ and $\partial h/\partial \sigma$. To complete this projection, we use the inner product:

$$\langle f, g \rangle = \int_{m(t)-H/\sigma(t)}^{m(t)} f(x)g(x)dx \tag{3.25}$$

and the functions $v_1 = 1$ and $v_2 = x - m + L/2$, which span the same subspace as $\partial h/\partial m$ and $\partial h/\partial \sigma$ over the dune's stoss slope.

The second inner product results in:

$$\langle -q_x, v_2 \rangle = \frac{L^2}{12}\frac{d\sigma}{dt} \tag{3.26}$$

This equation gives the evolution of the windward side angle which is independent of m. With this analysis, we can see that for a given dune mass, the stoss slope (σ) will approach an equilibrium value, implying the existence of an equilibrium dune shape for a given dune size. However, this slope is higher than observed transverse dune stoss slopes, which have average values of $\sim 10^{\circ}$ (Momiji et al. 2000, Parteli, Schwämmle, Herrmann, Monteiro & Maia 2005) and peak values of $\sim 15^{\circ}$ (Cooke et al. 1993). Thus, detailed dune morphology and dynamics must play a role in setting observed dune shapes and sizes.

The first inner product yields:

$$\frac{dm}{dt} = -\frac{1}{H}\Big[\langle -q_x, v_1 \rangle - \frac{d\sigma}{dt}(L\frac{\partial H}{\partial \sigma} - L^2/2)\Big]. \tag{3.27}$$

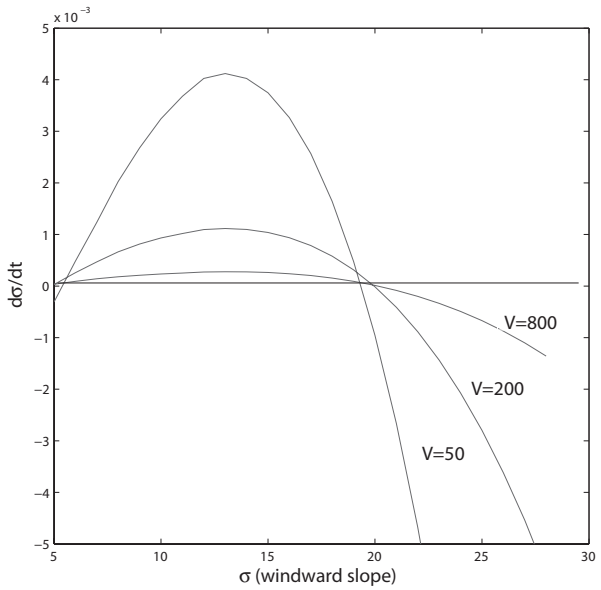

FIGURE 3.6. Dynamics of windward slope as a function of slope for several different size dunes (the values V refer to the dune's cross-sectional area). For each dune size, there is a single stable equillibrium value (for large dunes, this is about 18°).

If the dune has a steady shape ($d\sigma/dt = 0$), then the dune migration velocity will be:

$$\frac{dm}{dt} = -\frac{1}{H}\langle -q_x, v_1 \rangle = \frac{q(m - H/\sigma) - q(m)}{H}. \tag{3.28}$$

and we reproduce the observed inverse relationship between the dune height and its velocity (Bagnold 1941).

A reduced-dimension model was also developed for a two-dune system, and is described in Appendix B. This model was used to investigate binary dune collisions, but the large number of coupled variables needed to describe the system (12 versus 2 in the one-dune system) did not simplify the simulations or analysis, so this approach was abandoned.

4. INFLUENCE OF SAND FLUX

As the dune evolution model was constructed based on the averaged-dynamics of sand transport, we begin our analysis by considering the influence of sand flux on an individual dune's evolution. In this chapter, we then extend those results to evaluate dune evolution within a field, where dunes interact through sand flux (i.e., a dune's influx sand amount is set by the upwind dune's outflux).

4.1. Physical Description

As discussed in Section 2.1, sediment supply and sand flux dynamics exert crucial influences on dune evolution. The sand flux over a dune is one of the main measurements made within field studies of dunes. However, estimates of the total saltating sand flux cannot be easily related to dune migration, as:

- dunes are not perfect collectors. A large fraction of the incoming sand flux can be lost off the horns of barchan dunes (Hersen 2004), and sand can also be lost from transverse dunes (Momiji & Warren 2000);
- dune migration and growth is related to the net (not gross) sand flux over a dune;
- the sediment flux available to a field generally originates at a point or line source(s), and thus is not uniform within a field. Instead, the sediment flux available to a dune within the field depends primarily on the amount of sand escaping from the nearest upwind dune(s) and topography.

Thus, to consider dune evolution within a field, it is necessary to consider the exchange of sand between dunes.

4.2. Model Results

As the goal of these simulations is to evaluate the effect of sand flux (not total sand available), simulations were run with a semi-infinite boundary condition with fixed influx.

4.2.1. The need for a non-zero influx

Laboratory (Katsuki, Kikuchi & Endo 2005) and field observations (Hersen 2004) show that dunes will lose sand downwind through crest defects and other three-dimensional features, such as barchan dune horns, as they evolve and migrate. This

loss is enhanced through stochastic variations in wind direction and strength. Thus, an incoming sand flux is necessary for a dune's continued existence.

In our simulations, these three-dimensional effects are neglected; we essentially consider only defect-free transverse dunes, so care must be taken in comparing our two-dimensional simulation results to three-dimensional dunes. When the dune form is constrained to two dimensions, the slipface can act as a perfect collector, losing sand only when the dune slipface length is small (so that some saltating grains pass completely over the lee slope). Measurements of sand flux over the brink of a terrestrial desert transverse dune showed that 55%–95% of the sand flux is deposited within 1m of the crest, and 84–99% within 2m (Nickling et al. 2004).

From equation 3.5, we can see that sand flux decays exponentially once past the dune brink from equation 3.5 (and $q_s = 0$ in the separation bubble):

$$q_x = -\frac{1}{l_s} q \tag{4.1}$$

$$\Rightarrow q(x) \sim e^{\frac{-1}{l_s} x}. \tag{4.2}$$

As the lengthscale for sand flux decay is l_s, we have a minimum slipface height that will scale with $l_s \tan(34^\circ)$ (as the slipface is at the angle of repose). For Earth, the minimum dune height at which a slipface develops and is stable is 1m, which is about twice the scale height. As a dune's height increases beyond this amount ($H \gg l_s \tan(34^\circ)$), it should very efficiently collect sand.

Observations and modeling studies have found that the sand-trapping efficiency of the slipface increases as the dune grows (Momiji & Warren 2000) even within three-dimensional dunes. This creates an unstable equilibrium dune size (at which the sand influx equals the sand outflux). Smaller dunes will experience an net loss of sand and shrink in size, while larger dunes will experience a net gain and grow.

4.2.2. Sand flux over a dune

In previous studies of dune evolution, there has been scant attention paid to the influx sand amount beyond a general assumption that it is small with respect to the far-field saturated sand flux ($q_{\text{in}} = C q_{s,\infty}$, $C \sim 0.2$). Observations of the interdune sand flux generally support this assumption (Fryberger et al. 1984); it is thought that the interdune sand flux remains limited to a small fraction of the saturated sand flux due to the fluctuations in wind speed enhancing deposition onto small-scale topography when a larger amount of sand is mobilized. Additionally, any sand available for saltation within interdune regions is rapidly eroded as the winds downwind of dunes and the separation bubble accelerate as they recover, and are typically undersaturated in sand flux (Fryberger et al. 1984, Baddock et al. 2007).

Despite this apparent natural limitation in keeping the influx sand amount (equivalently, the multiplicative factor $C \in [0, 1]$) small, we investigate the influence this free parameter exerts on dune evolution model.

Simulations of a dune moving over flat topography showed two types of behaviors: for low C values the dune migrated, and for large values C the dune did not migrate but instead grew in height and length with an anchored foot. (For very large values of C, the dune also grew backwards due to the slight decrease in shear stress at the toe of the dune which caused deposition.) These different behaviors were caused by differences in the amount of sand eroded from the foot and stoss slope of the dune, to be deposited on the lee side.

Simple physical scaling arguments yield the threshold between different values. The total amount of additional sand that the wind can carry when it encounters the dune is $(1 - C)Q$, while the amount of sand that must be moved for the dune to migrate is the mass of the dune (M). Thus, the threshold between dune migration vs. dune growth depends on $(1 - C)Q/M$ (which has units of inverse time): when $(1 - C)Q/M$ is smaller than a threshold amount the dune will remain in place and grow, and when $(1 - C)Q/M$ is larger, the dune will migrate (Figure 4.1).

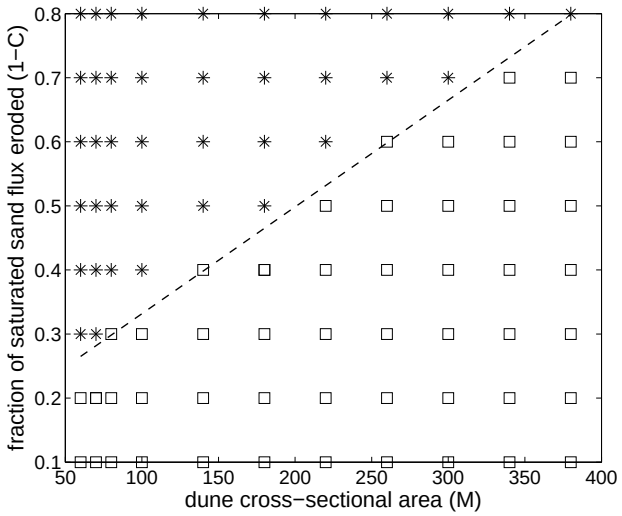

FIGURE 4.1. Plot showing that different dune dynamics: migration (*) or stationary growth (□), occur depending on the sand influx amount relative to the dune size. The boundary between the two dynamics is found when $(1 - C)/M \sim 0.002$; with the far-field influx (let $Q \sim q_{s,\infty}$): $(1 - C)Q/M \sim 5e$-6.

Thus, we again see unstable dynamics – for a given C and Q, large dunes will grow while smaller dunes migrate.

4.3. Physical Implications

Our results provide a negative conclusion with regards to controls on maximum transverse dune size: sand flux effects alone cannot regulate dune size within a field. For a given sand flux, simulated single dunes instead grow without bound (limited only by the total amount of sand available for accumulation). Previous continuum (Schwämmle & Herrmann 2004) and discrete (Momiji 2001) dune model studies found that the average transverse dune height within a field scales with the square root of time.

Combining this result with a line source of sediment for the field, and the increase in sand-trapping efficiency as a dunes grows means that dunes within a field should exhibit coalescent behavior: larger dunes will collect all upwind sand, while smaller dunes will become sand-starved and shrink in size, causing them to release more sand to the larger dunes (through increased downwind sand flux and collisions).

This analysis and our results are comparable to a study of barchan dune evolution by Hersen et al. (2004) (Fig. 4.2). That study found that solitary barchans and barchan fields are unstable in the case of a constant wind, with instabilities developing within a field of 100m wide dunes after a century, over a migration distance of a few kms. As observed dune fields hundreds of kilometers long do contain dunes of uniform size, Hersen et al. (2004) concluded that there must exist another dynamical mechanism that stabilizes the dunes sizes.

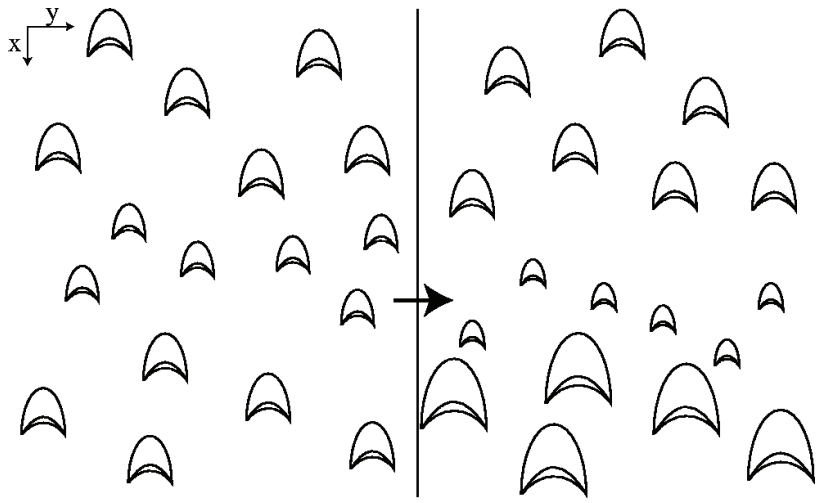

FIGURE 4.2. Sketch illustrating dune size instability within a field due to the exchange of sand between the dunes: small barchan dunes experience a net loss of sand, which causes their downwind neighbors to grow. This process continues as the small dunes shrink and the large dunes grow, causing coalescence as the sand is concentrated in a smaller number of larger dunes. Image is from Hersen et al. (2004).

We concur with this conclusion, and seek to identify a process(es) that limits dune size within a field, or that manages to balance the flux instabilities (at least within larger dunes). In the following chapters, we investigate the influence that dune interactions and bedrock topography can play in dune and dune field evolution.

5. INFLUENCE OF DUNE INTERACTIONS

Studies which consider the evolution and behavior of a single dune cannot be directly extended to evolution of dunes within a field, as isolated dunes do not behave and evolve the same way as dunes within a field. For example, as discussed in Chapter 4, individual dunes are unstable with respect to changes in the sand flux. This implies that dunes in a field, evolving only through sand flux, should eventually coalesce into a small number of large dunes (Hersen et al. 2004); as this does not occur, other processes must aid in limiting the sizes of dunes within a field.

In this chapter, we investigate the effect of neighboring dunes on shear stress and saltation. We also consider the dynamics of binary dune collisions, and evaluate evolution within a field through binary dune collisions. We find that collision dynamics can yield a field of similarly-sized dunes if the influx dunes' sizes are chosen from a sufficiently constrained population.

5.1. Physical Description

Wind tunnel (Walker & Nickling 2003) and field studies (Lancaster 1985, Baddock et al. 2007) of isolated or closely spaced dunes have shown that the presence of non-flat topography (such as terrain or neighboring dunes) will alter the wind-exerted surface shear stress, which in turn changes sand flux and dune evolution. For example, the distance before flow reattachment occurs is foreshortened by the presence of a downwind dune, causing the flow velocity at the foot of this dune to be lower (Walker & Nickling 2003). Wind speed up over the stoss slope is then found to increase faster over paired dunes than over isolated dunes (Lancaster 1985) – potentially steadying sand flux rates in the upper-portions of the stoss slope and increasing crestal erosion (Walker & Nickling 2003).

5.1.1. Effects not included in this study

These changes in flow dynamics are caused by greater turbulence as the reattaching flow encounters the downwind dune's stoss slope and is compressed (Sweet & Kocurek 1990, Baddock et al. 2007). This added turbulence is not accounted for in the airflow model used (subsections 3.1.1-3.1.2), so is not presently included in the dune evolution model used in this study. Empirical studies are needed to provide constraints on how the added turbulence will change sand transport and dune interactions; work by Palmer (2010) and Ewing & Kocurek (2010) are the only available studies that have begun to quantitatively examine this problem.

The interdune distance also is controlled by the reattachment and recovery of airflow in the lee of the upwind dune (Walker & Nickling 2002, Walker & Nickling 2003,

Schatz & Herrmann 2006, Baddock et al. 2007) (as described in subsection 2.2.4). This spacing may be influenced by three-dimensional or time-varying factors, such as complex secondary flow patterns (Walker & Nickling 2003), the incidence angle between the wind and dune crest, or changes in atmospheric stability (Sweet & Kocurek 1990); as the model used is two-dimensional and assumes steady airflow, these factors are not considered. Thus, this study does not focus on the specific controls and processes that control dune spacing, only dune sizes. Our method of modeling saltation over sand-free interdunal areas (described in subsection 3.1.4) causes spacing between simulated dunes to be proportional to the flow reattachment distance. This distance we assume to be proportional to the upwind dune height (subsection 3.1.1), causing our modeled interdune spacing to be related to dune sizes; this result matches to first-order observations of barchan and transverse dunes (Lancaster 1988).

5.1.2. First-order effect of topography on shear stress

We first investigate the distance over which non-flat topography will interact with a dune by considering the asymptotic behavior of the shear stress perturbation exerted at a point x by a nearby dune:

$$\Delta\tilde{\tau}(x) = \int_{\text{dune foot}}^{\text{dune slipface}} \frac{h_x(x-\xi)}{\pi\xi} d\xi \tag{5.1}$$

If the dune is downwind of x, then the ξ denoting where the dune is located ($h_x(x-\xi) \neq 0$) will be negative. The side of the second dune closer (and thus of more influence) is the stoss (positively sloped) side, so the overall effect of the shear stress perturbation is negative. Similarly, if the second dune is upwind, the relevant ξ will be positive and the more influential side of the second dune is the negatively sloped side, so the overall effect on the shear stress perturbation is negative. This makes physical sense, as additional topography would shift the wind-streamlines upward, thus decreasing the shear stress exerted on a dune surface.

To estimate the effect more quantitatively, assume a distance of d between the point of calculation and the dune foot. The dune is of length l, so $x_{\text{dune foot}} = x + d$, $x_{\text{dune slipface}} = x + d + l$ (Figure 5.1). Translating the horizontal coordinate system to: $\eta = -\xi - d$ and assuming $l \ll d$ yields:

$$\Delta\tilde{\tau} = \int_0^l \frac{h_x(x+d+\eta)}{\pi(d+\eta)} d\eta = \int_0^l \frac{1}{\pi d} \frac{h_x(x+d+\eta)}{1+\eta/d} d\eta \tag{5.2}$$

$$\approx \frac{1}{\pi d} \int_0^l h_x(x+d+\eta)(1-\eta/d) d\eta, \tag{5.3}$$

neglecting all higher order terms. (The last expression derived is the first-order taylor expansion of $\frac{1}{1+x}$ where $x \ll 1$, as $\eta/d \ll 1$ within the interval of integration). As the

FIGURE 5.1. Schematic diagram illustrating variables used in first-order topography-induced shear stress estimation.

dune is migrating over a flat plane, $\int_0^l h_x(x+d+\eta)d\eta = 0$. We integrate-by-parts the remaining integral (with boundary conditions $h = 0$):

$$\Delta\tilde{\tau} \sim \frac{-1}{\pi d^2}\int_0^l h(x+d+\eta)d\eta \tag{5.4}$$

$$\sim -\frac{A}{\pi d^2} \tag{5.5}$$

$$\sim -\left(\frac{d}{H}\right)^{-2} \tag{5.6}$$

where A is the total dune cross-sectional area ($A = \int_0^l h(x+d+\eta)d\eta$) and H is the dune height (assuming $A \sim H^2$; Figure 5.2).

This topography-induced decrease in shear stress results in lower saltation rates. As sand transport occurs at a slower rate, dune evolution, migration, and interactions will also occur at slower rates. Although this does not put a limit on dune size, this effect will play a (small) role in slowing dune growth as dunes within the field increase in size. Additionally, this will provide more time for other stabilizing processes to influence dune and dune field evolution.

5.2. Study of Dune Collisions

We investigate the dynamics of binary dune collisions by initializing our continuum dune model with two dunes of specified size, the smaller located upwind of the larger. The initial dune profiles were steady-state profiles calculated during simulations of isolated dune formation (found with periodic boundary conditions). The initial dune spacing was chosen by testing for the minimal distance at which no changes in size occurred immediately in the downwind dune because of the presence of the upwind dune (because of changes in its shear stress and, thus, sand flux calculation). To

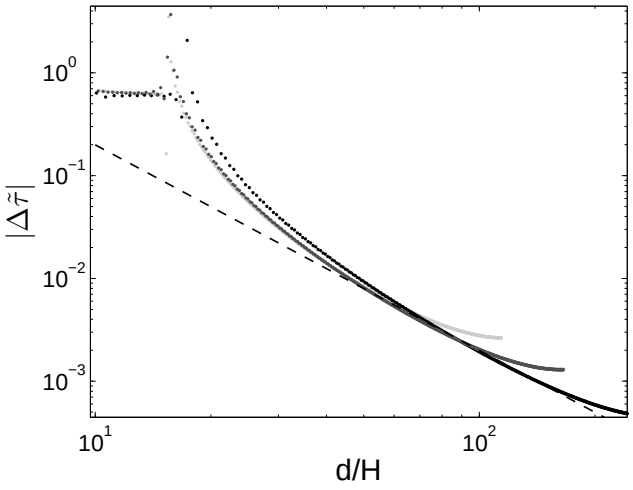

FIGURE 5.2. Log-log plot of the magnitude of the calculated $\Delta\tilde{\tau}$ as a function of distance from an upwind dune's foot, normalized by the dune's height ($H \sim \frac{1}{10}l$). The different curves were computed for dunes of different sizes, with the expected -2-power (trendline) appearing when $d > 30H$ ($\sim 3l$): $\Delta\tilde{\tau} \sim (d/H)^{-2}$. The $\Delta\tilde{\tau}$ curves curl up on the right as d becomes comparable to the computational domain size.

eliminate a dependence on the sand influx rate (which influences dune migration and growth, as discussed in subsection 4.2.2), periodic boundary conditions were used.

In these simulations, the upwind (and smaller, thus faster) dune catches up to the downwind dune. As the shadow zone of the upwind dune impinges upon the foot of the downwind dune, sand in the foot of the downwind dune is not transported by the wind and so is left behind and is eventually absorbed by the upwind dune. As the downwind dune loses sand, its profile gradually becomes shorter, which causes its velocity to increase. Similarly, the upwind dune gains sand, becomes taller, and decreases its velocity. Eventually, the upwind dune begins to climb the downwind dune and the two dunes would lose their distinct shapes and form an amorphous two-humped dune-complex. Sand continues to be exchanged and the humps change in height (the upwind hump grows and the downwind hump shrinks) while moving toward, then (once the downwind hump is the smaller of the two) away from each other (Figure 5.3).

Simulations were run with combinations of dunes with cross-sectional areas of $10-400m^2$ (corresponding to initial heights of $1-15m$), and dune pairs were categorized by the resultant type of interaction (Figure 5.4).

We noted two qualitatively distinct outcomes: (1) *coalescence* resulted when the downwind hump subsided into the dune complex, resulting in one unified dune, and

(2) *ejection* occurred when the downwind hump managed to separate completely, resulting in an exchange of material between the colliding dunes. In a small number of cases, the downwind hump managed to separate but was too small to remain stable and so would eventually *disappear*. We initially examined this case separately; as it occurred in only a small number of cases, we reclassified it as an extreme case of *ejection*.

Plotting the different types of dune interactions as a function of the sizes of the colliding dunes (downwind cross-sectional area: A_{before} vs. upwind cross-sectional area: $a_{\text{before}} < A_{\text{before}}$, Figure 5.4), it can be seen that the boundary between coalescence and ejection cases (i.e., the intermediary disappear cases) roughly follows a straight line passing through the origin. Along that line the size ratio between the two dunes before interaction is constant: $r = (a/A)_{\text{before}} \approx 1/3$. From this, we can see that if we consider a pair of dunes such that the line from that point (A, a) to the origin is less steep than that boundary (equivalently, the size ratio of the two dunes is between 0 and 1/3), coalescence occurs. Conversely, when the line between a point and the origin is steeper than the boundary (or the size ratio is between 1/3 and 1), the collision results in two dunes or ejection. Thus, it is appears that the size ratio (r) between the dunes is what determines a collision result, not the individual sizes of the dunes.

5.2.1. Defining the interaction function

To understand in more detail what will result when two dunes collide, we also compute the size ratio of the dunes after collision ($f(r) = (a_{\text{downwind}}/A_{\text{upwind}})_{\text{after}}$; where $a_{\text{downwind, after}} = 0$ if the dunes coalesce), and plotted this against the size ratio before dune collision (r). Resultant dunes which disappear are treated as very small ejection dunes because the sizes are measured as soon as the dune-complex separates into two dunes. As can be seen in Figure 5.5, the data collapses onto a single curve, indicating that dune size ratio resulting from a collision is uniquely determined by the size ratio before collision. We interpolate between the calculated points to generate the *interaction function*, which we will use in the dune field model to relate the before-collision size ratio (r) to the after-collision ratio ($f(r)$). We note that the interaction function has the following characteristics:

- The function $f(r)$ monotonically increases.
- When the initial size ratio of the colliding dunes is smaller than a threshold amount (here $r \leq 1/3$), $f(r) = 0$ indicating coalescence.
- In the limit where very similarly sized dunes collide, $f(r)$ appears to $\to 1$.

Similar results have been found elsewhere in the literature. For example, studies of discrete numerical simulations of interacting three-dimensional barchan dunes

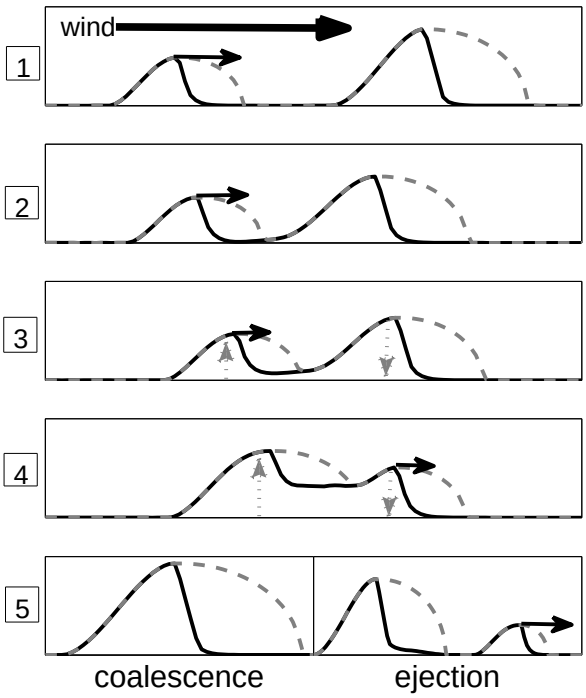

FIGURE 5.3. Schematic diagram illustrating a dune collision. The topography/dune profiles are outlined in black, and the separation bubble is outlined in gray. The horizontal arrows show relative dune velocity and the vertical arrows show changes in dune height. From top to bottom: 1. The upwind (smaller) dune approaches the downwind dune. 2. Eventually its separation bubble impinges upon the foot of the downwind dune, arresting that sand. 3. As the upwind dune continues to move toward the downwind dune, it gains sand that the downwind dune leaves behind. 4. As the upwind dune grows and the downwind dune shrinks, their relative crest height reverses, allowing the downwind dune to migrate faster than the upwind dune. 5. If the downwind dune loses all of its sand before it can migrate away, then we have *coalescence*. Otherwise, we have an *ejection* case.

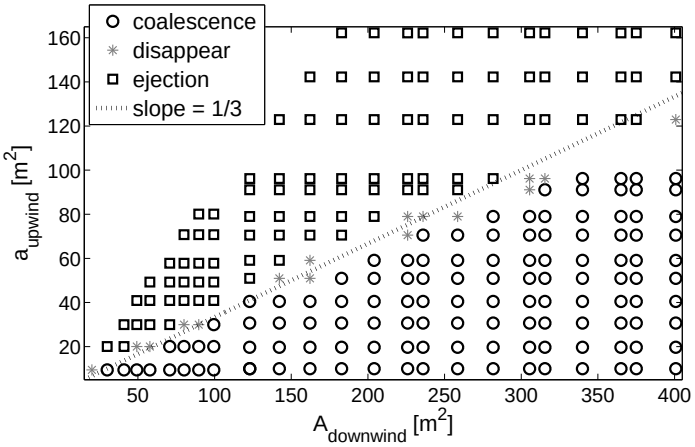

FIGURE 5.4. Plot of the different types of dune interactions as a function of the sizes of the dunes before collision: the area of the downwind dune (A) vs. the area of the upwind/smaller dune (a). Note that the boundary between *coalescence* and *ejection* roughly follows a straight line through the origin with slope of roughly 1/3. This implies that if the dune size ratio before collision: $(a/A)_{\text{before}}$ is smaller than 1/3, then coalescence occurs. Conversely, if $(a/A)_{\text{before}} > 1/3$, then two dunes result.

(Katsuki, Nishimori, Endo & Taniguchi 2005) and laboratory experiments of subaqueous barchan dune collisions (Endo, Taniguchi & Katsuki 2004) yield results which support our hypothesized interaction function characteristics. Additionally, a study by Durán et al. (2005) using continuum numerical simulations of three-dimensional barchan dune interactions found an interaction function (Figure 5.6) which also consists of a continuous, monotonic relation between size ratios before and after collision, with $f(r) \to 0$ as $r \to 0$ and $f(r) \to 1$ as $r \to 1$.

5.2.2. Dependencies of the interaction function

The balance between the timescale over which the upwind dune merges with the downwind dune and the rate at which the downwind dune shrinks (and migrates faster) is what determines the end result of a collision.

For example, the timescale over which the dunes merge is very short if dunes initially have very different sizes, as the relative velocity between the dunes is large. The dunes will merge together before the downwind dune can shrink sufficiently to escape, which is why $f(r) \to 0$ as $r \to 0$. Conversely, the rate at which the downwind dune shrinks is more important if dunes are initially very similar in size, because the relative velocity will be low. As they will move towards each other over a long time period, the downwind dune will be able to slowly escape after becoming slightly smaller than the upwind dune. The two dunes will end up close to each other in size,

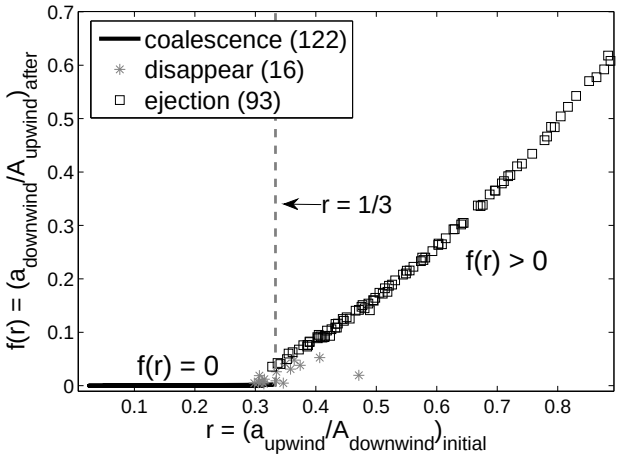

FIGURE 5.5. Plot of the area ratio of colliding dunes, before collision vs. after. Note the distinct zones of interaction results: coalescence occurs when the dune size ratio before interaction is below some threshold (1/3); when the ratio is above that threshold, then the output size ratio generally falls along a specific curve, independent of the absolute sizes of the dunes (the outlier corresponds to the smallest dune pair sampled). In the legend, the numbers given are the total number of simulations which yielded that particular type of interaction.

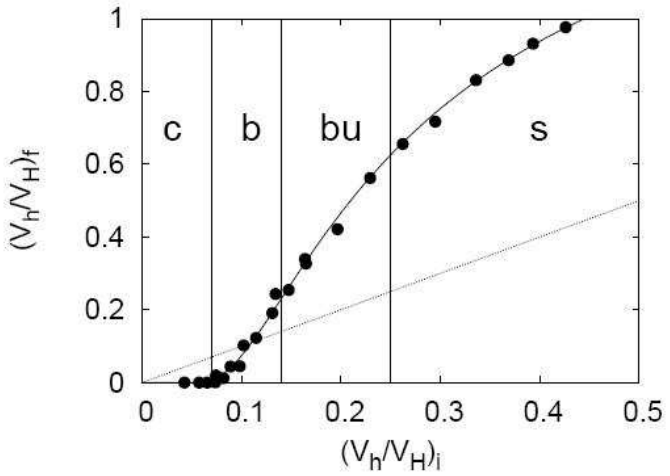

FIGURE 5.6. This plot was derived for three-dimensional barchan dune collisions by Durán et al. (2005) and shows volume ratios of colliding barchan dunes before versus after collision (the dots, along with a best fit curve). It exhibits the same characteristics as the interaction function shown in Figure 5.5: a threshold between coalescence (c) versus all ejection-type interactions (b/bu/s: breeding, budding, solitary waves), a single monotonic curve along which all points fall and which passes through (0,0) and probably (1,1). The straight line shown has a slope of one.

so $f(r) \to 1$ as $r \to 1$.

However, the range of the interaction function does not include the end-point (1) as it is not possible for an interaction to yield two exactly similar dunes – these two dunes will move at exactly the same velocity, whereas an ejected dune must be able to move away from the upwind dune. By similar reasoning, the domain of the function also does not include 1 as it is not possible for dunes migrating at the same velocity of collide. The range (but not the domain) does include 0 as long as coalescence can occur.

A continuum between these two effects is expected, as the timescale over which dunes interact will increase as the disparity between the sizes of the two dunes increases. This yields a continuous, monotonic function.

In summary, we expect an interaction function to have the following characteristics:

- $f : (0, 1) \to [0, 1)$,
- continuous and monotonically increasing,
- $f(r) \to 0$ as $r \to 0$,
- $f(r) \to 1$ as $r \to 1$.

The exact form of the function will depend on factors which set the timescale over which the dunes interact and the rate of the sand exchange between the dunes. In the continuum dune model, for example, one way to change the rate at which sand is exchanged is by increasing the aspect ratio of the separation bubble (β). This lengthens the shadow zone of the upwind dune, causing the foot of the downwind dune to be caught in that shadow zone and arrested sooner. The downwind dune, thus, loses more sand before the upwind dune begins to gain sand. As the growth of the upwind dune is delayed relative to the shrinkage of the downwind dune, the downwind dune will need to shrink more to become the smaller of the two. When the downwind dune is finally ejected, it will be smaller (and the upwind dune will be larger), causing the interaction function to be lower (i.e., $f(r)$ will decrease $\forall r$ where $f(r) > 0$). Conversely, if the length of the separation bubble is decreased, then the interaction function will be higher. Test simulations have shown this to be the case, although the effect was small (Figure 5.7).

5.2.3. Implications of the crossover value

Our interpolated interaction function for transverse dunes (Figure 5.5) is included in this study to explain the general form of an interaction function. The specific function that was found through our two-dimensional dune simulations, however, will not be used in the remainder of this study because that functional form (where $\forall r$, $f(r) < r$) yields coalescence-dominated dynamics.

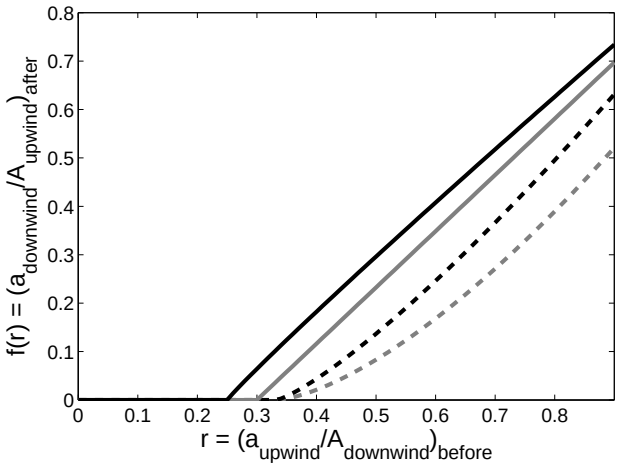

FIGURE 5.7. This plot shows the best-fit interaction functions for transverse dunes, after using different separation bubble aspect ratios (β) in the continuum dune model: from top, $\beta = 3$, 6.5 (shown in Figure 5.5), 8, 10. As hypothesized, $f(r)$ decreases as the separation bubble aspect ratio is increased (lengthening the length of the shadow zone) due to its influence on how quickly the downwind dune is able to lose sand.

When $\forall r \in (0,1), f(r) < r$, then in every collision the larger dune grows and the smaller dune shrinks. As the smaller dune in every collision shrinks and eventually coalesces with the larger dunes (for small enough r, $f(r) = 0$), the dune field perpetually evolves into a system containing a smaller number of larger dunes. This type of dune field dynamics will never yield a stable pattern of similarly sized dunes, and will in fact never be stable (as shown in Proposition 1).

Proposition 1 (Guaranteed Coalescence)**.** *Let us consider a dune field with a continuous influx of dunes chosen from a fixed size population with some variance (i.e., not a delta-function). If this field's interaction function f satisfies the following:*

1. $\forall r \in (0,1),\ f(r) < r$, *and*
2. $\exists r_c$ *such that* $\forall r < r_c, f(r) = 0$,

then the dune field will perpetually exhibit coalescent dynamics.

Proof. If the influx dune size population is fixed, then the average size of a dune within the field ($\bar{M} = \int_0^\infty Mp(M)dM$, where $p(M)$ is the probability density of dune sizes within the field) will be the same as the average dune size within the influx population unless coalescence occurs and the number of dunes decreases. Thus, it is sufficient to show that interactions resulting in coalescence will continuously occur within the field.

This can be seen by considering the variance of $p(M)$ (given by the second moment: $\int_0^\infty M^2 p(M) dM$). As $\forall r,\ f(r) < r$, then mass is distributed from the smaller to the larger dune ($m \to m - \epsilon$ and $M \to M + \epsilon$, $\epsilon > 0$), and:

$$\begin{aligned}(m-\epsilon)^2 + (M+\epsilon)^2 &= m^2 + M^2 + 2(M-m)\epsilon + 2\epsilon^2 \\ &> m^2 + M^2. \end{aligned} \tag{5.7}$$

Thus, we see that the variance will increase with every binary dune collision. As the mean is unchanging (unless coalescence is occurring), then this implies that, after a sufficient number of interactions, small dunes will be created that will experience collisions with r sufficiently small ($r < r_c$) that $f(r) = 0$. This will only be negated if the dune field becomes size-sorted (i.e., all of the small dunes are at the front of the field), but size-sorting cannot occur as long as the (fixed) influx of dunes is continued. □

Conversely, when $\forall r, f(r) > r$, then in all collisions the dunes become more similar in size. Eventually, after many collisions, the dune field will always evolve into a system of many similarly-sized dunes (with any remaining collisions occurring around $r \sim 1$), as shown with Proposition 2.

Proposition 2 (Guaranteed Patterning)**.** *Let us consider a dune field with a continuous influx of dunes chosen from a fixed size population. If this field's interaction function f is such that $\forall r \in (0,1),\ f(r) > r$. then the dune field will evolve into a system of similarly-sized dunes.*

Proof. We again consider the the variance of the probability density of dune sizes within the field ($\int_0^\infty M^2 p(M) dM$). As $\forall r,\ f(r) > r$, then mass is distributed from the larger to the smaller dune ($m \to m + \epsilon$ and $M \to M - \epsilon$, $\epsilon > 0$), and:

$$(m+\epsilon)^2 + (M-\epsilon)^2 = m^2 + M^2 - 2(M-m)\epsilon + 2\epsilon^2.$$

This is smaller than $m^2 + M^2$ only if $\epsilon < (M - m)$, but this is within the defined limit of mass exchange ($\epsilon < (M-m)/2$)as the small dune cannot become larger than the large dune (or it would *be* the large dune). Thus, we see that the variance will decrease with every binary dune collision, implying that the system moves towards a population of similarly-sized dunes. □

In most systems, the variance will be kept non-zero through size-sorting (as small dunes escape at the front of the field) and as the influx is continued (if coalescence has occurred, $\bar{M}$ within the field will be larger than the mean size within the influx population).

As one more extreme example: if $\forall r, f(r) = r$, then dunes will behave similar to solitons in that all interactions will preserve the sizes of the dunes involved, as if the dunes simply pass through each other.

Most natural dune field interaction functions will not correspond with one of these examples (in particular, see Livingstone et al. (2005) for a discussion about the unphysical nature of the soliton example). Instead, a natural dune field interaction function will probably be a combination of these extreme examples, with some regions where $f(r) < r$, some regions where $f(r) > r$, and transition points where $f(r) = r$. In these cases, the dynamics of the dune field can be determined based on the interaction function *crossover value*: the value r_* such that for all higher $r < 1$, $f(r) > r$. We define the crossover value as the lower bound on the region *connecting to (1,1)* where $f(r) > r$. An interaction function may have several regions where $f(r) \geq r$, but only the region including (1,1) is of interest, as it is necessary for $f(r) > r$ as $r \to 1$ for interactions to actually push the system toward a field where all dunes are about the same size. Additional lower regions where $f(r) > r$ will affect the timescale over which the system evolves, but not the end state. Even in simulations with a carefully paired influx dune population and interaction function (such as a strongly-peaked bimodal dune size distribution, with $f(r) = r$ at the ratio of the two peaks and $r_* = 1$), eventually a collision results in one dune of sufficiently different size that the field is pushed out of a patterned formation.

To further see that r_*, as defined, is the important parameter, we approximate the interaction function as a map from interval $[0, 1]$ onto itself. In a true discrete-time dynamical system where $f(r)$ is iterated over the unit interval, we have an invariant set $(r_*, 1)$ which is bounded by an unstable equilibrium point (r_*) and the stable equilibrium point (1) (i.e., applying $f^n(r) \to 1$ as $n \to \infty$, if $r \in (r_*, 1]$. Although this is not a perfect approximation to the interaction function (as dunes do not repeatedly collide with each other: although a given collision may have $r > r_*$, subsequent collisions involving those dunes may involve other dunes that are sufficiently different in size to yield $r < r_*$), the argument still applies as a collision which has $r > r_*$ will yield dunes which are each more likely to have subsequent collisions which involve $r > r_*$ (as the variance of the system has decreased, as discussed in Proposition 2).

Thus, for a dune field model to possibly form a stable patterned system, its interaction function needs to have $r_* < 1$. Generic interaction functions with this characteristic (in addition to those characteristics outlined in subsection 5.2.1) will be considered in constructing the dune field model.

In Diniega et al. (2010), we showed that the precise details of the interaction function are unimportant, and only the interaction function crossover value has a significant influence on the end state of the simulation. Based on this, we use simple piecewise-linear functions (Figure 5.8) for the remainder of this study, where the only adjustable parameter is r_*.

5.2.4. Other studies and their interaction functions

As we showed above, if $r_* = 0$ $(\forall r,\ f(r) > r)$, the system will always achieve a pattern of similarly sized dunes. Conversely, if $r_* = 1$ $(\forall r,\ f(r) \leq r)$, the system will

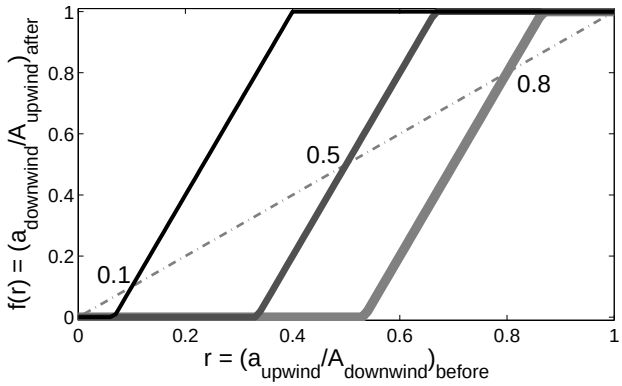

FIGURE 5.8. Examples of the piecewise-linear interaction functions used in the remainder of this study; $r_* = 0.1$ (thin), $r_* = 0.5$ (medium), and $r_* = 0.8$ (thick). Simulation tests showed the exact functional form is not important when considering the end state of the simulation – only the crossover value (r_*) matters. Thus, simple functions like these can be used as valid representatives of all reasonable interaction functions with the same r_*.

never have a stable patterned structure. This latter is the case we found with our two-dimensional simulations of colliding dunes (Figure 5.5): $\forall r,\ f(r) < r$, so zero was an attractive fixed point and the dune field moved toward perfect coalescence as long as collisions occurred.

This was an odd and unexpected result, as a study by Pelletier (2009) had managed to simulate the creation of patterned transverse dune fields (Figure 5.9) using a discrete model. A key difference between our model equations concerned the calculation of the shear stress exerted by the wind. In Pelletier (2009), a nonlinear correction was introduced to account for the added turbulence that develops as flow compresses over steeper slopes, causing a decrease in shear stress: $\tau = \tau_{JH}(1 - wh_x^2)$, where τ_{JH} is the shear stress calculated with the Jackson-Hunt model (Equations 3.1 and 3.2). In adding this modified shear stress calculation into the binary collision simulations, the interaction function did change in form (Figure 5.10) and was shifted upwards as $r \to 1$; however it still did not yield an $r_* < 1$. Additionally, even the use of the linear Jackson-Hunt shear stress calculation within the discrete model appeared to generate stable dunes (Figure 5.9). Thus, other differences between the model used in Pelletier (2009) and this study must account for the creation of the pattern, as the influences of collisions and sand flux are not sufficient. Currently, no continuum transverse dune model has resulted in a patterned dune field.

The interaction function derived for collisions between barchan dunes in previous studies (e.g., Durán et al. 2005) all have $r_* < 1$ ($r_* \sim 0.12$ in Figure 5.6), which

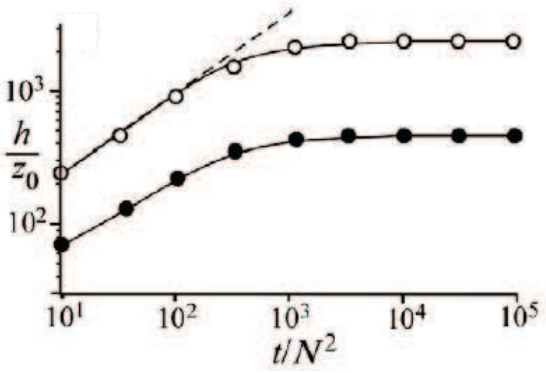

FIGURE 5.9. Plot of normalized bedform height (h/z_0) versus time for a discrete bedform evolution model using a linear (open circles) and nonlinear (close circles) shear-stress calculation (Pelletier 2009), based on an average of ten simulations. With short evolution times, height and spacing grow proportionately to the square root of time (dashed line); over long-times, the dunes reach a steady-state condition in which height and spacing do not increase significantly with time. Figure is taken from Pelletier (2009).

accounts for why those studies created patterned dune fields. We extend the results of those studies, in showing that when $r_* < 1$, the interaction functions *may* yield a patterned structure.

5.3. Field Model Description

As it is not reasonable to use the dune evolution model to examine the evolution and interactions of the hundreds of dunes within a field, a multiscale approach is instead used. Within the dune field model, the dunes themselves are treated as particles with morphologies and dynamics approximated using simple phenomenological relations, such as the interaction function.

5.3.1. Approximation of single dunes

Rather than keep track of every degree of freedom in the continuum model, it is useful to only track dunes according to their size and location. To determine when dunes are close enough to interact, we make reasonable assumptions about their morphology and zone of influence. Dune shape is assumed to be scale-invariant, approximated as a triangular wedge with a stoss aspect ratio of 10 (Parteli, Schwämmle, Herrmann, Monteiro & Maia 2005), a lee aspect ratio of 1.5 (angle of repose), and a separation bubble with an aspect ratio of 6 (Schatz & Herrmann 2006) (Figure 5.11).

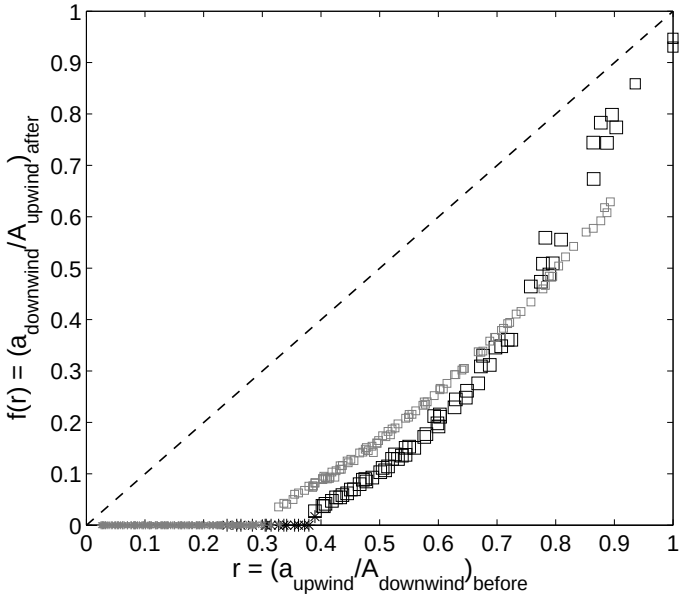

FIGURE 5.10. Interaction function (large black markers) found with a modified shear stress calculation, which takes into account the decrease in shear stress over steep slopes, due to turbulence that develops as flow compresses (Pelletier 2009). This function steepens for higher r values, as compared to the function found with our dune model (small gray marker), but still has $r_* = 1$. Markers follow the convention of Figure 5.5.

The dunes move with a velocity inverse to their crest height (Andreotti et al. 2002*a*); i.e., $v \sim k/H$. The coefficient k varies between actual dune fields (Bagnold 1941). In this study, it is arbitrarily set at $100m^2/yr$.

5.3.2. Interactions and initialization: particle model

We initially attempted to use a Smoluchowski coagulation-type study to analyze dune field evolution (described in Appendix C), as such equations are commonly used to describe the evolution of large populations (by evolving the number density P of particles of size x at a time t). Unfortunately, the dune field system sufficiently differed from the physical systems considered by Smoluchowski equations (such as molecular interactions within a vapor) that this approach became unwieldy: as sediment comes from a point or line source, it made more sense to use a semi-infinite field instead of periodic boundary conditions; secondly, dunes do not coagulate, but instead exchange mass when they collide. Thus, this approach was abandoned in favor of a deterministic particle model.

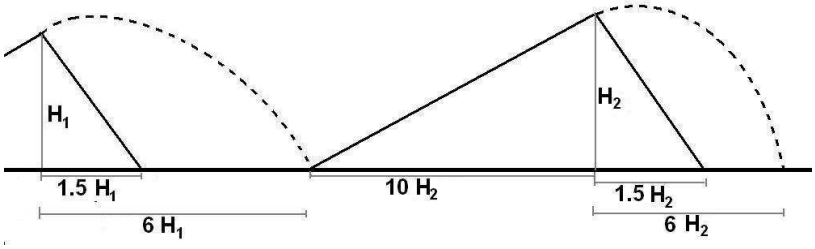

FIGURE 5.11. Approximation of the morphology of a dune, with fixed stoss aspect ratio of 10 and lee aspect ratio of 1.5. This shape is used to determine the dune's zone of influence as a function of area - two dunes interact when the separation bubble (with aspect ratio of 6) of the upwind dune touches the foot of the downwind dune, as shown.

Our particle dunes move within a one-dimensional semi-infinite field. Collisions occur when the foot of the downwind dune is touched by the separation bubble of the upwind dune. The distance between dunes after collision is calculated the same way, with the downwind dune located just outside the separation bubble of the upwind dune.

The results of dune collisions are governed by the interaction function, which relates the size ratio of the dunes before collision to the size ratio of the dunes after collision (as described and derived in subsection 5.2.3). In our dune field model, collisions occur instantaneously once dunes are close enough to interact.

Initial cross-sectional areas for the dunes (for either initial or influx dunes) are taken from a specified range with uniform distribution. When we consider a semi-infinite domain with an upwind influx of dunes, we assume a constant mass influx rate of $30m^2/yr$ to relate injection frequency to dune size. In general, this corresponded to ~ 1000 influx dunes per 1000 years for simulations run with a small mean dune size ($M = 40m^2$), and ~ 400 when a larger mean dune size ($M = 100m^2$) was used.

5.3.3. Model assumptions

Here we highlight and explain several assumptions we have made (in decreasing importance) in designing our dune field model:

1. *Sand flux effects are ignored.* This means that dunes only change size when they collide and the total size of colliding dunes is conserved during a collision (i.e., $(a + A)_{\text{before}} = (a + A)_{\text{after}}$). In reality, sand can be lost or gained by dunes between and during collisions (Elbelrhiti et al. 2008). Including this sand flux, however, adds an additional layer of complexity on the model, and such processes are not currently constrained by observations or experiments.

The effect this assumption may have on simulation results will be addressed in subsection 5.4.3.

2. *The interaction function is assumed to be spatially and temporally constant.* Dune collisions occurring at different times or locations are assumed to obey the same interaction function. The interaction function, however, may depend on local conditions, such as the type of sand included in the dunes. As timescale is not considered, in this study it is not important that the interaction function may change shape. If the interaction function crossover value should change temporally or spatially, however, as is suggested in Besler (2002), then this could impact the end state of the dune field. The physical implications of this will be discussed in subsection 5.4.3.

3. *Collisions happen instantaneously.* We considered this to be an acceptable approximation as we observed that the time between collisions was much longer than the collision timescale in our simulations. Additionally, this simplifies the collision-dynamics as only two dunes can collide at a time.

4. *Dune sizes are chosen from a uniform distribution.* Although physical systems generally have other types of distributions (e.g., Gaussian), a uniform dune size distribution will be used in this study as its structure is the simplest. This will remove one level of complexity from analysis of simulation results. Additionally, we will discuss the effect of a Gaussian distribution of dune sizes in subsection 5.4.3.

5. *The dune shape and zone of influence are specified somewhat arbitrarily.* Both of these will affect the timescale of dune field evolution, and the zone of influence directly relates to the interdune spacing of a patterned system. These values will have no effect, however, on whether or not a system will form stable similarly-sized dunes, which is the focus of this study.

6. *The value of the constant influx rate and the coefficient in the velocity relation are also arbitrarily specified.* Again, both of these constants will play a role in the timescale over which the field attains its end state. As long as dunes are not injected on top of one another, they have no other influence on the simulation.

5.3.4. Possible field end states

This study is concerned with the *long-time* behavior of dune fields – with this assumption, a dune field can evolve towards two possible outcomes: (1) a dynamic equilibrium is established where all dunes are and remain similar in size; we call this end state *quasi-steady* (for example, the crescentic dunes in White Sands, New Mexico or the martian dune field shown in Figure 1.2); or (2) the field may undergo *runaway growth*, with one or a few dunes continually growing through coalescence with upwind

dunes (a possible example of this type of dune field structure on Mars is shown in Figure 1.3).

Let us emphasize that because we are concerned with only the end state of a simulation, the exact timescales for evolution are not considered in the following tests. The effect timescale will have when model results are compared with actual dune fields will be discussed in subsection 5.4.3.

In the *quasi-steady* end state, all dunes have approximately the same size and interdune spacing – the epitome of a patterned dune field. The field will evolve into the following characteristics:

- Since the dunes will become similar in size, they will move with approximately the same velocity and, thus, rarely interact with each other.
- The interdune spacing will be similar across the field, as this quantity depends on their defined zone of influence, which depends on their size (subsection 5.3.2).
- Even if new dunes with a range of sizes are introduced (e.g., through an influx condition), interactions ultimately yield dunes of similar size with the rest of the field.
- This end state is characterized by a linear increase in the number of dunes and a steady mean dune size.

In the *runaway growth* case, one or a few dunes become large enough relative to their surrounding dunes that all future interactions occur between very disparately sized dunes (r small), which results in the larger dune getting still larger (and coalescing with all smaller upwind dunes). This will result in the following characteristics:

- The system will eventually settle into a size-sorted field, with dune size monotonically decreasing with distance from the upwind boundary.
- Influx dunes will generally be smaller than the dunes found at or near the beginning of the field, so will interact with a few dunes at the beginning, generally losing sand and eventually coalescing with an anomalously large dune.
- This causes the number of dunes in the field to be quasi-constant.
- If periodic boundaries had been used, then no size-sorting can occur and the final outcome is just a single large dune.

5.4. Results

Our results show that a dune field's end state depends only on the interaction function crossover value and influx dune size distribution's standard deviation/mean ratio. The way in which these two parameters are coupled can be seen most clearly in Figure

5.12, which shows a simulation's end state as a function of r_* and σ/M. A boundary between parameter values yielding a quasi-steady or runaway growth end state clearly exists. To understand this coupling, we utilize a probabilistic approach to predict the evolution of a dune field.

5.4.1. Threshold between end states

As it is not clear how to estimate the probability that a dune field will enter a specific end state, we instead ask how probable it is that a single collision involving an individual downwind dune of mean influx size (M) will involve an upwind influx dune of size a such that $r = a/M > r_*$, or $a > Mr_*$? As discussed in subsection 5.2.3, interactions involving $r > r_*$ push the dune field towards a quasi-steady end state because the collision results in more similarly-sized dunes.

The reason that the probabilistic outcome of an individual dune collision should be related to the predictions of a dune field's end state is results from the nature of the runaway growth end state: the runaway growth end state involves a small number of dunes becoming substantially larger than the rest of the dune field through collisions. If the probability is low that interactions between subsequent influx dunes (i.e., near the beginning of the dune field) will yield dunes more similar in size ($r > r_*$), then it is more likely that a single dune can eventually become disparately large enough to enter into runaway growth. Furthermore, as runaway growth involves a dune growing through collisions, the initial size that we consider is somewhat arbitrary – so we consider the probability with regards to the mean sized influx dune.

We hypothesize that calculating the probability that $a > r_*M$ for the lowest r_* which yields runaway growth will yield insight about the boundary between the possible simulation end states. The results of many simulations are shown in Table 5.1, where it can be seen that the probability at the boundary between the two end states is consistently very large. We can see in Figure 5.12 that as long as the size distribution of the influx dunes is not overly wide ($\sigma < 0.5M$), even with a 90% probability that any single interaction will involve a mass ratio $r > r_*$ and will yield more similarly-sized dunes, the simulation will still achieve runaway growth.

Physical implications of this probabilistic analysis are discussed in subsection 5.4.3.

5.4.2. Influence of other model parameters

We have shown that whether or not a dune field model achieves a patterned structure depends intimately on the interaction dynamics and dune formation. Thus, both of these processes need to be well constrained before a model can be compared to a physical dune field. If one is only interested in predicting the end state of the simulation, however, just one parameter in dynamics (the interaction function crossover value) and and one parameter in dune initialization (the influx condition's standard deviation/mean ratio) need to be constrained. Theoretically, if an actual dune field is

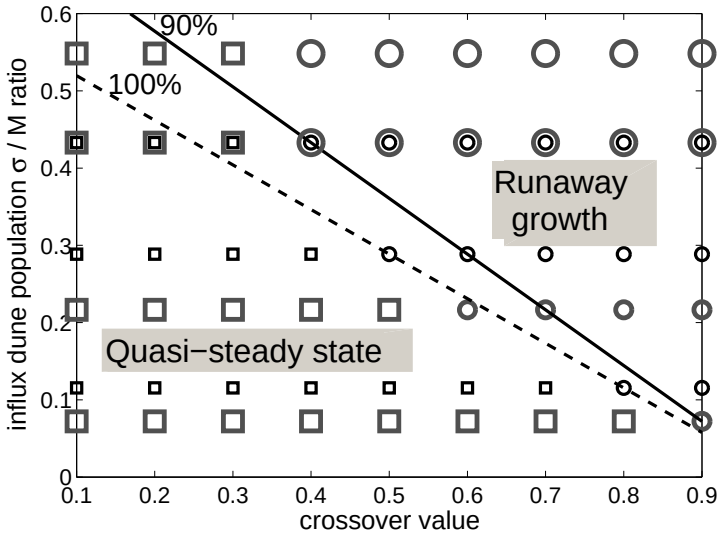

FIGURE 5.12. Plot showing the model end state, as a function of the interaction function crossover value and the standard deviation/mean ratio (uniform distribution). Notice the clear boundary between the regions corresponding to each end state: quasi-steady state (squares) vs. runaway growth (circles). This boundary is consistent between simulations with a mean influx dune size of 40m^2 (small point markers) and 100m^2 (large point markers). Additionally, it is not linear, but is roughly bounded (when standard deviation < 0.5 mean) by the trendlines corresponding to a 100% (dashed) and 90% (solid) probability that a collision involving a downwind mean-sized dune will have a mass ratio $r > r_*$ and thus result in two similarly sized dunes.

dune size range [m^2]	mean size (M)	threshold r_*	probability at threshold r_*
$10-70$	40	0.4	90%
$25-55$	40	0.6	100%
$35-45$	40	0.9	90%
$25-175$	100	0.4	90%
$50-150$	100	0.5	100%
$80-120$	100	0.8	100%

TABLE 5.1. Table showing the probability that a collision involving a mean-sized influx dune will yield more similarly-sized dunes, for simulations with different influx ranges, and at the lowest r_* yielding runaway growth. If the dune range given is the uniform distribution $[c, d]$, then the mean size $M = (c + d)/2$, and the probability $P(a > Mr_*) = 1 - P(a < Mr_*) = 1 - (Mr_* - c)/(d - c) = (M - Mr_* - \sqrt{3}\sigma)/\sigma\sqrt{12}$.

patterned and appears to be stable, then finding one of these two parameters should also yield information about the other.

Many other structural factors do affect the timescale over which the simulation achieves its end state, however, which by extension affects dune size and interdune spacing (Table 5.2). This means that unless a physical dune field has achieved its end state, these other factors (such as dune velocity and initial conditions) must also be constrained to reliably compare simulation results with observations.

5.4.3. Physical implications

As was shown in subsection 5.4.1, a dune field will achieve runaway growth even if a high probability (90%) exists that an average collision near the spatial beginning of the dune field will result in similarly sized dunes ($r > r_*$). An even larger probability is needed for the field to achieve a quasi-steady end state – which relates to a very careful coupling between the influx condition and the interaction function crossover value; given this, it appears surprising that most observed dune fields do not appear to be in a state of runaway growth.

Assuming the premise that the dune field model presented in Section 5.3 adequately captures the results of dune collisions, there are three extreme explanations:

1. Collisions are the dominant stabilizing mechanism for dune fields. Thus, for most dune fields to appear patterned, the physical system – both the environmental conditions which influence dune formation and the interaction dynamics – must naturally fall into the small window needed for this to occur.

2. Collisions may play a role in redistributing sand from large dunes to small dunes, but the model is incomplete. Other processes (e.g., interdune sand flux

Structural element		Effect
Interaction function:	Form (e.g., steepness)	timescale
	Extent of coalescence zone	timescale
	Multiple regions of $f(r) > r$	timescale
	Crossover value	*end state*
Initial conditions:		negligible as long as not containing dunes overly large compared to the influx, and sufficient time is given for them to be assimilated/run ahead
Influx condition:	Mean value	timescale
	Standard deviation/mean	*end state*

TABLE 5.2. A summary of different dune field model components, for a model with semi-infinite boundaries, and the effect each component has on the model's end state results. Any component which affects timescale will also affect dune size and spacing evolution. In this study, we were primarily interested in the simulation's end state.

or intrafield dune nucleation) or factors (e.g., variations in influx) are needed to increase the stability of patterned dune fields.

3. Patterned dune fields are not stable landforms. The timescale over which a dune field destabilizes, however, is very long compared to the timescales over which its environment changes.

The first point is a plausible explanation for barchan fields, as numerical simulations of barchan dune interactions yield interaction functions with very low crossover values, which means the influx distribution does not need to be tightly constrained for the dune field to possibly become patterned. For example, Durán et al. (2005) found an $r_* \sim 0.12$ (volume ratio) for zero-offset collisions between barchans (Fig. 5.6). Using a crossover value that low in this model (translated to $r_* = 0.16$ for the cross-sectional area ratio by Lee et al. (2005)), and assuming a uniformly distributed area influx starting with 10m^2 ($\sim$ 1m height), the upperlimit on the influx distribution can be as high as 110m^2 ($\sim$ 5m height) and the system will still achieve a quasi-steady state. Additionally, even if the crossover value is higher, it seems reasonable to assume that dune initialization should result in a narrow range of dune sizes, so still yield a quasi-steady end state.

In Section 5.2, we showed, however, that simulations of transverse dune collisions yield $r_* = 1$. In this case, if transverse dune fields do achieve stable patterned structures, the second explanation must be correct. Alternatively, the third point is

correct (or the original premise is wrong).

The second explanation (that the model is incomplete) needs to be carefully evaluated, as size- or age-dependent dune field stabilizing processes do occur. For example, large barchan dunes can be destabilized through wind variations and dune collisions, as long-wavelength perturbations form on the flanks of these dunes and break away. This prevents any dunes from becoming overly large and increases the likelihood that a dune field will remain patterned. Intrafield dune destabilization has been studied in the field (Elbelrhiti et al. 2005, Gay 1999), in the laboratory (Endo, Taniguchi & Katsuki 2004), and in three-dimensional continuum simulations (Durán et al. 2005, Katsuki, Nishimori, Endo & Taniguchi 2005, Elbelrhiti et al. 2008).

The results of dune collisions may also depend on local conditions, such as the age of dunes involved or the type of sand making up the dunes. In Besler (2002), on-going dune collisions were studied in different fields in the Libyan desert, and the apparent collision results in each locale were compared with the dunes' granulometrics. In that study, it was hypothesized that a downwind dune made of softer and finer grains was more likely to coalesce with the colliding upwind dune, while a downwind dune made of more compacted and coarser grains was more likely to have a collision result in ejection. As younger/smaller dunes are more likely to contain softer, finer grains, and older/larger dunes are more likely to contain more compacted, coarser grains (Besler 2005), this would mean that large dunes would be less likely to coalesce and enter runaway growth.

The rate of sand redistribution through these processes and/or their effect on the dune field's interaction function, however, still needs to be quantified through numerical simulation, observation, and/or laboratory experiments, before these processes can be included in a dune field model.

The final explanation is in reference to the fact that, in this model, the timescale of collisions was ignored and the rate of migration and dune injection were arbitrarily specified. This is acceptable as long as we are concerned only with the dune field's end state. However, if the timescale over which a dune field achieves runaway growth is overly long, environmental conditions may vary or the dune field may run into a physical boundary long before the dune field will reach this state. Currently, there is no reason to expect that the timescale over which runaway growth occurs should be very long. In this study, our choice of parameters yielded timescales on the order of a century (which is consistent with estimates by Hersen et al. (2004)).

However, long timescales may play a role if the actual distribution of dune sizes is strongly-peaked. With simulations that were run with Gaussian influx dune size distributions (with comparable σ/M as were used with uniform distributions, and with a low-end cutoff at 1m^2), runaway growth occurred at lower crossover values (Fig. 5.13), but after much longer time periods ($10 - 100$ times longer). This was unexpected, because we had hypothesized that a peaked distribution could have the same standard deviation/mean ratio value as a uniform distribution, and be far less

likely to have a sufficient number of small r interactions for the dune field to achieve runaway. The 'tails' of the distribution ended up being more influential than the peak, however – very large or very small dunes had a very low probability of being injected into the dune field, but after a very long time it was more likely that an apparently 'stable' patterned dune field would become destabilized and enter runaway growth.

The peaked nature of the distribution did exert a 'stabilizing' influence on transitory dune field dynamics – in a few cases with intermediary r_* values, a field would appear to switch from quasi-steady state to runaway growth and then back. Additionally, when simulations were run with tail-less Gaussian distributions (which is a more physically realistic distribution), the observed decrease in the threshold crossover values disappeared. The impact of using a realistic influx dune size distribution should be more thoroughly studied in the future.

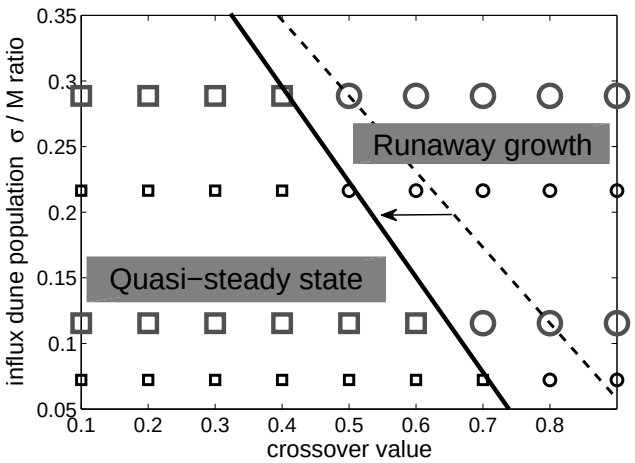

FIGURE 5.13. Plot showing the model end state, as a function of the interaction function crossover value and the standard deviation/mean ratio (Gaussian distribution). Notice that the boundary between the regions corresponding to each end state (roughly demarked by the solid trendline): quasi-steady state (squares) vs. runaway growth (circles), is at lower crossover values as compared to the results with uniform distribution (dashed trendline). However, simulations required $10-100x$ longer times to achieve an end state. Additionally, the left shift in the boundary disappears if the tails are removed from the Gaussian distribution. As in Figure 5.12, the size of the point-markers denotes the mean of the dune size distribution.

5.4.4. Possible future model improvements

As discussed in the second point in subsection 5.4.3, some additional physical processes may need to be included before the model can provide a sufficiently complete

picture of dune field evolution. For example, the model may be improved by including (i) sand flux between and during collisions, (ii) dune destabilization between and during collisions, and (iii) variations in the influx condition or interaction function. Additionally, if the model is to be expanded to consider evolution of a three-dimensional dune field, dunes would be able to split into more than two dunes after a collision (Durán et al. 2005, Katsuki, Nishimori, Endo & Taniguchi 2005).

As long as the processes and effects considered are assumed to occur during a collision (such as sand flux, dune destabilization, and/or a higher number of resultant dunes), then the model would not need to significantly change in structure. The effects of sand flux and dune destabilization during a collision could simply be added into a higher-dimension interaction function (e.g., the total size of the dunes and the size ratio after collision could be a function of the size ratio and total sizes of the dunes before collision), and the interaction function could reflect the formation of more than two dunes by calculating multiple after-collision size ratios. Thus, although the function would doubtlessly be much more complex, it is unlikely that the nature of its effect on the dune field's end state would significantly change from what is presented in this study; i.e., it is likely that the "crossover surface" would still be the only influential component of the interaction function in the analysis about the end state of a dune field.

Another possible addition to the model would be to include temporal or spatial variations in the interaction function (e.g., because of granulometric sand type changes in the dunes (Besler 2002)), or temporal variations in the influx condition (e.g., because of changes in local vegetation or sand supply). In this case, the range of possible r_* and/or σ/M values, and the rates of parameter change would need to be incorporated into the analysis, as those factors could push a dune field between end states. For example, if the interaction function crossover value could widely vary over short time/spatial scales, a dune field that would be expected to enter runaway growth at the mean crossover value could in fact be stabilized as large dunes would break up before becoming sufficiently larger than the surrounding dunes. If, instead, the influx dune population's standard deviation changed over long time periods, an apparently patterned dune field could be destabilized.

Furthermore, if the variation in range and period of these parameters were properly coupled, it should be possible to see oscillation between the two end states. In fact, all of these different types of behavior (apparently runaway $\rightarrow$ patterned, apparently patterned $\rightarrow$ runaway, and oscillatory) have been observed in simulations with a Gaussian distribution of influx sand dunes (see subsection 5.4.3).

To complete the model, it may also be necessary to allow dune evolution between collisions – such as through sand flux or dune destabilization. These types of inter-collision processes, however, would be more problematic to add into the model, as now dune evolution is partially uncoupled from the collisions. New analysis would needed to carefully determine inter- and intra-collision dune size evolution functions,

and related parameter(s) would need to be constrained.

Finally, if we are to include temporally or spatially varying parameters, and/or inter-collision dune evolution in the model, then timescale becomes an important concern. Dune evolution can now occur continuously (e.g., through intra- and inter-collision sand flux), semi-periodically (e.g., with a varying influx condition), or even stochastically (e.g., storm-caused destabilization of large dunes). With these different timescales, superimposed periodicities between dune growth and destabilization may occur, possibly resulting in pseudo-periodic or chaotic switching between the runaway growth and quasi-steady states.

As we can see, a more "complete" model can quickly become much more complex – and interesting. However, to properly include these processes in the model, identify influential parameters, and be able to derive predictions about a particular dune field, a far better understanding of these processes is needed. Thus, experimental and field work is vital in providing a quantification of the timescales and effects these different processes have on dune and dune field evolution.

6. INFLUENCE OF BEDROCK TOPOGRAPHY

As we have shown, interactions between airflow, sediment transport, and topography have a large impact on the formation and distribution of aeolian landforms, such as dunes; Chapters 2 and 3 described in detail how dunes are formed through a feedback between dune topography and wind-induced sediment transport. However, it is not well-understood how non-flat (non-erodible) bedrock topography will affect dune formation and evolution; despite (or perhaps because of) this, geological studies will often attribute strange dune forms to the effect of terrain. For example, the shape and orientation of Antarctic 'whaleback' dunes was attributed to underlying moraine structure (Calkin & Rutford 1974, Selby et al. 1974) (a study by Bristow et al. (2009) showed that this was not the case).

In this chapter, we investigate the effect of non-flat bedrock topography on isolated dune size and migration. Those results will then be extended to the effect that terrain will have on binary dune collisions, and related dune field evolution.

6.1. Physical Description

Numerical dune simulations are generally run with a flat bedrock layer, whose only effects are to halt erosion beyond a baseline (e.g., $h = 0$) and to enhance saltation over exposed bedrock. However, dune fields are found in non-flat environments: martian dune fields are often found inside of craters (Fenton et al. 2005) and mountains and valleys shape the dune fields on Earth (Gaylord & Dawson 1987, Wiggs et al. 2002) and Mars (Bourke, Bullard & Barnouin-Jha 2004). However, it is not well-understood how to include relevant topography within the model without greatly complicating the simulation or obscuring features of interest.

Additionally, detailed topographic information is often not available for inclusion in the models. In these cases, an understanding of the connection between dune morphology and underlying topography could be used to reverse-engineer estimates of terrain slopes based on observed dune morphology. For example, qualitative analysis of this type is currently being done for Titan. We have almost no topography information about this moon of Saturn, but comparative analysis between dune terminations on Titan and dunes in the Namibian desert has yielded information about the sign of topographical slopes (i.e., topographic highs vs. lows). In some places, this differed from topographical inputs to global atmosphere circulation models (Radebaugh et al. 2010); analysis of dune forms also yielded opposite wind directions (Radebaugh et al. 2008) from those predicted by the atmosphere model, but changing the topographical inputs yielded more consistent results (Radebaugh et al. 2010).

Here we present preliminary attempts to study the influence topography exerts on the migration and shape of an isolated dune. We will extend these results to

qualitatively estimate effects within large-scale and more complicated dune fields, but note that current numerical experiments have the following limitations:

- As the simulation is two-dimensional, the perturbations considered are perpendicular to wind flow, causing obstruction of sediment transport or sheltering effects. We do not consider the effect of channeled airflow or other three-dimensional effects.
- To more closely identify and quantify the influence of topography, we restrict ourselves to only small and simple perturbations: a Gaussian hill or an upwards or downwards step.

Future studies should consider more complicated underlying topography, and will require validation through quantatitive comparison with observed dune fields.

6.2. Influence of Terrain on Isolated Dune Evolution

Numerical experiments in non-dimensional space were used to investigate how dune shape and migration dynamics changed as a dune moved over topography – a Gaussian hill of specified height and standard deviation or an upward/downward step of specified height (Figure 6.1). Simulations were initialized with isolated dune profiles that were found to be steady-state over a flat surface, with dune area of 100-400. Results from these control simulations with dunes of size 120, 280, 400 (the results generally shown in figures) are listed in Table 6.1.

Dune area	height	length	migration velocity
120	7.53	43.48	0.3401
280	11.74	63.10	0.2227
400	14.09	74.33	0.1864

TABLE 6.1. Table showing dune shape and migration values over flat topography.

6.2.1. Over a smooth hill

As shown in Figures 6.2-6.4 (0.5, 1 and 5-high Gaussian hills, respectively), the dune's shape and migration rate varied both before and after encountering the hill, within a zone of perturbation. After encountering the hill, the dune adjusted back to its original shape and migration rate.

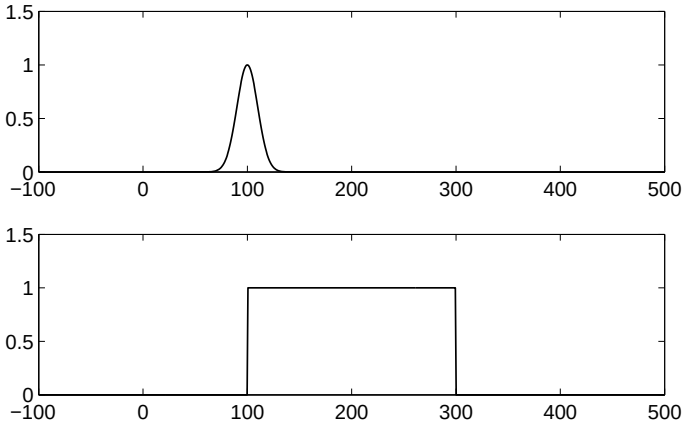

FIGURE 6.1. Diagrams showing simulation ground initialization for investigating the influence topography will have on dune migration and evolution. We focus on a bedrock Gaussian hill (top): $y = A\exp(\text{-}(x-100)^2/2\sigma^2)$ or upward/downward step (bottom): $y = \begin{cases} A & x \in [100, 300] \\ 0 & \text{otherwise.} \end{cases}$. The Gaussian hill example has height $A = 1$ and standard deviation $\sigma = 10$; the step example has height $A = 1$.

6.2.2. Over upward and downward steps

As was found with the Gaussian hill, the dune's shape and migration rate were changed upon encountering a step, and then readjusted within a zone of perturbation. Figures 6.5-6.7 show changes in dune migration rate, height, and length for steps of 0.5, 1 and 2-high, respectively.

Upon encountering the upward step, the lower portion of the dune became caught. This caused the dune crest to migrate faster, as effectively a smaller dune (the upper-portion only) was migrating forward, over the step. This caused the dune height to decrease and the dune length to increase. However, as the upper-portion moved forward, the lower portion of the dune was then exposed to the wind and began to also move over the step, causing the dune length to decrease (to less than the regular amount). Finally, after some distance from the step (which increased with both dune and step size), the dune adjusted to nearly its original shape and migration rate.

The reverse happened upon encountering the downward step. The dune initially slowed down when it reached the step, as sand was sheltered behind the step. As the sand pile behind the step grew to be taller than the step, the upper portions were exposed to the wind and began to migrate with a dune migration velocity higher than the original velocity. Eventually, most of the sand reaccumulated within the dune and it adjusted back to a steady shape and migration rate. When the step was

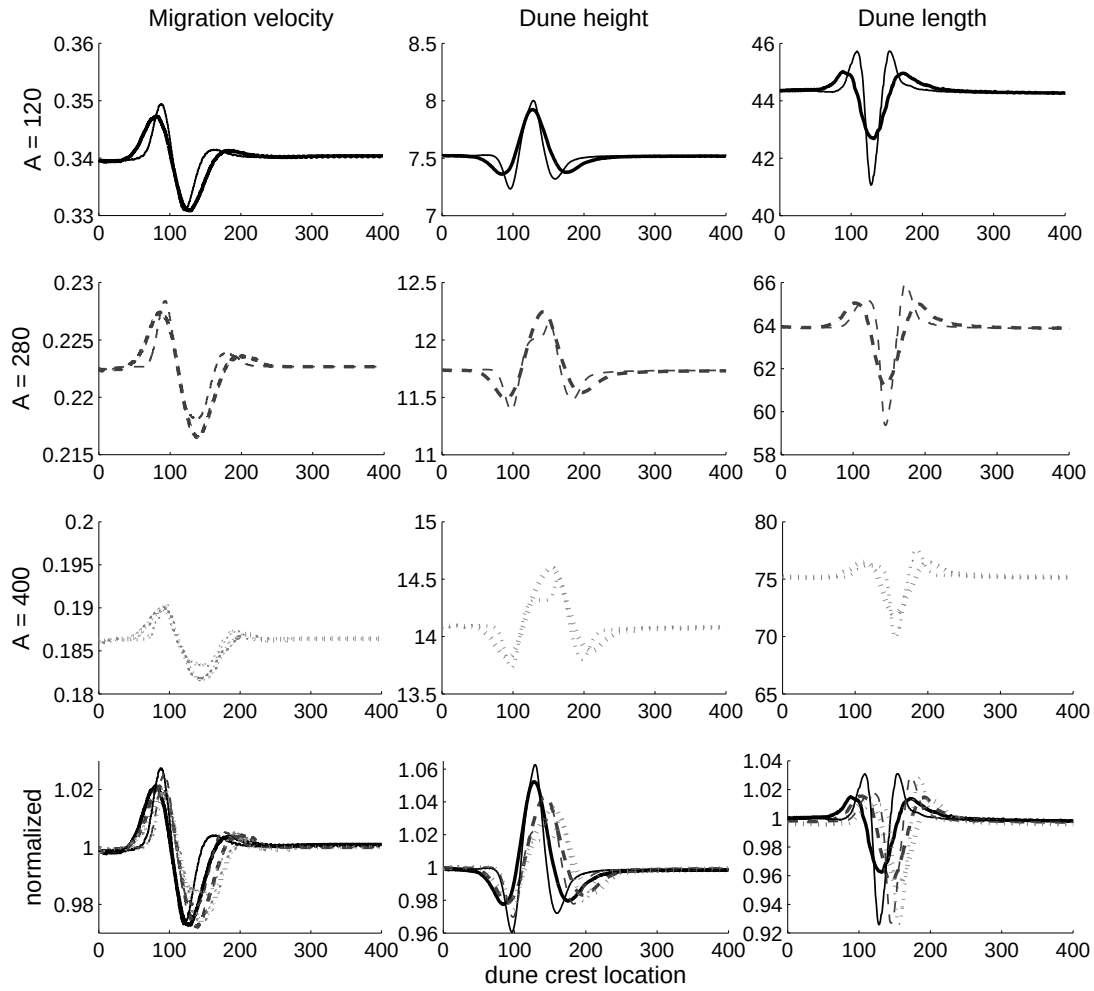

FIGURE 6.2. Plots showing the changes induced in dune migration rate, height, and length by a 0.5-high Gaussian hill located at 100, with standard deviations of 10 and 20 (thick lines). Dunes plotted had sizes of 120, 280, and 400; the bottom plots contain values normalized by the values found with no topography (Table 6.1).

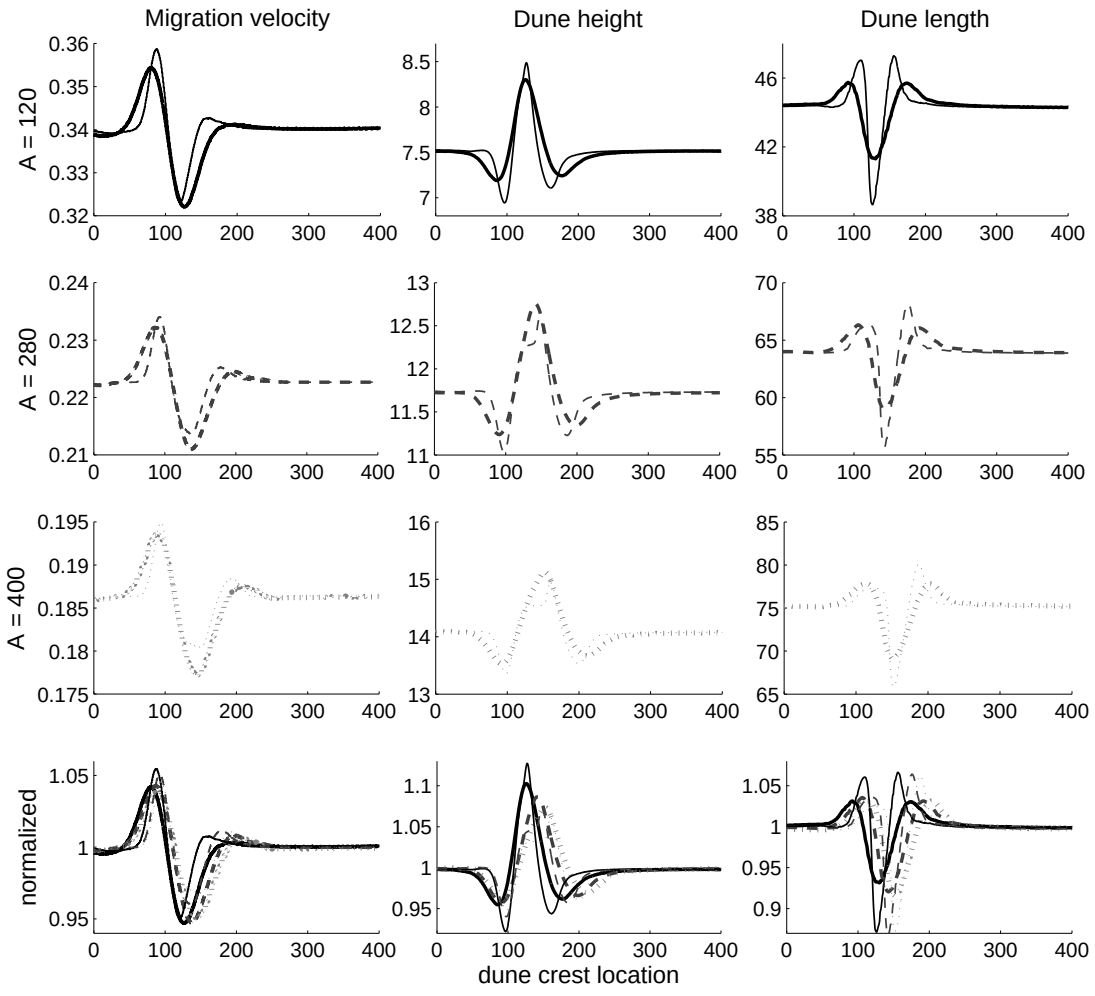

FIGURE 6.3. Plots showing the changes induced in dune migration rate, height, and length by a 1-high Gaussian hill located at 100, with standard deviations of 10 and 20 (thick lines). Details are as described in Figure 6.2.

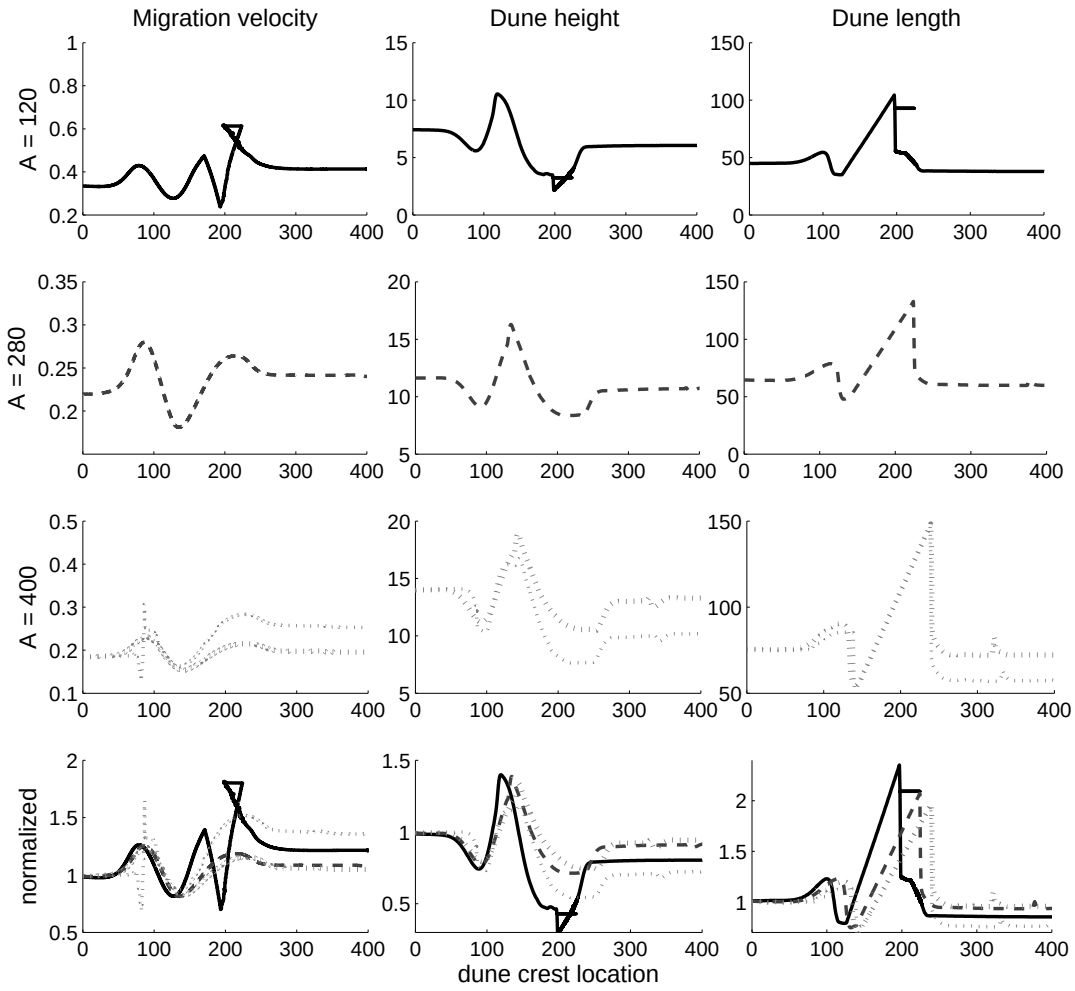

FIGURE 6.4. Plots showing the changes induced in dune migration rate, height, and length by a 5-high Gaussian hill located at 100, with standard deviations of 10 and 20 (thick lines). Strange behaviors occur when the dune height is comparable to the topography height; for example, the 120 dune (7.5-high) appears to move backwards as it encounters the 5-high hill, temporarily morphing into a two humped feature. Neither the 120 nor 280 dunes survive migration over the steep 5-high, 10-standard deviation hill (they both became stuck behind the hill, and slowly leaked sand), and even the 400 dune loses sand (height drops to ~ 0.75 original value). Plot legend is as described in Figure 6.2.

much smaller than the dune (e.g., Figure 6.5), the dune nearly-recovered its original shape and size. When the step was comparable to the dune height, a large fraction of the dune mass became trapped behind the backward step, causing the final dune size to be much smaller; this is especially visible in the differences between dunes in Figures 6.6-6.7.

6.2.3. Effect on isolated dune evolution

With both the Gaussian hill and steps, the change in dune migration speed (and associated changes in dune shape) depended primarily on the topography to dune height ratio (Figure 6.8); we found a near-linear relation between the maximal fractional change in velocity and this height ratio. Generally, the maximum change in velocity over an upward step was an increase, and the maximum change over a downward step and a Gaussian hill was a decrease. Exceptions occurred when the perturbing topography's height was large; in these cases, sand was lost to the sheltered lee of the topography or due to leakage during the encounter, which resulted in a smaller dune size and higher migration velocity.

We also investigated the length of the zone of perturbation (both before and after the topography; Figure 6.9) to investigate the spatial extent of transitory changes in dune shape and migration rate. We found that:

- The distance over which the dune was perturbed in shape and size before a step was independent of dune size and increased with the perturbation height. Before the Gaussian hill, the dune was perturbed much earlier (roughly one dune length); perturbation lengths in this case exhibited nonlinear dependencies on dune size and perturbation shape.

- After encountering either a step (upward or downward) or a Gaussian hill, the distance over which the dune adjusted back into a steady-state shape seems to depend on both the perturbation size and shape. In most cases, this distance scales roughly with dune length: $\sim 2-3$ times the pre-perturbation dune length.

6.3. Implications for Field Evolution

Based on these preliminary numerical experiments of how terrain changed the evolution and behavior of an isolated dune, we begin to estimate the influence of topography on dune field evolution.

6.3.1. Effect on dune collisions

Dune migration over topography will alter dune collision dynamics and the interaction function due to induced changes in dune migration velocity. Changes in dune velocity have a large influence on the amount of sand exchanged throughout a dune

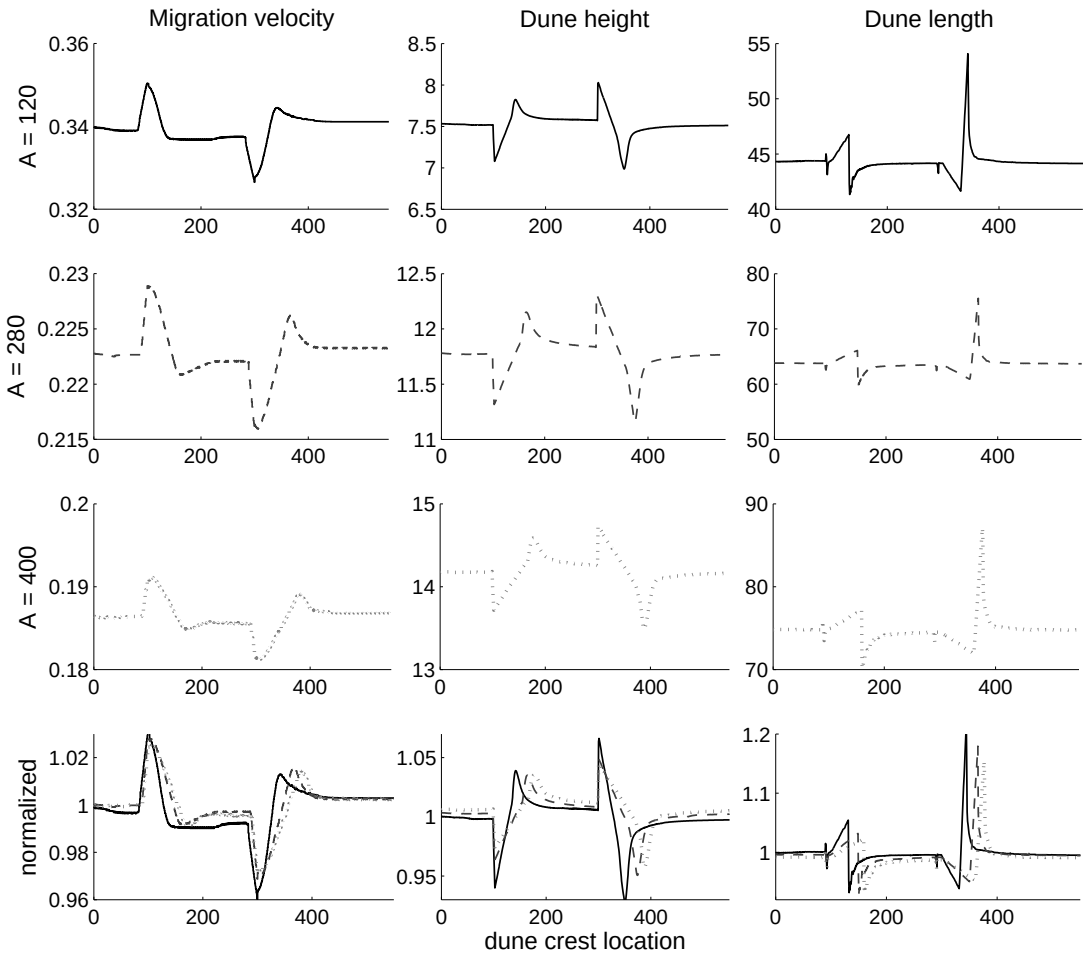

FIGURE 6.5. Plots showing the changes induced in dune shape and migration rate by 0.5-high steps, upward at 100 and downward at 300. Dunes plotted had sizes of 120, 280, and 400; the bottom plots contain values normalized by the values found with no topography (Table 6.1).

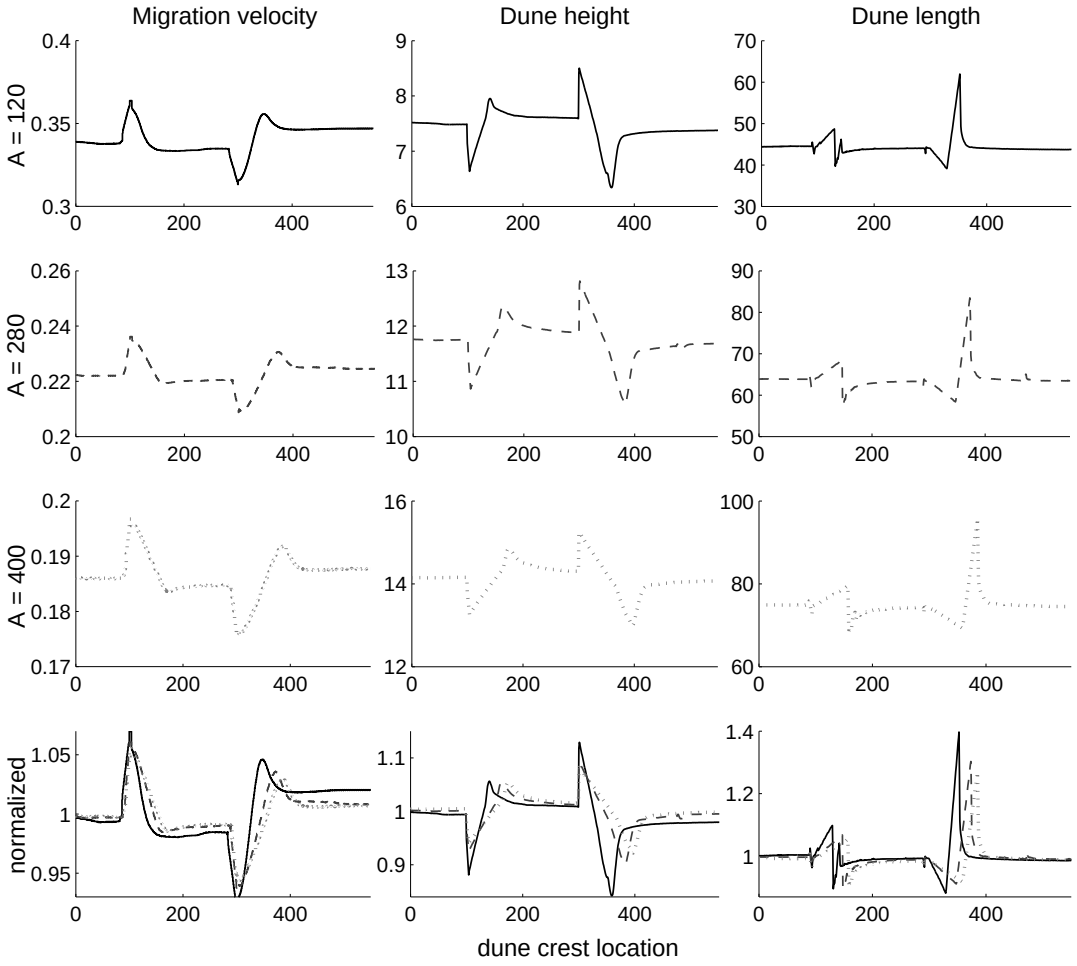

FIGURE 6.6. Plots showing the changes induced in dune shape and migration rate by 1-high steps, upward at 100 and downward at 300. Plot legend is as described in Figure 6.5.

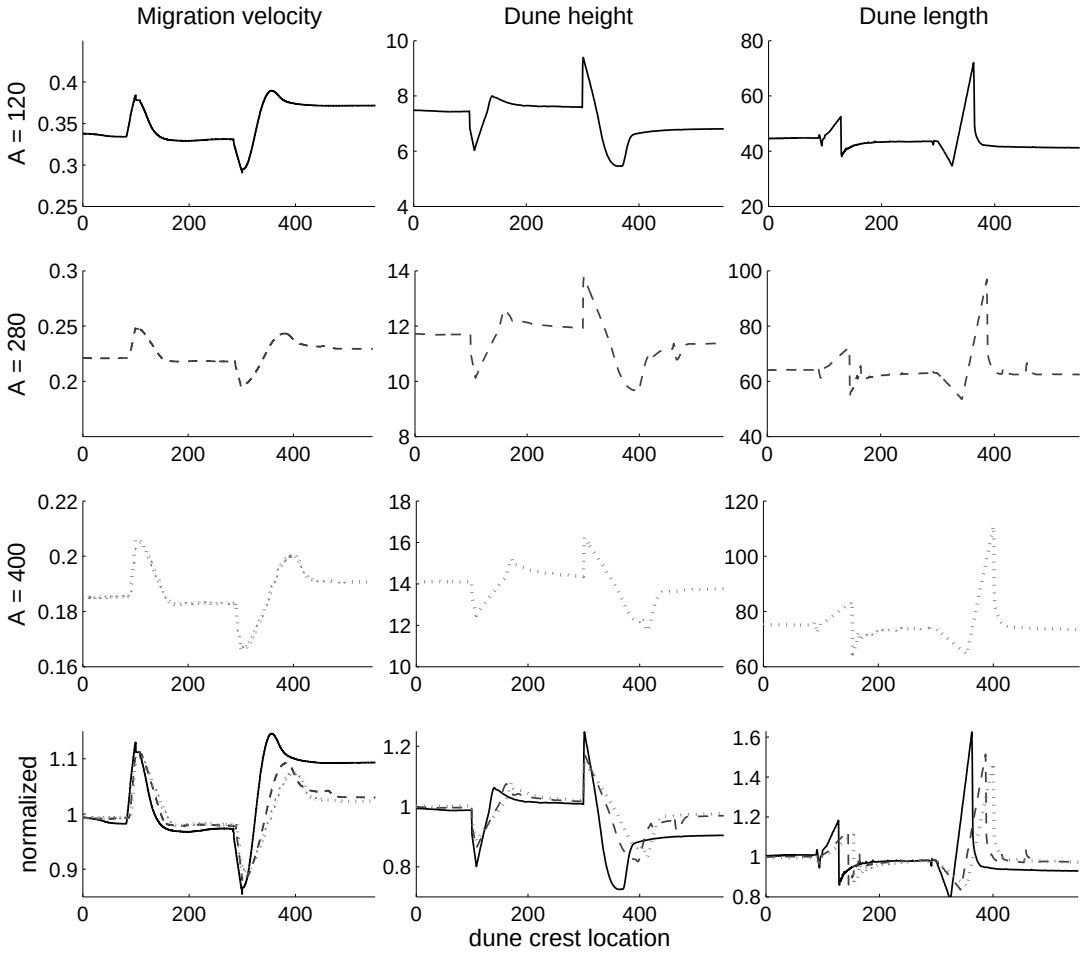

FIGURE 6.7. Plots showing the changes induced in dune shape and migration rate by 2-high steps, upward at 100 and downward at 300. Plot legend is as described in Figure 6.5.

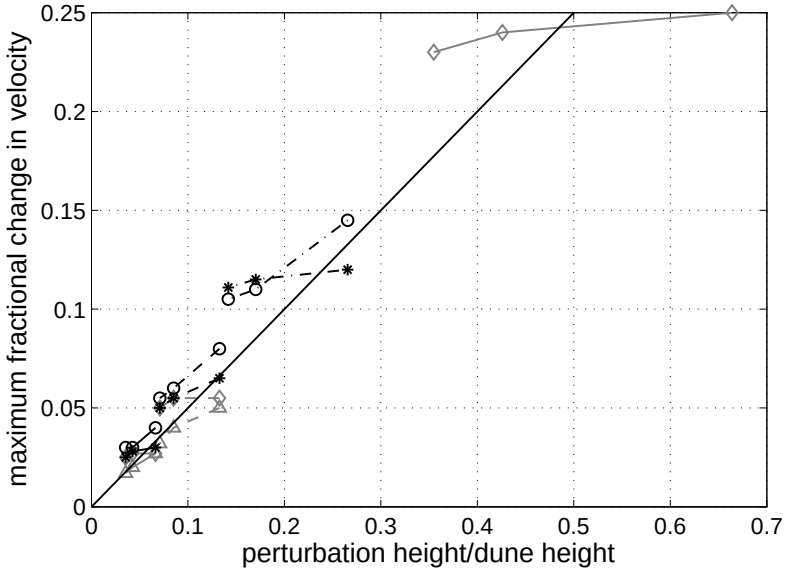

FIGURE 6.8. The maximal change in dune velocity (either increase or decrease) due to topography, either a step (black; * = upward, o = downward) or a Gaussian hill (gray; △ = standard deviation of 10, ◇ = 20). The line markers denote perturbation height: 0.5 (solid), 1 (dashed), 2 (dash-dotted), and 5 (dotted); they connect the values for different dune sizes: 120-280-400 (left to right within a sequence).

collision as this depends primarily on the timescale of the collision (as described in subsection 5.2.2). In this study, we consider only cases where topography is located downwind of colliding dunes; topography located upwind of dunes will perturb the shear stress exerted on the dunes (see subsection 5.1.2), but will not otherwise affect dune collisions.

Generally we found that the presence of topography will increase the likelihood of a dune collision to result in coalescence. In simulations run with Gaussian hills and downward steps, the non-flat topography caused a decrease in dune migration rate, causing the ejected dune to be slowed. This allowed the dunes to interact a second time, and for sand to be moved back from the smaller dune to the larger. Figure 6.10 illustrates a clear example of this: this collision resulted in ejection over flat terrain, but a downwind encounter with a Gaussian hill caused further sand exchange, resulting in coalescence and net sand loss. In other simulations where the topography was large relative to the ejected dune, sand was lost from this dune even if it did not re-interact with the upwind, larger dune; in either case, the downwind dune became smaller, making later coalescence more likely.

If it is possible for sand to be moved from the larger dune to the smaller, this

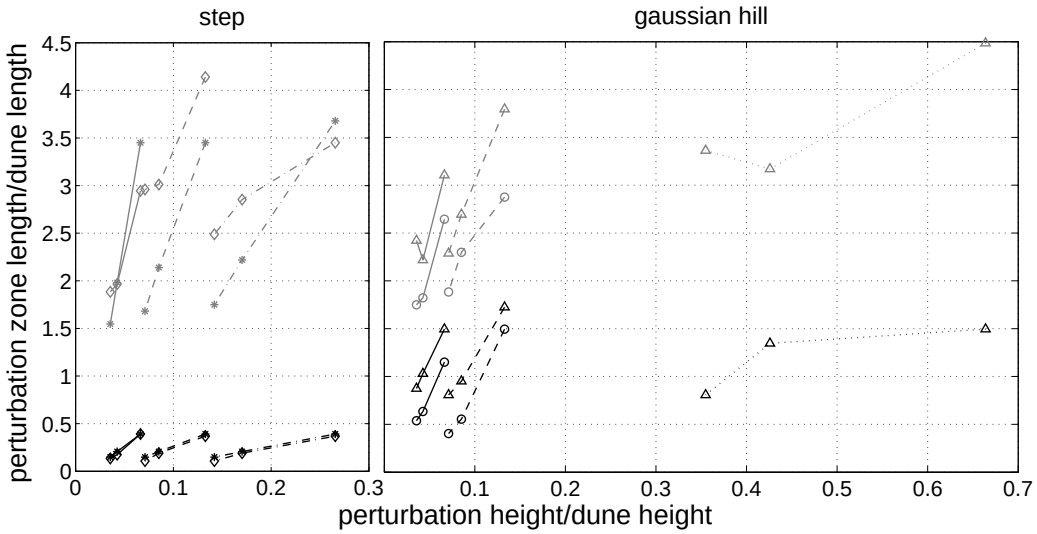

FIGURE 6.9. The perturbation zone length, before (black) and after (gray) the topography normalized by the dune length (before perturbation), as a function of perturbation height normalized by the dune height. The left plot shows the effects of an upward step (*) and downward step ($\diamond$), while the right plot shows the effects of a Gaussian hill with standard deviation of 10 (o) or 20 ($\triangle$). The line markers denote perturbation height: 0.5 (solid), 1 (dashed), 2 (dash-dotted), and 5 (dotted); they connect the values for different dune sizes: 120-280-400 (left to right within a sequence).

would instead result in a pair of dunes that are more similar in size. This could perhaps occur if the upwind dune become caught on large topography (such as a hill or upward step) and leaked sand to the smaller downwind dune. However, within these two-dimensional simulations, the topography would have first interacted with the smaller downwind dune, and would have exerted a greater effect due to the larger relative size. Thus, the net change in the downwind dune's size should still be to decrease in size.

In three dimensions, it may be possible for the smaller dune to bypass topography which catches the upwind larger dune. Additionally, topography that is less wide than the dune (and thus will exert three-dimensional effects) can perhaps cause a larger dune to break into several pieces. This has been shown to occur within barchan dunes due to wind variations (Elbelrhiti et al. 2005).

6.3.2. Effect on dune field pattern formation

Binary collisions within two-dimensional fields and occurring around and over non-flat topography appear to result in more cases of coalescence, or at least result in

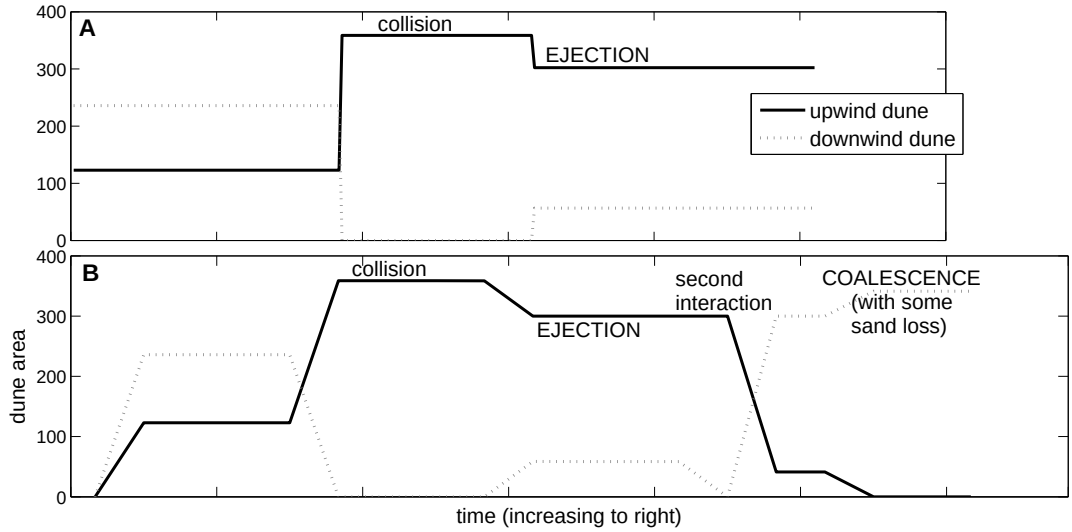

FIGURE 6.10. These plots show the size of colliding dunes (120 with 240) throughout a collision. In (A) the dunes collide on flat terrain: they briefly merge and then a small dune is ejected. (B) shows the perturbative effect of topography, as the presence of a 1-high, 10-standard deviation Gaussian hill downwind of the collision slows the ejected dune sufficiently to cause a second interaction, resulting in coalescence and net sand loss.

dunes of more disparate sizes. Individual dune collisions that result in sand transfer from the smaller to the larger dune pushes the system toward run-away growth (as discussed in subsection 5.4.1). Thus, it appears that topography, in affecting dune collisions, will have a destabilizing influence on pattern formation within transverse dune fields.

However, this influence can perhaps be dampened. For example, as dunes recover from their interaction with topography over a few dune-lengths (Figure 6.9), we would expect topography to exert a destabilizing influence only within closely-packed dune fields (where dune spacing is comparable to dune length). In dune fields with large-interdunal spacings, the influence topography will exert on dune collisions may be minimized. Alternatively, the development of sediment-rich interdune areas (such as those found in most transverse dune fields) can insulate the dunes from large bedrock topography, dampening the influence of terrain even within closely-packed fields.

Thus, bedrock topography may only affect dune collision dynamics under specific conditions. If these conditions occur only during an early period of transverse dune field evolution, this could cause an initial enhancement of coalescence within the field; the influence of topography may decrease as the field matures and allow the field to

stabilize (under the influence of other processes).

6.3.3. Inclusion of topography in the dune field model

As the primary effect of terrain on dune collisions and dune field evolution is related to variations in dune migration velocities, it should be possible to include topography within the dune field model outlined in Section 5.3 by:

- Letting the dune migration velocity (between collisions) be a function of proximity to terrain and the ratio of dune height to topography height. Simplifying assumptions will be needed to accomodate dependecies on topography shape.
- Modifying the interaction function to reflect changes in relative dune velocity when terrain is also involved in the collision. As in the first point, this will depend on the relative size of the topography with respect to the interacting dune and possibly on the shape of the topography.
- Sand leakage will need to be considered between and during dune collisions, when a small dune encounters large topography. Lost sand can generally be assumed to accumulate on the downwind dune (in two-dimensions).

Many more simulations and studies are needed to determine simple relations that will reflect the way that dune migration speed changes based on perturbation height (relative to dune height) and shape, and the distance over which terrain will exert an influence is felt. These preliminary results, however, do indicate that simple relations may be found for how the dune migration velocity varies with topography height (relative to dune height). The most complicated quantity appears to be the perturbation zone length.

These results also indicate that simple two-dimensional studies will only show enhanced coalescence within dune fields. More complicated dune field evolution processes (such as sand accumulation in the interdune areas) and three-dimensional effects may need to be considered to determine if topography can exert a stabilizing influence on dune field evolution.

7. AN APPLICATION: MARTIAN POLAR DUNES

In this chapter, we investigate the influence of reversing wind directions, diffusive processes, and ice cementation on dune slope evolution. The aim is to quantitatively connect specific morphologies to processes and environmental parameters, which will aid in the interpretation of actual dune forms.

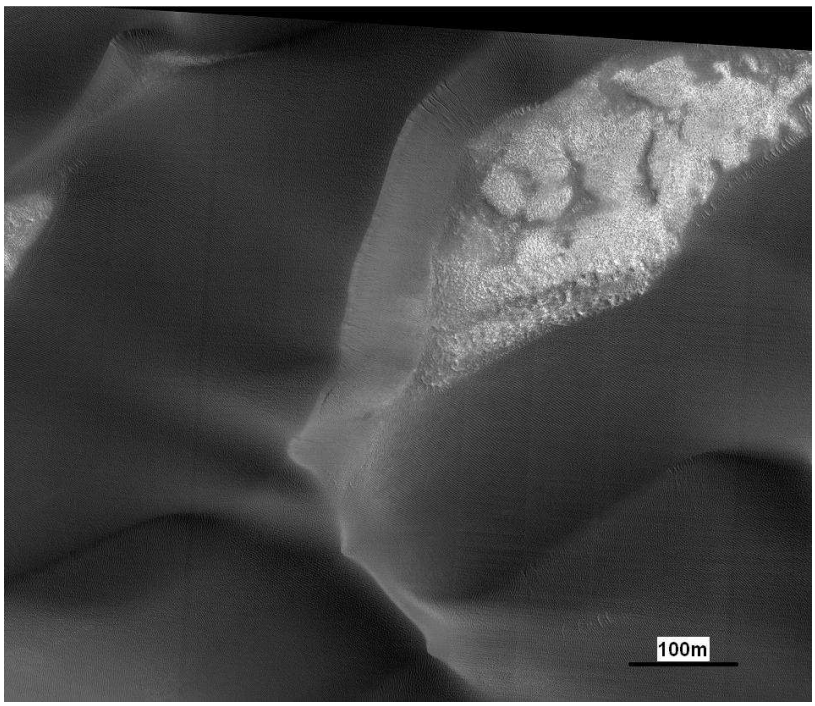

FIGURE 7.1. An image (HiRISE PSP_010269_2620; 81.7N,133.6E)of an example of the break in lee slope seen in many martian polar dunes. The appearance of a ∼10m wide "bright ribbon" along the dune brink is due to a lack of ripples and increased slope on the upper portion of the lee slope, relative to the lower portion.

This work was motivated by our observation that martian dunes located in the mid-latitudes and polar regions exhibit a break in slipface slope (Figure 7.1), which is not found elsewhere (Figure 7.2, 7.3). Within terrestrial dunes, this type of slipface morphology forms due to wind reversals (Koster & Dijkmans 1988, Burkinshaw et al. 1993, Bishop 2001, Bristow et al. 2010). Due to the apparent latitudinal control on where this feature is observed, we hypothesize that dune geomorphology may also be affected by cold climate processes, such the formation of an ice cemented core and/or

increased downslope sand transport.

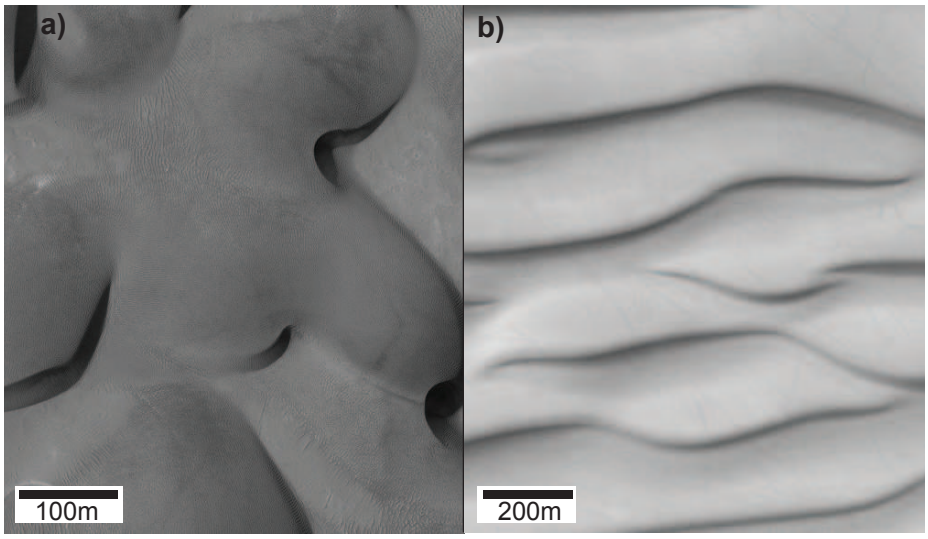

FIGURE 7.2. HiRISE images of other lee slopes seen on martian dunes. Image (a) shows examples of sharp, clean brinks and smooth lee slopes (PSP_010413_1920; 20N,79E). Image (b) shows examples of shallow and round lee slopes (PSP_006716_1220; 60S, 340E).

7.1. Physical Description

Antarctic dunes are studied as possible terrestrial analogues of martian polar dunes, due to similarities between their cold and arid formative environments. They also appear to share many morphological details, such as denivation features: fans, slumps, and visible ice layers have been observed within both cold-climate terrestrial (Bourke et al. 2009, Calkin & Rutford 1974, Steidtmann 1973) and martian dunes (Bourke 2005, Horgan et al. 2010). Within Antartic dunes, these features form due to the inclusion of inter-bedded sand, snow, and/or ice deposits (Bourke et al. 2009, Calkin & Rutford 1974). There is much evidence for subsurface water ice on Mars, in both the mid-latitudes and polar regions. In the North Polar Sand Sea on Mars, neutron current measurements and modeling results imply the existence of an ice-rich (and immobile) underlying topography with a relatively desiccated upper-layer ($\sim$ 6cm depth; Feldman et al. 2008), and recently-formed impact craters in the mid-latitudes have exposed near-surface pure ice (Byrne et al. 2009).

Understanding how cold climate processes will change dune evolution has important implications for present-day dune evolution on Mars, as such processes will slow landform migration. In cold-climate environments, dunes often are stabilized due

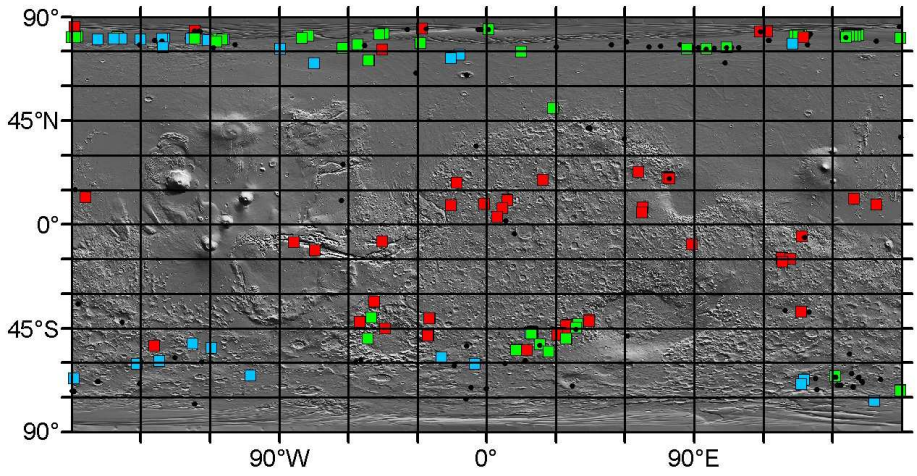

FIGURE 7.3. HiRISE images of dune fields were inspected to located dunes with "clean" and sharp slipfaces and crestlines (red), highly-eroded slipfaces and rounded crestlines (blue), and slipfaces with an apparent break in slope (green). Black dots denote dunes where viewing conditions (illumination and/or frost cover) made it difficult to discern the condition of the slipface.

to coverings of snow, ice-cementation, and possible increases to the threshold shear velocity of sand motion due to increased humidity (Lindsay 1973, Selby et al. 1974). Reversing (seasonal) winds will also slow dune migration, as the dune must now adjust its shape before migrating (Figure 7.4; Burkinshaw et al. 1993). Comparison of aerial photographs of Antarctic reversing dunes yielded a 40yr (1961-2001) average migration rate of 1.5m/yr (Bourke et al. 2009), while dating of stratigraphy within the same dunes yielded average migration rates of 0.05-1.3m/yr over 1300yrs (Bristow et al. 2010). This is much slower than the tens of meters per year migration rates of similarly-sized desert dunes (Cook et al. 1993, Gay 1999).

7.2. Influence of Reversing Winds

Winds that change direction by 180° will yield reversing dunes. These dunes can be differentiated from transverse or barchan dunes (which form in unidirection winds, as described in subsection 2.1.1) due to their steeper and/or non-smooth slopes that form as the stoss slope becomes the lee slope, and visa versa. On the new lee slope, free-falling sand piles up at the angle of repose on the upper-portions of the previously-stoss slope; on the new stoss slope, an apron of lower slope forms at the base of the previously-lee slope. Reversing dunes can be found within terrestrial desert (Bishop 2001, Burkinshaw et al. 1993) and cold climate dune fields (Koster & Dijkmans 1988, Bristow et al. 2010).

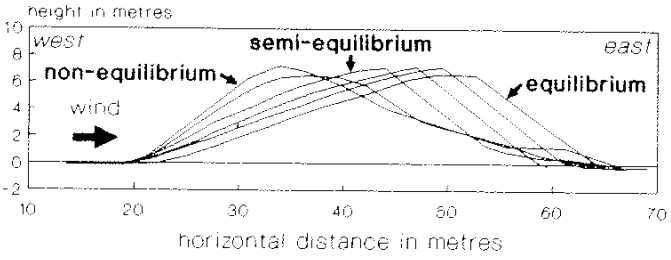

FIGURE 7.4. Dune profiles measured over a 7m high African transverse dune during the winter season (March to September), showing stages of dune reversal. During the summer the winds blow from the east, and during the winter from the north-west. Image is from (Burkinshaw et al. 1993).

A study by Fenton et al. (2005) showed the probable existence of reversing dunes in Proctor crater (47S, 30E) on Mars. These dunes contain slipfaces with three orientations and the kinked lee slope (Figure 7.5). Two of the slipface orientations coincide with predicted wind directions: within this intracrater dune field, geostrophic-induced winds blow from the west during the fall and winter, and katabatic winds blow from the east during the spring and summer. It is likely that similar reversing winds will be found in other intracrater dune fields and in the polar regions.

To investigate the influence that reversing winds will have on dune slope and behavior, we numerically experimented with different period lengths (duration of a cycle during which the wind blows to the left and then right) and ratios (the time the wind blows to the left versus to the right). Simulation parameters for sand flux were taken from a martian barchan dune modeling study (Table 3.1; Parteli & Herrmann 2007). Windspeed was held constant at 1.5 times the threshold value. Simulations were initiated with a dune formed under unidirectional winds blowing to the right.

As observed within terrestrial dunes (e.g., Burkinshaw et al. 1993), a reversing wind slows dune migration and steepens the dune's slopes (Figure 7.6). The amount of steepening depends primarily on the frequency of wind reversal (Figure 7.7, 7.8), and only weakly on the period of wind cycling and the dune size.

7.3. Influence of Diffusive Processes

Numerical experiments showed that dune slope values also depend on assumptions made about down-slope transport of sand (e.g., avalanching) that is modeled via diffusion. For example, reversing wind simulations run with a diffusion coefficient one order of magnitude higher yielded much lower slopes (Figure 7.9); this change in

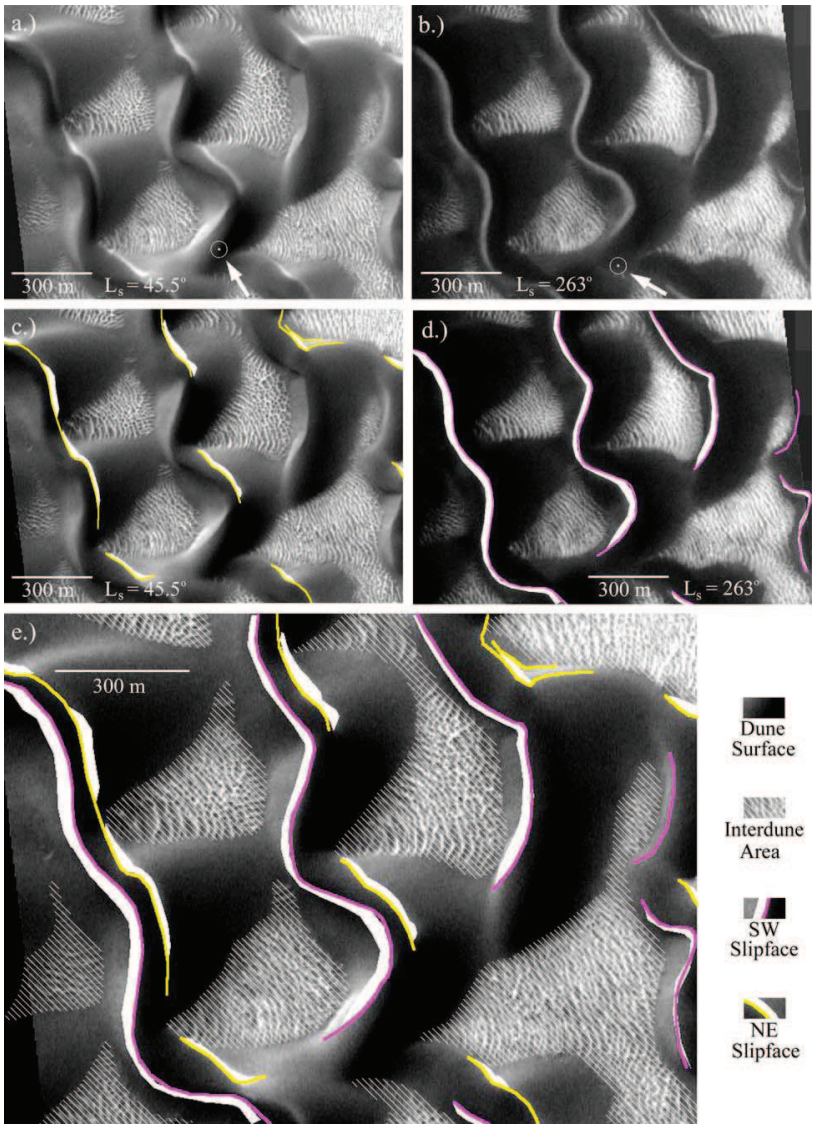

FIGURE 7.5. MOC images showing possible reversing slipfaces on dunes at the eastern edge of the Proctor crater dune field (47S, 30E). Images taken in the fall (a, MOC NA M19/00307) and spring (b, MOC NA E09/02707) show the same area with bright accumulations on opposing slipfaces. Figures (c) and (d) illustrate the locations of slipface brinks and bright accumulations. Figure (e) shows both sets of slipfaces and bright material. The movement of bright material is thought to be caused by a seasonal shift in wind direction. Image is taken from Fenton et al. (2005).

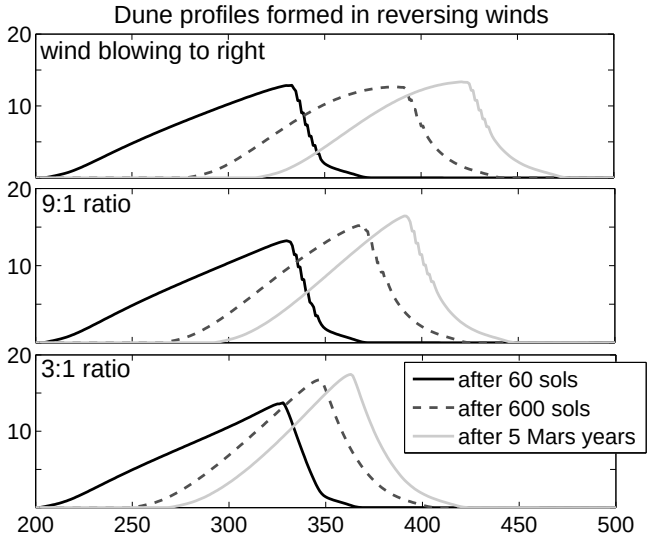

FIGURE 7.6. Under unidirectional winds, the dune migrates 97m; under 9:1 (9/10 of time wind blows to right, 1/10 to left) winds, 63m; and under 3:1 winds, 35m. The dune also grows in height, as its slopes steepen. The period used was six sols.

slope was comparable or larger than that resulting from adjustment to a wind reversal (Figure 7.7) or any other factors, illustrating that diffusion needs to be properly estimated before simulation results can be compared with observed dunes. In the physical situation, this dependence on diffusion reflects the fact that a dune's shape results from a competion between saltation (which piles sand and increases slope) and diffusion (which decreases slope).

In terrestrial desert dune systems, it generally can be assumed that diffusion is comparable in strength to saltation only within lee slope avalanches. In this case, as discussed in subsection 3.1.5, the diffusion coefficient is chosen so that diffusion operates on the same timescale as saltation when avalanches occur, and at a much longer timescale (increased by 2-3 orders of magnitude) otherwise. The effective diffusion, however, can be increased through any process that preferentially transports material downslope, such as atmospheric turbulence, creep, freeze-thaw cycles, seismic shaking, micro-meteorite impacts, or CO_2 sublimation (Figure 7.10).

Additionally, if saltation does not occur for a large fraction of time (due to sediment or wind limits), then simulation results and model time need to be scaled via this fraction to yield real-time results. As the diffusion coefficient is inversely related to time ($\sim$ length^2/time), this coefficient needs to be increased by the same multiplicative scale as time, to accurately reflect the effect of diffusion operating over the longer real-time period.

Current studies place martian dune evolution on timescales of ten-thousands of

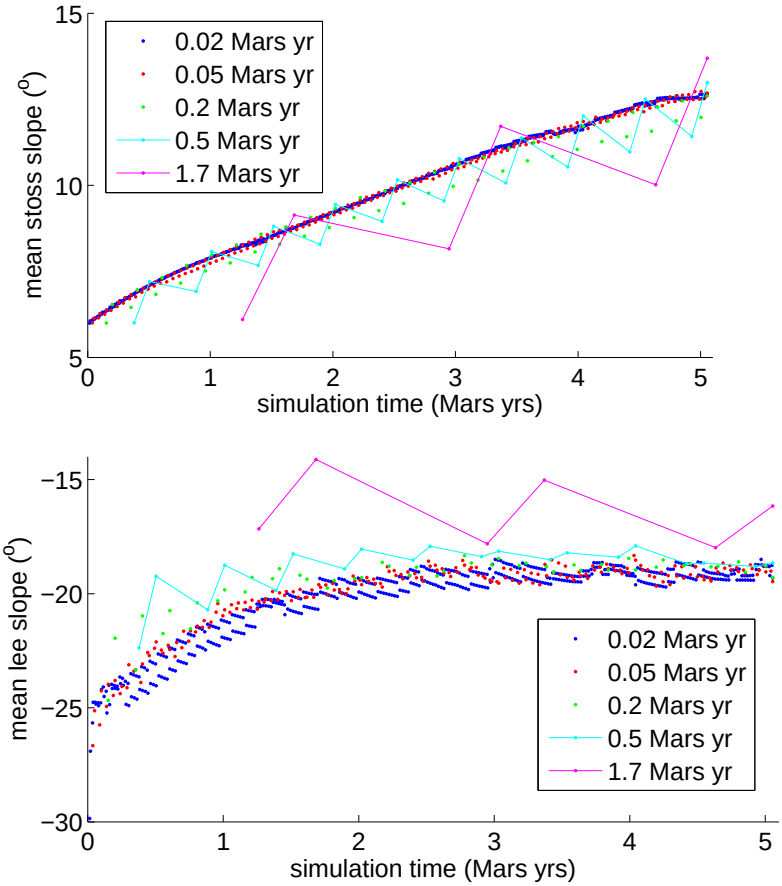

FIGURE 7.7. Simulations were run with a ratio of 3:1 for the time the wind blew to the right versus left, with different period lengths. Both stoss (upper plot) and lee (lower) slopes adjust to a mean value, with primary dependence on the ratio (not period length). The variance in average slope does increase with the period length, as the dune has a longer time to adjust to a wind direction before it reverses.

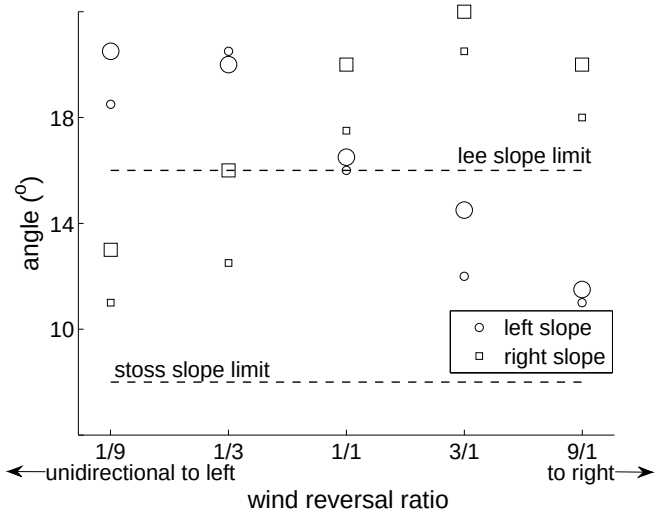

FIGURE 7.8. Both lee and stoss dune slopes adjust to a mean value that depends on the frequency of wind reversals, but is nearly independent of the period length (not shown) and dune size (large markers: dunes ∼30m high; small: ∼20m.). Dashed lines show effect of unidirectional wind, which is consistent in stoss values with observations (Burkinshaw et al. 1993, Parteli, Schwämmle, Herrmann, Monteiro & Maia 2005). The mean lee slope is lower than the angle or repose as calculations include smoothing at the top and bottom of the slope. This is the cause of the apparent oversteepening of the lee slope – as the wind reverses direction, the smoothing-portions of the previously-lee slope (which lie at very low slopes, especially at the foot of the slipface) are swept towards the dune and shortened.

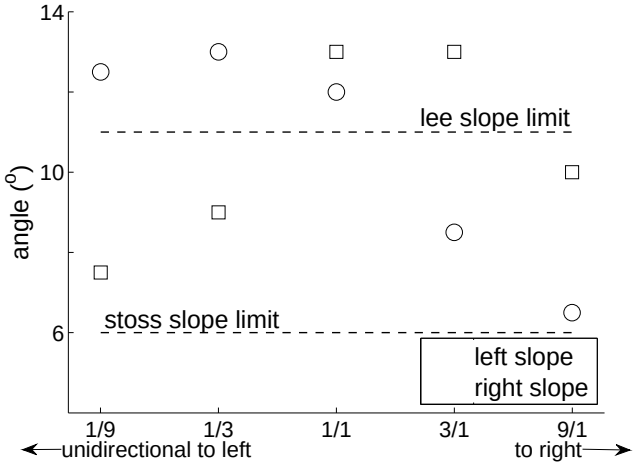

FIGURE 7.9. Simulations of dune evolution under reversing winds, but with a diffusion coefficient multiplied by 10 from that used to create Figure 7.8. Again, both slopes adjust to a mean value that depends on the frequency of wind reversals, but the dune is significantly shallower on both sides. Only the larger dune was used, as the smaller dune quickly became a symmetric, shallow heap.

years (Parteli & Herrmann 2007), comparable to estimates for climate shifts and cold climate processes. This was based on the assumption that the wind speed exceeds the threshold for saltation initiation only 40s every 5yrs (based on wind speeds recorded by the Viking spacecraft) – so simulation results were scaled by $\sim 10^7$. Although other studies claim that saltation should occur more often (Almeida et al. 2008, Kok 2010) due to the difference between the fluvial threshold and impact threshold for saltation, the current lack of observed dune migration makes it likely that a temporal scaling of at least a few orders of magnitude is necessary.

Recent martian dune modeling studies (e.g., Parteli & Herrmann 2007) have not accounted for this, but have created dune forms that look similar to martian dunes. This implies that the effective diffusion rate on Mars is comparable to the model rate, after scaling down by 10^7 (or whatever time scaling is necessary). Currently no estimates for diffusion due to stochastic processes exist. One study has estimated a diffusion rate of 2e-12m^2/s for ice-driven creep on martian debris slopes (Perron et al. 2003). This rate should be small relative to ice-driven creep within granular material (such as within dunes) and is probably much smaller than diffusion from aeolian/cold climate processes and avalanching, but provides us with a starting value. Scaling this diffusion coefficient by 10^7 yields a simulation diffusion rate of 2e-5m^2/s, which is comparable to the rate used in our simulations for avalanches (Table 3.1).

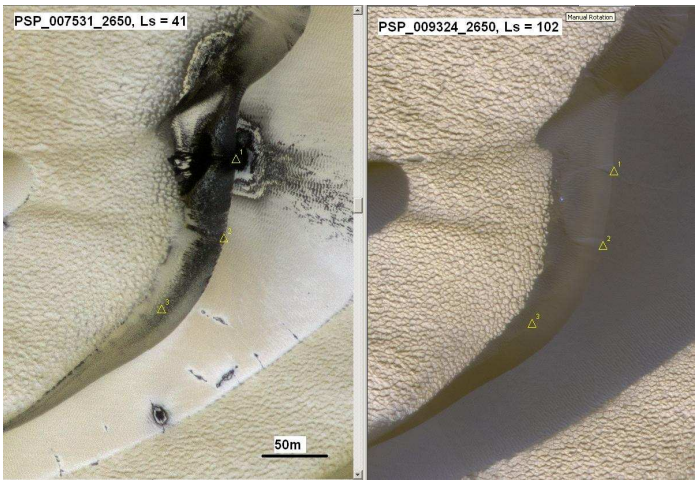

FIGURE 7.10. CO_2 frost coats these polar dunes (imaged by HiRISE; 84.7N, 0.8E). As the frost accumulates, it can become translucent ice and cause increased insolation heating at its base. This causes explosive vapor eruptions, which entrain dust and create dark spots, rings, and fans at the surface. Such activity can create small channels (Hansen et al. 2007) and mass-wasting events (localized slumps and avalanches) on the dune slope (Horgan et al. 2010). On this dune, there is a clear correlation between sublimation spots visible in spring (left) and small avalanche locations visible in summer (right), after the frost has sublimated (examples are highlighted with numbered markers).

However, as we have shown, model dunes are highly dependent on this simulation diffusion rate, so it will be crucial to better constrain this value before comparing simulation results to observed mid-latitude and polar martian dunes.

7.3.1. Possible method for estimating the diffusion rate

The location of the break in a dune's lee slope may also relate to competition between saltation and diffusive processes (in addition to reversing winds). Within dunes with a break in lee slope, the upper portion is the slipface, where saltation is active: $Q \sim x^2/T_{\text{salt}}$, where x is the horizontal length of the slipface (the portion of the lee slope at the angle of repose; Figure 7.11). Diffusion operates over the entire lee slope: $D \sim L^2/T_{\text{diff}}$, where L is the horizontal length of lee slope. If the dune lee slope profile is psuedo-steady (i.e, returns to the same value after a wind reversal cycle), this implies that $T_{\text{salt}} \sim T_{\text{diff}}$ and we find that $D/Q \sim (L/x)^2$. This relation provides us with a possible method for estimating the relative diffusion to saltation rate over the dune based on lee slope morphology, by comparing dunes with similar L/x ratios.

Preliminary simulation results indicate that this may be the case. In these simu-

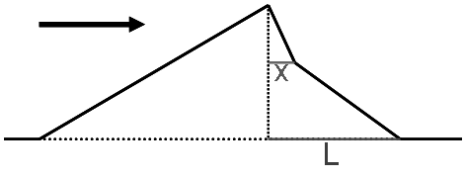

FIGURE 7.11. Schematic diagram showing lee slope lengthscales that may be related to the relative diffusion vs. saltation rate on a dune.

lations, flux is nearly equivalent between dunes of similar aspect ratio (as the shear stress calculation depends on nearby-slope values, as discussed in subsection 3.1.2) and diffusion was a constant. Figure 7.12 shows that the length of the slipface (after the wind blows towards the right, the dominant direction, and the slope adjusts back) varies with dune size and frequency of wind reversals. However, the ratio of lee slope to slipface length (L/x) is very similar between simulation runs.

The spread that appears when the period length increases is due to differences that form between dunes' aspect ratios, as the dunes are able to more completely adjust to the new wind direction; this causes differences in the sand flux over the dunes. This is also the reason that the smallest dune experiencing the 3/1 wind reversal behaves differently – this dune is able to more completely adjust its shape between wind reversals, so it has a different shape at the end of a wind reversal cycle than the other dunes, and does not experience the same flux.

7.4. Results

Our simulation results demonstrate specific and quantitative connections between dune slope morphology and reversing wind directions and cold climate processes (Table 7.1). Although these results are preliminary and indicate the high-level of coupling between processes, careful combinations of measurables can perhaps be used to decouple the effects of these processes in the interpretation of actual dune forms. Additionally, climate, polar process, and sediment cementation studies will aid efforts by independently constraining some model parameters, such as effective diffusion rates.

These results will also aid in future efforts to replicate a specific martian dune shape. If a study successfully replicates the details of a dune form, this implies that the simulation parameters and processes used are related to and (relatively) scaled appropriately to the environmental conditions and formative processes of the observed dune. Although there is no guarantee of this relation, model parameters can provide at least a starting dataset for understanding a dune's environment.

This may prove especially useful in understanding the formation of "extreme" dune shapes, such as flat-topped dune seen in Antartica (Figure 7.13) and on Mars (Figure 7.14). Currently, we have been unsuccessful in numerically replicating this dune

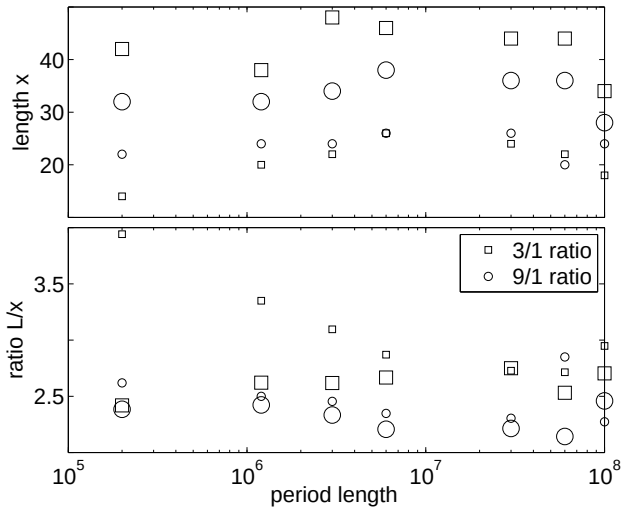

FIGURE 7.12. Simulations show that the length of the slipface (x) varies with dune size and frequency of wind reversals, and appears independent of the wind reversal period length. The ratio of the lee slope to slipface (L/x) appears independent of all of these values as long as the dune aspect ratios remain similar (not the case with very long period lengths or very small dunes), so may be primarily related to the relative rates of diffusion and saltation. (Large markers: dunes 30m high; small: 20m.)

form; it appears that a very carefully selected combination of high diffusion, slope-dependent ice cementation, and reversing winds will be needed. Another interesting and currently unexplained dune form is the elongated and slipface-less Antarctic 'whale-back' dune (Bristow et al. 2009).

7.4.1. Implications for martian dunes

Our simulation results show that polar processes and reversing winds cannot be neglected in modeling studies of martian mid-latitude and polar dunes. Such processes may explain observed morphological differences between mid-latitude intracrater dunes and polar dunes (Bourke, Balme & Zimbelman 2004). Additionally, steeper mean stoss slopes and shallower mean lee slopes have important implications for estimations of dune height (e.g., Bourke et al. 2006) and volume, which relate to estimates of regional and global erosion rates and sediment volume.

Dune Morphology	**Related Process/Parameter**
round/flattened tops	diffusion, wind reversal, influx of sand to sides
symmetry of dune/dual slipfaces	ratio for wind reversal, cementation
slipface length	diffusion vs. saltation, period of wind reversal
mean lee/stoss slopes	ratio for wind reversal, diffusion

TABLE 7.1. Table showing connected dune slope measurables and the simulated process/parameter associated with such features.

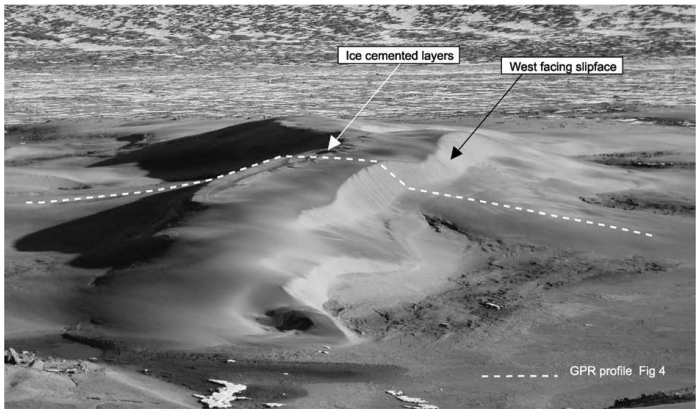

FIGURE 7.13. An Antarctic reversing dune with a flat top, displaying slipface development on both sides. The west facing 'summer' slipface is visible on the right side of the dune. Image taken from Bristow et al. (2010).

FIGURE 7.14. HiRISE image of a flat-topped dune with slipfaces on two sides (PSP_004235_1300; 49S, 34E) in Matara crater dune field. The sinuous gullies on the left of the dune are hypothesized to be formed by melting ground ice (Miyamoto et al. 2004).

8. CONCLUSIONS

The aim of this dissertation work was to investigate the role that various environmental conditions and dynamic processes play in determining dune and dune field morphology. We have approached this through a mixture of model development, analysis, numerical simulation, and comparison with observations. In Chapter 3, we constructed and analyzed the dune evolution model. Chapters 4 through 6 focused on identifying and quantifying the influence that sand flux, dune collisions, and bedrock topography will play in dune size regulation. In Chapter 7, we focused on details of dune slope and morphology, and extended the dune evolution model to include reversing winds and cold climate processes. Detailed conclusions were provided within each chapter; here, only general conclusions are given, along with broad discussion of implications for terrestrial and martian dunes and dune fields. We also briefly discuss possible future extensions of these studies.

8.1. Dune Field Morphology

In section 1.1, we first discussed the fact that many dune fields contain uniformly-sized dunes. Many studies have used this to argue that a dune field evolves into specific patterns and that dunes will tend towards a maximum or equilibrium size, but this argument has yet not been validated or extended into quantitative connections with specific environmental conditions or processes. This dissertation aimed to address this open question.

In Chapter 4, we demonstrated that there is no equilibrium isolated dune size. Instead, dunes will achieve an unstable equilibrium size based on the incoming sediment flux; within a field where dunes interact only through the sand flux, this leads to coalescent behavior.

This result motivated the focus of Chapter 5, which was to investigate the influence that interacting dunes will have on dune size within a field. We first considered the influence that non-flat topography (such as neighboring dunes) will have on shear stress, and thus on sand flux. This also predicted coalescent dynamics, so we focused instead on mass exchange through dune collisions. This study is not the first to construct a dune field model, but it is the first to sequentially and thoroughly explore the components of contemporary dune field models and to identify the crucial elements that are needed to connect model results to an observed dune field. We identified specific criteria for a patterned dune field to form, and quantitatively connected the dune field's end-state (patterned: Figure 1.2 or runaway growth: Figure 1.3; subsection 5.3.4) with its collision dynamics and influx size population.

Although we showed it is possible for a dune field to become patterned, it was unclear how likely it is that so many dune fields just naturally have the correct cou-

pling between the dune interaction processes and the dune nucleation size population. In Chapter 6, we completed preliminary numerical experiments to explore the effect non-flat bedrock topography would have on isolated dune evolution, and extended this to binary dune collisions. We had hoped that topography would exert a stabilizing influence and would create more similarly-sized dunes, but it in fact did the opposite (at least in two dimensions). Both Gaussian hills and upward/downward steps enhanced interaction between colliding dunes, resulting in a higher sand transfer from the smaller to the larger dune. This increased the probability for coalescence and overall pushed a dune field towards runaway dynamics.

In summary, we have primarily *negative* results with respect to dune size regulation through isolated dune evolution via sand flux and migration over topography. This strongly implies that studies focused on the evolution of one or a few dunes will not be sufficient for identifying the reason that dunes within a field often tend towards a uniform size. In other words, a dune evolution model cannot simply be scaled up for studies of dune field evolution.

Instead, studies need to be multi-scale and to focus on interactions that occur within the field between neighboring dunes and between dunes and (possibly non-constant) environmental conditions. For example, in Chapter 5 we showed that dune collision dynamics can result in the dune field evolving into uniformly-sized dunes, given a proper coupling between the influx dune size population and the interaction rule. Further and more detailed investigation is needed here to explore the premise that most dune fields naturally have the right conditions for pattern formation.

There are other possible processes that may enhance dune field stabilization through size-dependent effects (and preferential break-up or stabilization of large dunes). Some of these will be discussed in Section 8.3.

8.2. Dune Morphology

Although isolated dune modeling studies may not be sufficient for understanding dune field evolution, the dune evolution model has been shown to be useful in analysis of detailed dune morphology. Past studies using a continuum dune evolution model have been used to quantitatively connect observed martian and terrestrial dune shapes with environmental conditions throughout dune evolution.

However, the contemporary dune evolution model is limited as it relies on several simplifying assumptions about constancy in the environment (such as steady winds and flat bedrock topography) and dynamics. In this dissertation, we have attempted to extend the model to accomodate more complicated environments.

In Chapter 6, we showed that non-flat bedrock topography (such as a Gaussian hill or step) will temporarily alter a dune's shape and migration rate. Although the dunes did adjust back to their original shapes and migration velocity (unless the topography and dune were of comparable height), these changes need to be considered when

making comparisons between simulation results and observed dunes evolving over non-flat terrain (e.g., in a crater). Alternatively, an understanding of the influence that topography has on dune evolution can perhaps be used to reverse-engineer topography estimates based on observed dune shapes.

The dune evolution model was also extended to include reversing winds and polar processes, as presented in Chapter 7. Although this results of this study are ill-constrained due to a lack of comparative observations, our simulation results show specific and quantitative connections between dune slope morphology and reversing wind directions and polar processes that could be used in the interpretation of observed polar dune fields on the Earth and Mars. Our results are very preliminary, but they do provide a framework for future studies aimed at quantifying the influence polar processes and reversing winds exert on terrestrial and martian dune evolution.

That study also highlights the importance of properly scaling all model parameters in a consistent manner to accurately portray the effect of interacting processes (such as gravity-driven avalanches, general diffusion processes, and wind-driven saltation). This last point will be discussed further in subsection 8.3.3.

8.3. Future Extensions

Here we propose several research extensions that should be included in the construction of future dune and dune field evolution model studies. Existing observations and qualitative models imply that these processes exert measurable effects on dune and dune field morphology, and thus should be considered when interpreting observed dune forms.

8.3.1. Dune nucleation

In subsection 5.4.1, we showed that two model parameters completely predicted whether or not a dune field would become patterned after a large number of dune collisions (Figure 5.12): (i) an interaction parameter describing when collisions will redistribute sand from the larger to the smaller dune (the crossover value, r_*), thus decreasing dune size polydispersity, and (ii) the the standard deviation/mean ratio of the influx dunes' size distribution, which corresponds to the polydispersity of the dune sizes found at the beginning of the field, when dunes first form and have not yet interacted with each other. Previous studies have calculated dune size and spacing distributions within mature terrestrial (Wilkins & Ford 2007) and martian (Bishop 2007) dune fields and proved that dunes undergo some form of organization to create non-random distributions. These studies, however, did not explain the origin of the organization, which could depend on processes and environmental conditions during dune formation and/or subsequent interaction.

A method for quantifying the size distribution created through dune nucleation within observed fields would provide constrained estimates for the influx population

used in a dune field model. This will allow modeled dune fields to more closely resemble specific, observed dune fields and increase the prediction ability of our dune field model. Additionally, by isolating the effect of formation processes and conditions on dune field morphology, this study will provide much-needed validation and calibration information for dune initiation models.

8.3.2. Evolving intrafield sediment conditions

Currently, the dune evolution model considers only the mean grain size within the dune, and even this is indirectly included within a flow parameter that directly relates to the minimum dune size (Andreotti et al. 2002*b*) and dune destabilization (Elbelrhiti et al. 2005): the sand flux saturation length (a spatial delay in the sand flux's response to the local wind regime). As this flow parameter is generally held constant in dune evolution model studies, it is implicitly assumed that the mean grain size does not greatly change throughout a simulation.

Field studies have shown that dunes may nucleate with a strongly peaked and spatially-uniform grain distribution, but spatial variations in mean grain size and grain size distribution naturally evolve (Figure 2.3) as a function of wind regime, dune age/type, and underlying sediment composition (Wang et al. 2003, Besler 2005). As briefly mentioned in subsection 5.4.4, increasing observational evidence implies that these variations can strongly influence dune and dune field dynamics. For example, Besler (2002) examined apparent collision dynamics within on-going dune collisions in the Libyan desert, and compared this with the dunes' granulometrics. Based on these observations, she hypothesized that dunes made of softer and finer grains were more likely to coalesce, while interacting dunes made of more compacted and coarser grains was more likely to have a collision result in separate, similarly-sized dunes (enhancing stability of a patterned dune field). Due to winnowing effect, older/larger dunes are more likely to contain more compacted, coarser grains (Besler 2005), meaning that dune collision dynamics are not constant, and should enhance pattern formation as a dune field ages. Additionally, as surface grains increase in mean size, sediment transport rates should slow and older dunes should be stabilized.

This stabilization of more mature dune fields due to granule surface shielding, along with the overall generally larger size of older dunes, can perhaps explain why dune field reorganization seems to occur over much slower timescales than dune construction, leading to multiple dune patterns superimposed within a dune field (Kocurek & Ewing 2005).

8.3.3. Process interactions

As discussed in Chapter 7, when multiple processes are relevant in dune evolution, it is important to estimate (or at least constrain) the relative timing and parameter magnitudes related to the different processes. This is especially important if the processes are interacting to create the dune form; for example, it is competition

between diffusive processes and wind-driven saltation that create the stoss/lee dune slopes and the asymmetry in the dune cross-sectional profile (Figure 2.1, 2.2; Section 2.2). Estimates of these relative process rates can sometimes be found through independent studies, thus allowing for predictions of dune evolution and morphology. Conversely, the relative rates can sometimes be estimated from observations and scaling arguments (e.g., subsections 3.1.5, 7.3.1).

It is also important to investigate how discrete processes will interact with continuous or averaged processes. For example, in Chapter 7 we showed that discrete reversals of wind direction influence some dune measurables (such as an instantaneous measure of the dune slope), while the time-averaged process (which can be approximated as a continuous process) influenced other measurables (such as the average dune stoss slope; Figure 7.7).

This is also important when a process occurs over much longer timescales (such as ice-cementation of sediment in polar regions) than changes in mobile-sediment supply and or wind conditions. As pointed out in Chapter 7, studies using discrete intervals of saltation (rather than a temporally-scaled continuous-saltation simulation) may be especially important in martian dune studies, as saltation is thought to occur only rarely (Parteli & Herrmann 2007) and may interact with slower, but more continuous, cold climate processes.

Finally, it has also been proposed that seasonal storms play an important role in regulating dunes' sizes by inducing long-wavelength perturbations on large dunes, which cause them to break into several dunes (Elbelrhiti et al. 2005). Given the observational support for this theory, it would be very useful to include this stochastic process in the dune field model. However, this will first require a quantification of storm occurrence rates, and exploration of how important the discrete events will be, versus considering only the long-time-averaged influence.

8.4. The Need for Comparative Observations

As discussed in Chapter 1, increased collaboration between dune geologists, physical modelers, and mathematicians has greatly aided efforts to quantitatively connect dune and dune field evolution with environmental conditions and physical processes. For example, the increased availability of spacecraft images of dune fields on different planetary surfaces in the last decade has helped with the validation of assumptions and parameters used in the basic dune evolution model. Currently, however, the main constraint on further dune and dune field evolution model development remains a lack of field or laboratory observations. In particular, there are very few studies which focus on dune interactions and nucleation, which greatly limits model predictive ability.

Studies such as those presented in this dissertation can, however, serve as as guides for future observational studies. Scaling relations and behavior trends derived through model equation analysis and numerical experimentation provide information

about possible connections between dune measurables and influential environmental conditions or physical processes. For example, this dissertation highlights the need for these field and laboratory studies:

- Changes in localized saltation rates as dunes collide with a neighboring dune (Section 5.2) or with bedrock topography (Section 6.2);
- Measurements of relative saltation and diffusion rates, and resultant dune stoss and lee slopes (Section 7.3);
- Dune size distribution found at the beginning of the dune field and created through nucleation processes (subsection 8.3.1).

Future interative comparisons between mathematical models of dune and dune field evolution and field and laboratory observations will continue to elucidate, in greater and greater detail, the quantitative connections between environmental conditions and dune morphology/behavior. As dunes are prime examples of geomorphic markers of environmental conditions over many scales, these studies provide important contributions towards the advancement of scientific knowledge and understanding of surface and climate evolution on the Earth and other planets.

A. THE NUMERICAL ALGORITHM

As outlined in subsection 3.1.8, the simulation evolves the non-dimensional dune profile h over a time step dt, via several relations. Within our model, all relations have been linearized to simplify analysis.

Within each time step, we start with the dune profile (h^n). The following steps are then followed to yield the dune profile at the next time step (h^{n+1}), and the process is iterated.

A.1. Avalanching

Avalanching is applied to smooth the surface and to keep slopes below the angle of repose. This process is assumed to be diffusive in nature, as described in subsection 3.1.5. The diffusion coefficient at a mid-gridpoint ($x_{i-1/2}$, which is between x_i and x_{i-1}; $i \in [1, 2, \ldots, N]$) is calculated via backward differences:

$$\begin{aligned} D(x_{i-1/2}) &= \mathrm{D}_h \underbrace{\frac{1 + \mathrm{D}_a \exp\left((|(h_i - h_{i-1})/dx| - \tan(\text{ref. angle}))/\gamma\right)}{1 + \exp\left((|(h_i - h_{i-1})/dx| - \tan(\text{ref. angle}))/\gamma\right)}}_{\text{slope check}} \times \\ &\quad \underbrace{\left(\frac{1}{2}\tanh(G_1(h_i - \mathrm{gr}_i - G_2\epsilon)) + 1/2\right)}_{\text{ground check}} \end{aligned} \tag{A.1}$$

The leading coefficient (D_h) is the low-level diffusion that smooths the surface due to wind variability, etc. The 'slope check' term (Figure A.1) determines if avalanching should occur; if so, then the diffusion coefficient is increased by the multiplicative factor D_a (generally 10^2 or 10^3). The 'ground check' term (Figure A.2) determines how much sand is available for avalanching; no avalanching occurs when within $G_2\epsilon$ (the limit ϵ is defined in subsection 2.2.3) of the the non-erodible surface (gr), which was generally defined as $h = 0$ (sometimes more complicated topographies were used, as described in Chapter 6). When periodic boundary conditions were used, then $h_0 = h_n$; when semi-infinite boundary conditions were used, then $D(x_{1/2}) = 0$ to fix the end-gridpoint.

An implicit central differences scheme was then applied to calculate diffusion, with a forward difference in time:

$$\begin{aligned} h_t &= (D(h_x)h_x)_x \\ \frac{h_i^{n+1} - h_i^n}{dt} &= \frac{D_{i+1/2}h_{i+1} - (D_{i+1/2} + D_{i-1/2})h_i + D_{i-1/2}h_{i-1}}{dx^2} \end{aligned} \tag{A.2}$$

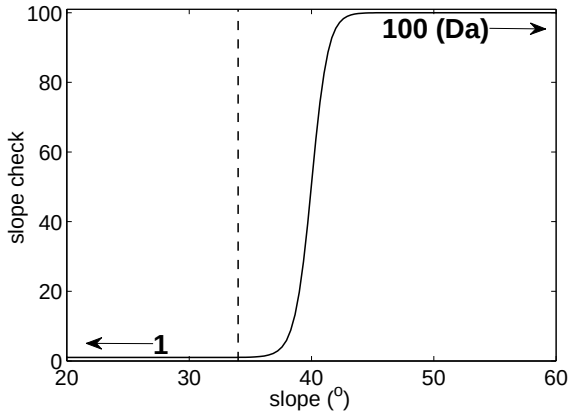

FIGURE A.1. Function used to determine diffusion coefficient, based on local slope. When the slope is below the angle of repose (vertical dashed line), then this function $\rightarrow 1$. When the slope is at or above the angle of repose, then this function $\rightarrow D_a$. The exact shape of this function is determined by the ref. angle (which determines when it increases; generally ref. angle $= 40^o$) and γ (which determines its steepness; $\gamma = 0.02$).

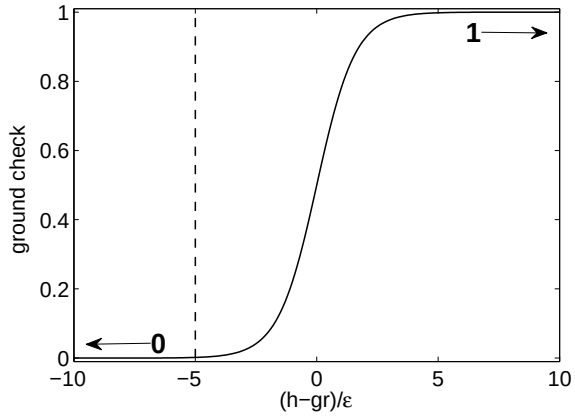

FIGURE A.2. Function used to determine diffusion coefficient, based on availability of mobile sand. When the sand depth is less than $G_2\epsilon$, then avalanching does not occur. The exact shape of this function is determined by the G_1 (which determines the steepness; here $G_1 = 200$) and G_2 (which determines at what depth the sand should not avalanche; $G_2 = 5$).

A.2. Separation bubble

We then calculate the separation bubble (s) which describes the airflow over the surface. This is done by locating all brink locations, and then extending the upper-right portion of an ellipse (of $\beta = 6.5$ aspect ratio, as defined in subsection 3.1.1) from each brink, with continuous value and slope at the connection point. The airflow profile for the entire simulation box is then found by taking the maximum of the juxtaposition of these partial-ellipse-profiles and the dune topography. The full profile is C^1 except where a separation bubble rejoins downwind topography (where it is C^0).

A.3. Shear stress

The shear stress perturbation ($\tilde{\tau}$) is calculated from the separation bubble (s) via fourier methods (Matlab FFT) applied to the Jackson-Hunt equation (Jackson & Hunt 1975, Weng et al. 1991):

$$\widehat{\tilde{\tau}} \;=\; (A \cdot K + B \cdot D) \cdot \hat{s} \tag{A.3}$$

where K is the the convolution of $1/\pi x$ (the Hilbert transform) and the spatial-derivative in fourier space ($|k|$), and D is the spatial-derivative in fourier space (ik). The parameters A and B determine the importance of the local versus global slope, and depend logarithmically on the ratio of geometric lengthscale (conventionally, the dune half-length; $L = \pi/2k$) to the surface roughness ($\sim \frac{1}{10}$ grain diameter; z_0). For a dune, the geometric lengthscale is typically 6-9 orders of magnitude longer than the surface roughness, so $A \sim 4$ and $B \sim 1$. These parameters can be calculated more exactly via the following equations (explained in more detail in Jackson & Hunt 1975, Weng et al. 1991, Kroy et al. 2002):

$$\begin{aligned}
\Phi &\equiv L/z_0 \\
\phi &\equiv 2\kappa^2\Phi/\ln\phi \text{ (note implicit formula)} && \text{(A.4)} \\
A &= \frac{\ln(\Phi^2/\ln(\Phi))^2}{2\ln(\phi)^3}\big(1 + \ln(\phi) + 2\ln(\pi/2L) + 4\gamma_E\big) && \text{(A.5)} \\
B &= \pi\frac{\ln(\Phi^2/\ln(\Phi))^2}{2\ln(\phi)^3} && \text{(A.6)}
\end{aligned}$$

where κ is the von Kármán constant (≈ 0.4) and γ_E is Euler's constant (≈ 0.577)

A.3.1. Jackson-Hunt equation

In this subsection, we briefly describe the derivation of the Jackson-Hunt equation (which is explained in full detail in Jackson & Hunt 1975, Weng et al. 1991). We focus on this equation as its inclusion is perhaps the weakest assumption within our dune

evolution model. The use of this "shallow hill" approximation has been empirically validated (Sauermann et al. 2003) for flow over an isolated dune on a flat surface, but it may (is probably) not be a valid approximation over more complicated terrain and dune morphologies. However, at this time no better approximation is known.

The study by Jackson & Hunt (1975) considers windflow over a two-dimensional low, symmetric hill (Figure A.3; $H \ll L$ and slope everywhere on the order of H/L, the study used $h(x/L) = H/(1+(x/L)^2)$) with constant surface roughness (z_0; assume $L/z_0 \to \infty$; note that $L/z_0 = \Phi$ as in Eqn. A.4) and far-field shear stress velocity (u_*). Far above and upwind/downwind from the hill (i.e., as y/L or $|x/L| \to \infty$), the airflow will follow the Prandtl-von Kármán model (Eqn. 2.1):

$$u_0(y) = \begin{cases} u_*/\kappa \ln(y/z_0) & y < \delta \\ u_*/\kappa \ln(\delta/z_0) & y \geq \delta \text{ (free stream velocity).} \end{cases} \tag{A.7}$$

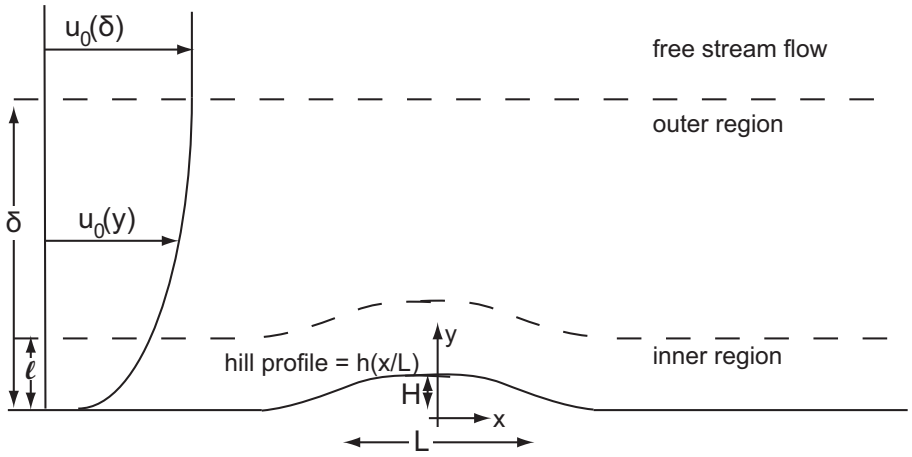

FIGURE A.3. Schematic diagram showing airflow regimes over a low hill. Image is from Jackson & Hunt (1975).

Over the hill, the study considers flow within two layers. Within the inner layer (of depth ℓ; note that $\ell/z_0 = \phi$ from Eqn. A.4), the horizontal velocity (u) is given to the first approximation by the upstream velocity at the same displacement above level ground ($\Delta y = y - h(x/L)$; y is the height over the far-field flat plane). However, continuity implies the existence of a vertical velocity (due to airflow compression from the hill: $v = h_x u_0(\Delta y)$) which causes a perturbative pressure (p) on the outer region, and thus a change in horizontal velocity within the outer region ($u(x, y) = u_0(y) + \tilde{u}(x, y)$). Continuity of pressure between the regions then implies that there is also a horizontal perturbation velocity within the inner region (i.e, within the inner boundary, the wind velocity at a local height over the hill is that given by the Prandtl-von Kármán model plus a perturbation: $u_i(x, \Delta y) = u_0(\Delta y) + \tilde{u}_i(x, \Delta y)$.

These perturbations ($\tilde{u}$ and v) are first calculated within the outer region. They are further constrained (and $\tilde{u}_i$ is calculated) by matching velocity and pressure terms at the boundary between the inner and outer layers.

Solving for the flow within the outer region involves consideration of the vertical displacement of the flow due to presence of the hill (in the inner region). The outer flow's upper and far-field boundary conditions are set by the far-field conditions, as far from the hill (i.e., as y/L or $|x/L| \to \infty$) the displacement and thus the vertical velocity u should tend to zero. This suggests that the vertical scale of the outer region (δ) must be of the same order as the horizontal scale of the inner region, which is the length of the hill L.

The perturbation terms within this layer ($\tilde{u}$, v, and p) can be expressed in asymptotic power series for the limit $\ln \Phi \to \infty$:

$$\text{i.e., } \tilde{u} \sim u_* \frac{\ln \phi}{\ln \Phi}(U^{(0)} + \frac{1}{\ln \Phi} U^{(1)} + \dots) \tag{A.8}$$

Normalizing $\tilde{u}$ so that the linear inertial terms are of the same order as the pressure gradient terms, then substituting into the momentum equation (up to $O(1/\ln \Phi)$) yields, for $y < \delta$:

$$\begin{aligned}
\frac{\partial U^{(0)}}{\partial (x/L)} + \frac{\partial P^{(0)}}{\partial (x/L)} &= 0 && \text{(A.9)}\\
\frac{\partial V^{(0)}}{\partial (x/L)} + \frac{\partial P^{(0)}}{\partial (x/L)} &= 0 && \text{(A.10)}\\
\frac{\partial U^{(1)}}{\partial (x/L)} + \frac{\partial P^{(1)}}{\partial (x/L)} &= -\Big(\ln(y/L) \frac{\partial U^{(0)}}{\partial (x/L)} + \frac{\partial V^{(0)}}{\partial (x/L)} \Big) && \text{(A.11)}\\
\frac{\partial V^{(1)}}{\partial (x/L)} + \frac{\partial P^{(1)}}{\partial (x/L)} &= -\ln(y/L) \frac{\partial V^{(0)}}{\partial (x/L)} && \text{(A.12)}\\
& && \text{(A.13)}
\end{aligned}$$

This yields:

$$\begin{aligned}
\nabla^2 V^{(0)} &= 0 && \text{(A.14)}\\
\nabla^2 V^{(1)} &= V^{(0)}/(y/L)^2 && \text{(A.15)}
\end{aligned}$$

where $\nabla^2 = \frac{\partial^2}{\partial (x/L)^2} + \frac{\partial^2}{\partial (y/L)^2}$.

For $y > \delta$, as $du_0/dy = 0$ the equations lead to:

$$\begin{aligned}
\nabla^2 V^{(0)} &= 0 && \text{(A.16)}\\
\nabla^2 V^{(1)} &= 0
\end{aligned}$$

To justify the neglect of higher order terms, the following scale constraints are needed: $\ln \Phi \gg \ln(\delta/L)$ and $\ln(\delta/L) = O(1)$. As long as these conditions are satisfied,

then the asymptotic expansion (Eqn. A.8) will be valid within the outer region for both $y < \delta$ and $y > \delta$.

At the boundary between the inner region and the outer region (i.e., as $y/L \to 0$ in the outer region and $\Delta y/\ell \to \infty$ in the inner region), the perturbative pressure (p) and horizontal and vertical velocities ($\tilde{u}_i$, v) must match. Solving Eqn. A.12 and A.16 in Fourier space (w.r.t. the x-coordinate) with all boundary conditions yields:

$$P^{(0)}(x) = -\frac{L}{\pi H}\int_{-\infty}^{\infty}\frac{h_x(s)}{(x/L - s)}ds \tag{A.17}$$

on the surface $y/L \to 0$. The lower boundary of the inner region ($\delta y = z_0$) must satisfy the no-slip condition (i.e., $u = v = 0$). The thickness of the inner region (ℓ) is found by considering the necessary balance between the acceleration and the stress gradient when $\Delta y/\ell \sim O(1)$.

As was done for the outer region, the velocities and pressure can be expanded asymptotically within a power series for the limit $\ln(\phi) \to \infty$:

$$\text{i.e., } \tilde{u}_i \sim U_i^{(0)} + \frac{1}{\ln\phi}U_i^{(1)} + \dots \tag{A.18}$$

which yields:

$$\frac{\partial U_i^{(0)}}{\partial(x/L)} + \frac{\partial P_i^{(0)}}{\partial(x/L)} = \frac{\partial}{\partial(\Delta y/\ell)}\Big(\frac{\Delta y}{\ell}\frac{\partial U_i^{(0)}}{\partial(\Delta y/\ell)}\Big) \tag{A.19}$$

$$\frac{\partial U_i^{(1)}}{\partial(x/L)} + \frac{\partial P_i^{(1)}}{\partial(x/L)} - \frac{\partial}{\partial(\Delta y/\ell)}\Big(\frac{\Delta y}{\ell}\frac{\partial U_i^{(1)}}{\partial(\Delta y/\ell)}\Big) = \tag{A.20}$$

$$-\ln(y/\ell)\frac{\partial U_i^{(0)}}{\partial(x/L)} - \frac{V_i^{(0)}}{y/\ell} + 2a_1\kappa^2\frac{\partial}{\partial(\Delta x/L)}\Big(\frac{\Delta y}{\ell}\frac{\partial U_i^{(0)}}{\partial(\Delta y/\ell)}\Big)$$

$$\frac{\partial P_i^{(0)}}{\partial(\Delta y/\ell)} = 0 \tag{A.21}$$

$$\frac{\partial P_i^{(1)}}{\partial(\Delta y/\ell)} = 2a_2\kappa^2\frac{\partial}{\partial(\Delta y/L)}\Big(\frac{\Delta y}{\ell}\frac{\partial U_i^{(0)}}{\partial(\Delta y/\ell)}\Big) \tag{A.22}$$

Solving these equations yields:

$$u \sim u_*\Big(\ln(y/z_0) - \frac{h}{y} - \frac{H}{L}\ln(\Phi)P^{(0)} + \dots\Big) \tag{A.23}$$

which, as expected, is the asymptotic solution at both the lower bound of the outer region ($y/L \to 0$) and the upper bound of the inner region ($\Delta y/\ell \to \infty$). The first term in Eqn. A.23 is $u_0(y)$ (Eqn. A.7), so the remainder is the perturbative horizontal velocity ($\tilde{u}$: Figure A.4).

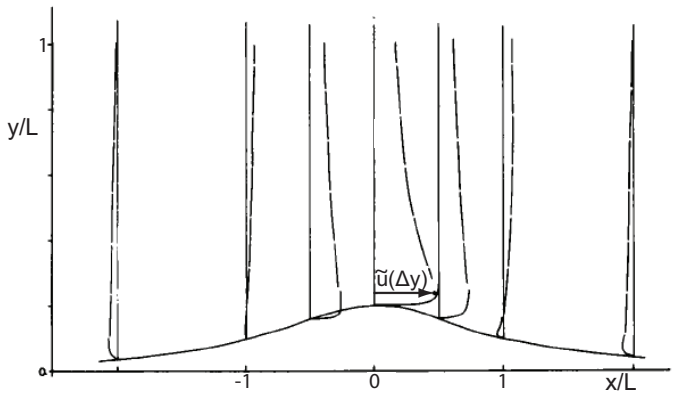

FIGURE A.4. Normalized perturbative velocities ($\tilde{u}(x, \Delta y)$) at different positions at the surface of a low hill. Image is from Jackson & Hunt (1975).

Once the perturbative horizontal velocity is calculated, it can be rewritten as a perturbation to the shear stress ($\tau = (u_*)^2 \rho_{\text{air}}$):

$$\tilde{\tau} \sim \frac{2\kappa \Delta y}{u_*} \frac{\partial \tilde{u}}{\partial y} \tag{A.24}$$

A.4. Sand flux

As we are working in the non-dimensional space (i.e., have normalized by the far-field sand flux $C\tau_0^{3/2}$), the saturated sand flux $q_s = 1 + 3/2\tilde{\tau}$.

The actual sand flux is found via backward differences:

$$\begin{aligned} q_x &= q_s - q \\ q(x_i) - q(x_{i-1})/dx &= \begin{cases} q_s(x_i) - q(x_i) & h_i - \text{gr}_i > \epsilon \text{ and } h = s \\ 0 & h_i - \text{gr}_i < \epsilon \text{ and } h = s \\ -q(x_i) & h < s \end{cases} \end{aligned} \tag{A.25}$$

Within the second case, sand is neither deposited nor eroded as bedrock is exposed. Within the third case ($s > h$ only inside the shadow zone/separation bubble), $q_s \equiv 0$ so only deposition occurs. These two cases preserve the nonnegativity of h, as $q_x \leq 0$ (only deposition can occur) as long as h is small.

When periodic boundary conditions are used, q is calculated via matrix inversion. When a semi-infinite boundary conditions are used, then q is calculated from a fixed $q_1 = q_{\text{in}}$.

A.5. Update the dune profile

Changes in dune profile are then found via the Exner equation, discretized via upwinding (backward differencing, as sand blows in one direction):

$$\begin{aligned} h_t &= -q_x \\ (h_i^{n+1} - h_i^n)/dt &= -(q_i - q_{i-1})/dx \end{aligned} \tag{A.26}$$

B. TWO-DUNE REDUCED DIMENSION MODEL

This model was constructed to investigate the dynamics of a collision between two dunes within a reduced complexity frame. The aim was to isolate important behaviors without consideration of detailed dune morphology. Unfortunately, although this model can be used to simulate binary dune collisions, we were unable to decouple the evolution of the six model variables, so the reduced dimension system was not actually easier to simulate or analyze.

B.1. Two-dune Structure

We specify the total cross-sectional area (A) of the two dunes, and assume that it is conserved throughout the collision. The lee slopes are fixed at the slope of repose ($\alpha = \tan(34^o)$), and the dunes are initiated in contact with each other. The two-dune profile (h; Figure B.1) is now specified by five variables: the windward slopes of the dunes ($\sigma_{\mathrm{u,d}}$, where 'u' denotes upwind and 'd' denotes downwind), the heights of the dunes' crests ($H_{\mathrm{u,d}}$), and the distance between the foot of the structure and an arbitrary location (m). The distance between the dunes' crests (d) is fixed since we specified A, and is equal to:

$$d = \frac{H_2}{\sigma_d} + \frac{H_u}{\alpha} - \sqrt{\frac{2A_o}{1/\alpha + 1/\sigma_d}}\Big(\frac{1}{\alpha} + \frac{1}{\sigma_d}\Big)$$

where A_o is the "overlap" volume:

$$A_o = \frac{H_u^2}{2}\Big(\frac{1}{\sigma_u} + \frac{1}{\alpha}\Big) + \frac{H_d^2}{2}\Big(\frac{1}{\sigma_d} + \frac{1}{\alpha}\Big) - A.$$

Note that d is positive (and physically meaningful) only if $A_0 \in [0, A]$. Additionally, if $A_0 = 0$ (i.e., the two interacting dunes are disjoint), then d is not uniquely defined ($d \geq \frac{H_d}{\sigma_d} + \frac{H_u}{\alpha}$); to uniquely define d, we restrict the dunes to be just touching ($d = \frac{H_d}{\sigma_d} + \frac{H_u}{\alpha}$) .

We define the dune profile ($h(x,t)$; Figure B.1), which is piece-wise linear and

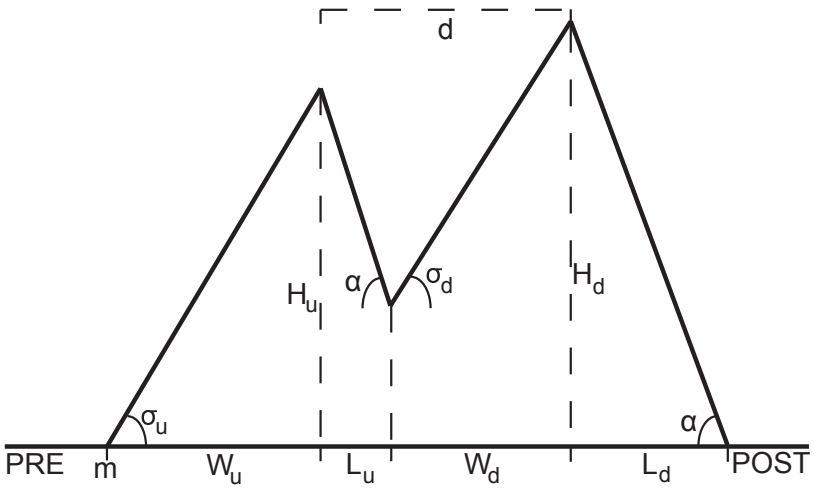

FIGURE B.1. Schematic diagram of the reduced dimension two-dune structure.

continuous with six regions:

$$h = \begin{cases} 0 & x \in PRE = (-\infty, m), \text{ pre-dune} \\ (x-m)\sigma_u & x \in W_{\mathrm{u}} = (m, m + \frac{H_u}{\sigma_u}), \\ & \quad \text{upwind dune's stoss slope} \\ -(x - m - \frac{H_u}{\sigma_u})\alpha & x \in L_{\mathrm{u}} = (m + \frac{H_u}{\sigma_u}, m + \frac{H_u}{\sigma_u} + \frac{H_u - H_d + d\sigma_d}{\sigma_d + \alpha}), \\ \quad +H_u & \quad \text{upwind dune's lee slope} \\ (x - m - \frac{H_u}{\sigma_u} - d)\sigma_d & x \in W_{\mathrm{d}} = (m + \frac{H_u}{\sigma_u} + \frac{H_u - H_d + d\sigma_d}{\sigma_d + \alpha}, m + \frac{H_u}{\sigma_u} + d), \\ \quad +H_d & \quad \text{downwind dune's stoss slope} \\ -(x - m - H_u/\sigma_u - d)\alpha & x \in L_{\mathrm{d}} = (m + \frac{H_u}{\sigma_u} + d, m + \frac{H_u}{\sigma_u} + d + \frac{H_d}{\alpha}), \\ \quad +H_d & \quad \text{downwind dune's lee slope} \\ 0 & x \in POST = (m + \frac{H_u}{\sigma_u} + d + \frac{H_d}{\alpha}, \infty), \\ & \quad \text{post-dune} \end{cases} \tag{B.1}$$

B.2. Derivatives of the Two-dune Profile

Derivatives of this function with respect to the variables are as follows:

$$\frac{\partial h}{\partial \sigma_u} = \begin{cases} 0 & x \in PRE \\ (x-m) & x \in W_u \\ -\frac{H_u \alpha}{\sigma_u^2} & x \in L_u \\ \frac{H_u \sigma_d}{\sigma_u^2}\left(1 - H_u/2\sqrt{\frac{2A_o}{1/\sigma_d+1/\alpha}}\right) & x \in W_d \\ -\frac{H_u \alpha}{\sigma_u^2}\left(1 - H_u/2\sqrt{\frac{2A_o}{1/\sigma_d+1/\alpha}}\right) & x \in L_d \\ 0 & x \in POST \end{cases} \tag{B.2}$$

$$\frac{\partial h}{\partial \sigma_d} = \begin{cases} 0 & x \in PRE \\ 0 & x \in W_u \\ 0 & x \in L_u \\ x - m - H_u/\sigma_u - d & \\ \quad -\frac{1}{2\sigma_d^2}\left(H_d^2/\sqrt{\frac{2A_o}{1/\sigma_d+1/\alpha}} + -\sqrt{\frac{2A_o}{1/\sigma_d+1/\alpha}} + 2H_d\right) & x \in W_d \\ -\frac{\alpha}{2\sigma_d^2}\left(H_d^2/\sqrt{\frac{2A_o}{1/\sigma_d+1/\alpha}} - \sqrt{\frac{2A_o}{1/\sigma_d+1/\alpha}} + 2H_d\right) & x \in L_d \\ 0 & x \in POST \end{cases} \tag{B.3}$$

$$\frac{\partial h}{\partial H_u} = \begin{cases} 0 & x \in PRE \\ 0 & x \in W_u \\ \frac{\alpha}{\sigma_u} + 1 & x \in L_u \\ -\sigma_d\left(\frac{1}{\sigma_u} + \frac{1}{\alpha} - H_u(1/\sigma_u + 1/\alpha)/\sqrt{\frac{2A_o}{1/\sigma_d+1/\alpha}}\right) & x \in W_d \\ \alpha\left(\frac{1}{\sigma_u} + \frac{1}{\alpha} - H_u(1/\sigma_u + 1/\alpha)/\sqrt{\frac{2A_o}{1/\sigma_d+1/\alpha}}\right) & x \in L_d \\ 0 & x \in POST \end{cases} \tag{B.4}$$

$$\frac{\partial h}{\partial H_d} = \begin{cases} 0 & x \in PRE \\ 0 & x \in W_u \\ 0 & x \in L_u \\ H_d(1 + \sigma_d/\alpha)/\sqrt{\frac{2A_o}{1/\sigma_d+1/\alpha}} & x \in W_d \\ -H_d(1 + \alpha/\sigma_d)/\sqrt{\frac{2A_o}{1/\sigma_d+1/\alpha}} + \alpha/\sigma_d + 1 & x \in L_d \\ 0 & x \in POST \end{cases} \tag{B.5}$$

$$\frac{\partial h}{\partial m} = \begin{cases} 0 & x \in PRE \\ -\sigma_u & x \in W_u \\ \alpha & x \in L_u \\ -\sigma_d & x \in W_d \\ \alpha & x \in L_d \\ 0 & x \in POST \end{cases} \tag{B.6}$$

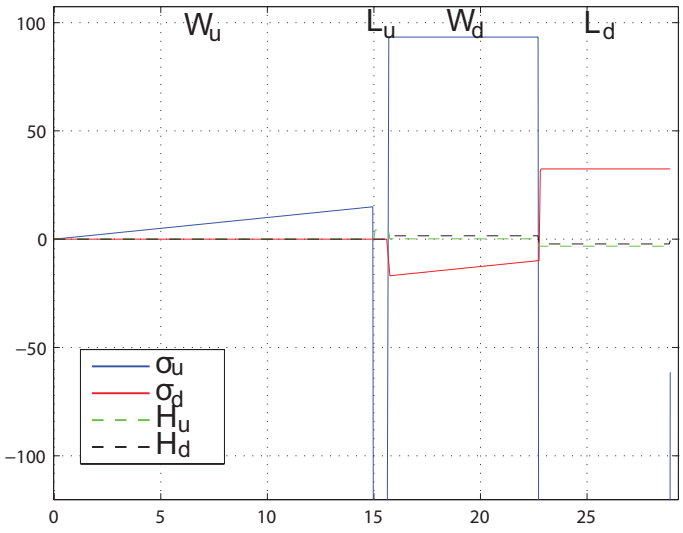

FIGURE B.2. Plot of numerically computed partial derivatives of the dune profile (h), with respect to $H_u,\ H_d,\ \sigma_u$, and σ_d in regions W_u, L_u, W_d, and L_d.

Assuming that h can be expressed purely as a function of the five variables ($\sigma_u,\ \sigma_d,\ H_u,\ H_d,\ m$), we have:

$$\frac{dh}{dt} = \frac{\partial h}{\partial \sigma_u}\dot{\sigma}_u + \frac{\partial h}{\partial \sigma_d}\dot{\sigma}_d + \frac{\partial h}{\partial H_u}\dot{H}_u + \frac{\partial h}{\partial H_d}\dot{H}_d + \frac{\partial h}{\partial m}\dot{m}, \tag{B.7}$$

where $\dot{()} \equiv \frac{\partial h}{\partial t}$. Projecting this function onto a space spanned by the partial derivatives of h yields the time-derivatives of the different variables.

B.3. Isolating Time-derivatives

We identify a set of functions that spans the same space as the partial derivatives Figure B.2, as follows:

- Test function one (T1) is a linear function on the windward slope of the first dune, and isolates $\dot{\sigma}_u$:

$$y = \begin{cases} x - m - \frac{H_u}{2\sigma_u} & x \in W_u \\ 0 & \text{otherwise} \end{cases}$$

- Test function two (T2) is a linear function on the windward slope of the second dune, and isolates $\dot{\sigma}_d$:

$$y = \begin{cases} x - m - \frac{H_u}{\sigma_u} - \frac{H_d - H_u + \alpha d}{2(\sigma_d + \alpha)} & x \in W_d \\ 0 & \text{otherwise} \end{cases}$$

- Test function three (T3) is a constant function over the windward slope of the first dune, and it isolates $\dot{m}$:

$$y = \begin{cases} 1 & x \in W_u \\ 0 & \text{otherwise} \end{cases}$$

- Test function four (T4) is a constant function on the leeward slope of the first dune, and isolates (after subtracting off known parts from the above derivatines) $\dot{H}_u$:

$$y = \begin{cases} 1 & x \in L_u \\ 0 & \text{otherwise} \end{cases}$$

- Test function five (T5) is a constant function on the leeward slope of the second dune, and isolates (after subtracting off known parts from the above derivatines) $\dot{H}_d$:

$$y = \begin{cases} 1 & x \in L_d \\ 0 & \text{otherwise} \end{cases}$$

We now can use the inner product:

$$\langle f, g \rangle = \int_{-\infty}^{\infty} f(x) g(x) dx$$

to project the RHS of the conservation equation ($h_t = -q_x$) onto the space spanned by the test functions.

Test function one gives us:

$$\begin{aligned}
\langle T1, -q_x \rangle &= \langle T1, \frac{\partial h}{\partial \sigma_u} \dot{\sigma}_u \rangle \\
&= \int_{Wu} \Big(x - m - \frac{H_u}{2\sigma_u} \Big)(x-m)\dot{\sigma}_u dx \\
&= \frac{H_u^3}{12\sigma_u^3} \dot{\sigma}_u \\
\Rightarrow \dot{\sigma}_u &= \frac{12\sigma_u^3}{H_u^3} \langle T1, -q_x \rangle
\end{aligned} \tag{B.8}$$

which is the result found with the one-dune reduced model (Equation 3.26). The two-dune model also reproduces the results of the one-dune model for $\dot{\sigma}_u$ (Figure B.3) when run with only one dune (i.e., let $H_d = 0$; one-dune model is discussed in subsection 3.2.2).

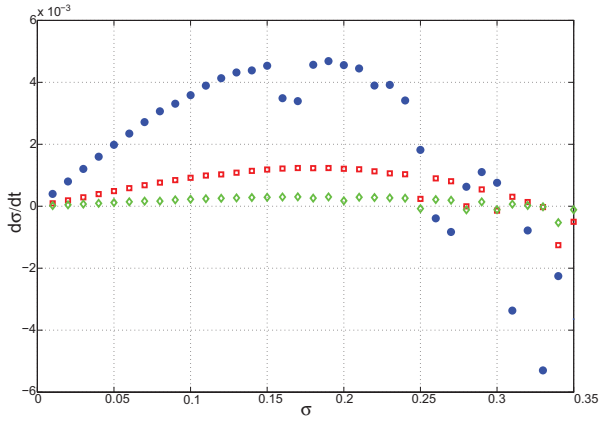

FIGURE B.3. Dynamics of windward slope as a function of slope for several different size dunes, computed using the two-dune model. Results have the same general shape and characteristics as those found with the one-dune model: Figure 3.6. Some noise is present due to small transitive variations in the dune profile.

Similarly, test function two yields:

$$\dot{\sigma}_d = \frac{12\sigma_d^3}{(H_d - \sqrt{\frac{2A_o}{1/\alpha + 1/\sigma_d}})^3} \langle T2, -q_x \rangle. \tag{B.9}$$

Test function three yields:

$$\begin{aligned}\langle T3, -q_x\rangle &= \int_{Wu}\Big(\frac{\partial h}{\partial \sigma_u}\dot{\sigma}_u + \frac{\partial h}{\partial m}\dot{m}\Big)dx \\ \Rightarrow \dot{m} &= \frac{1}{H_u}\Big(-\langle T3, -q_x\rangle + 6\frac{\sigma_u}{H_u}\langle T1, -q_x\rangle\Big). \end{aligned} \tag{B.10}$$

Note that if we have a steady windward slope on the first dune ($\dot{\sigma}_u = 0$), then we would just have:

$$\dot{m} = \frac{-\langle T3, -q_x\rangle}{H_u} = \frac{q_{\text{onto first dune's foot}} - q_{\text{out over first dune's crest}}}{H_u}$$

which is the same as that found with the one-dune model (Equation 3.28).

Test function four yields:

$$\begin{aligned}\langle T4, -q_x\rangle &= \int_{Lu}\Big(\frac{\partial h}{\partial \sigma_u}\dot{\sigma}_u + \frac{\partial h}{\partial H_u}\dot{H}_u + \frac{\partial h}{\partial m}\dot{m}\Big)dx \\ \Rightarrow \dot{H}_u &= \Big(\frac{\langle T4, -q_x\rangle}{H_u - \sqrt{\frac{2A_o}{1/\alpha + 1/\sigma_d}}} + \frac{6\sigma_u\langle T1, -q_x\rangle}{H_u^2} + \frac{\langle T3, -q_x\rangle}{H_u}\Big)/\Big(\frac{1}{\alpha} + \frac{1}{\sigma_u}\Big) \end{aligned} \tag{B.11}$$

Finally, test function five yields:

$$\begin{aligned}\langle T5, -q_x\rangle &= \int_{Ld}\Big(\frac{\partial h}{\partial \sigma_u}\dot{\sigma}_u + \frac{\partial h}{\partial \sigma_d}\dot{\sigma}_d + \frac{\partial h}{\partial H_u}\dot{H}_u + \frac{\partial h}{\partial H_d}\dot{H}_d + \frac{\partial h}{\partial m}\dot{m}\Big)dx \\ \Rightarrow \dot{H}_d &= \Big(\frac{\alpha}{H_d}\langle T5, -q_x\rangle - \frac{\partial h}{\partial \sigma_u}\dot{\sigma}_u - \frac{\partial h}{\partial \sigma_d}\dot{\sigma}_d - \frac{\partial h}{\partial H_u}\dot{H}_u - \frac{\partial h}{\partial m}\dot{m}\Big)\sigma_d \div \\ &\qquad \Big((\sigma_d + \alpha)(1 - H_d/\sqrt{\frac{2A_o}{1/\alpha + 1/\sigma_d}})\Big) \\ &= \Big(\langle T5, -q_x\rangle/H_d + \frac{12\sigma_u}{H_u^2}\Big(1 - \frac{H_u}{2\sqrt{\cdot}}\Big)\langle T1, -q_x\rangle + \\ &\qquad \frac{6\sigma_d^2}{(H_d - \sqrt{\cdot})^3}\Big(\frac{H_d^2}{\sqrt{\cdot}} - \sqrt{\cdot} + 2H_d\Big)\langle T2, -q_x\rangle \\ &\qquad -\Big(1 - \frac{H_u}{\sqrt{\cdot}}\Big)\Big(\frac{\langle T4, -q_x\rangle}{H_u - \sqrt{\cdot}} + \frac{6\sigma_u\langle T1, -q_x\rangle}{H_u^2} + \frac{\langle T3, -q_x\rangle}{H_u}\Big) - \\ &\qquad \frac{\sigma_d}{\alpha H_u}\Big(\frac{6\sigma_u\langle T1, -q_x\rangle}{H_u} - \langle T3, -q_x\rangle\Big)\Big) \div \\ &\qquad \Big(\Big(1 - \frac{H_d}{\sqrt{\cdot}}\Big)\frac{H_d(\sigma_d + \alpha)}{\alpha\sigma_d}\Big) \end{aligned} \tag{B.12}$$

With this reduced dimension simulation of binary dune collisions, coalescence occurred when the downwind dune's crest dropped onto the upwind dune's lee slope.

If this did not happen (H_d remained higher than $h \in L_u$), then ejection resulted. Tests showed that predicted dynamics were consistent with those found with the full dune evolution model (Section 5.2), but the reduced dimension simulation returned less information with regards to the ejected dune's final size. The simulation also was not simpler in use or faster, so this approach was abandoned.

C. SMOLUCHOWSKI DUNE INTERACTION STUDY

Smoluchowski coagulation equations are used to to describe the evolution of the number density P of particles of size x at a time t. This is useful when systems consist of a very large number of particles, such as within gaseous molecular interactions.

In the continuous case, the Smoluchowski equation is:

$$\frac{\partial P(x,t)}{\partial t} = \frac{1}{2}\int_0^x K(x-y,y)P(x-y,t)P(y,t)dy - \int_0^\infty K(x,y)P(x,t)P(y,t)dy,$$

where the operator (K) is known as the coagulation kernel and describes the rate at which particles of size x interact with particles of size y. The first term on the RHS of the equation corresponds to interactions which increase P(x), and the second corresponds to interactions which remove elements from P(x).

If we were able to derive the proper form of the kernel function for a dune field, we could perhaps use this framework to analyze the evolution of the number density of dunes of size m within the field.

Unfortunately, the dune field system differed from the physical systems analyzed by Smoluchowski in two key ways: interactions are asymmetric, as dunes and sediment move only downwind; secondly, dunes do not coagulate, but instead exchange mass when they collide.

Although this approach was abandoned in favor of a discrete particle model (discussed in sections 5.3), here we outline our kernel function derivation. The kernel function is a compilation of two functions: the rate (R) at which an upwind dune of mass a_{before} and a downwind dune of mass A_{before} interact, and the probability (O) that this interaction will yield a dune of size M.

C.1. Rate Function

As we have fixed a scale-invariant dune morphology, it is irrelevant if we consider dune height or area; as dune velocity is related to height, for simplicity the following relation will be given in terms of height (and height $\sim$ area$^{1/2}$). We consider interacting dunes of pre-collision height h and H. As dunes move in one direction, following the wind direction, $R(h,H) = 0$ if the upwind dune (the first argument) is smaller than the downwind dune. Assuming $h < H$, their rate of interaction will be determined by their relative velocity. In the frame of reference of the slower dune, the two dunes will interact once per time needed for the faster dune to do one orbit of the simulation box (if periodic boundary conditions are assumed). Thus, the rate of interaction is $R = 1/T$, where T is the time length of this orbit. As we are in the reference frame of the slower dune, the velocity that the faster dune is moving at is $v - V = h^{-1} - H^{-1}$

$(= a^{-1/2} - A^{-1/2})$. The distance traveled is the length of the simulation box (L), so $T = \frac{L}{v-V}$, or:

$$R = \frac{h^{-1} - H^{-1}}{L} = \frac{H - h}{LhH} \tag{C.1}$$

which is illustrated in Figure C.1.

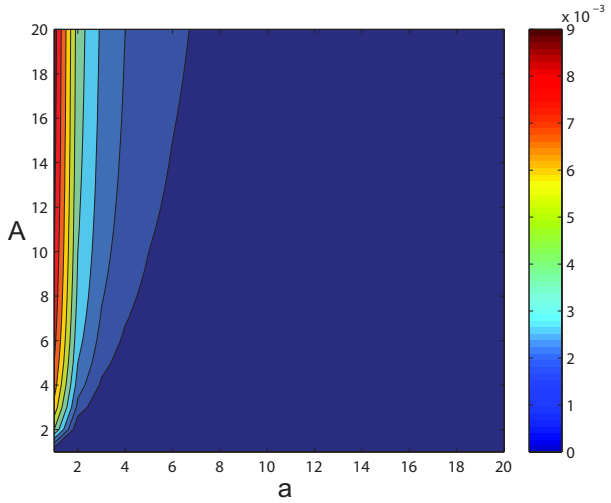

FIGURE C.1. Plot of the rate of interaction (number of collisions per unit time) between an upwind dune of size $a \sim h^2$ and a downwind dune of size $A \sim H^2$ (equation C.1).

To validate this analytical result, we counted dune collisions within randomly generated dune fields (Figure C.2). Note that this relationship is quite different from the rate function found for collisions between gas molecules (which exchange velocities), where $R \sim \frac{1}{h^2 H^2}$.

C.2. Output Function

Our output function will be in the form of a δ-function, as it will be determined based on numerical simulation of our full dune evolution model, which is deterministic. Our output function must also be a superposition of two cases, as sometimes one dune is the result of interaction (coalescence) and sometimes two dunes result (ejection). We define the following case-functions (where the a and A again refer only to the

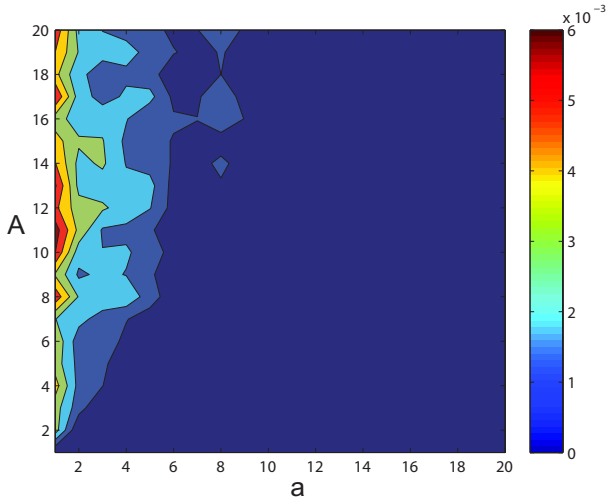

FIGURE C.2. The number of interactions (number of collisions per unit time) between an upwind dune of size a and and a downwind dune of size A, as counted within 30 simulation runs.

pre-collision sizes, and the first argument refers to the upwind dune size):

$$O_{\mathrm{c}}(a,A,M) = C_c(a,A)\delta(a+A-M) \tag{C.2}$$

$$\text{where } C_c(a,A) = \begin{cases} 1 & \text{coalescence occurs} \\ 0 & \text{ejection occurs} \end{cases} \tag{C.3}$$

$$O_{\mathrm{e}}(a,A,M) = C_e(a,A)\big(\delta(M_{\text{after, upwind}}(a_{\text{before}},A_{\text{before}})-M)+ \tag{C.4}$$

$$\delta(M_{\text{after, downwind}}(a,A)-M)\big) \tag{C.5}$$

$$\text{where } C_e(x,y) = \begin{cases} 0 & \text{coalescence occurs} \\ 1 & \text{ejection occurs} \end{cases}. \tag{C.6}$$

The full output function is, thus, $O(a,A,M) = O_c(a,A,M) + O_e(a,A,M)$. For any given a and A, the integral of O over all output dune sizes (M) yields the total number of dunes which result from the collision:

$$\int_0^\infty O(a,A,M)dM = \begin{cases} 1 & \text{coalescence occurs} \\ 2 & \text{ejection occurs} \end{cases}. \tag{C.7}$$

To determine the exact form of the output function, we need to know how the masses of two interacting dunes influences the mass(es) of the dunes which result from the interaction. To do this, we study the numerical results of many, many interactions (as discussed in subsection 5.2.1), which results in construction of a 1-to-1 interaction

function (f) between the before-collision size ratio ($r = (a_{\text{downwind}}/A_{\text{upwind}})_{\text{before}}$) and the after-collision size ratio ($s = (a_{\text{downwind}}/A_{\text{upwind}})_{\text{after}}$) (Figure 5.5). Note that $r \in (0, 1)$, but that $f(r) = s \in [0, 1)$, as if coalescence occurs $s = 0$.

We find the following expressions (where lowercase always denotes the smaller of the two dunes):

$$(a_{\text{after}}/a_{\text{before}}) = \frac{1+r}{1+s}\frac{s}{r} \tag{C.8}$$

$$(A_{\text{after}}/A_{\text{before}}) = \frac{1+r}{1+s} \tag{C.9}$$

Thus, if coalesce does not occur (i.e., $s \neq 0$), for a dune of mass M_* to result, we need an input dunes of size $a_{\text{before}} = M_* \frac{r}{s}\frac{1+s}{1+r}$, $A_{\text{before}} = M_* \frac{1+s}{s(1+r)}$ or $a_{\text{before}} = M_* \frac{r(1+s)}{1+r}$, $A_{\text{before}} = M_* \frac{1+s}{1+r}$. If coalescence does occur ($s = 0$), then to get a dune of mass M_* to result, we need $a_{\text{before}} = M_* \frac{r}{1+r}$, $A_{\text{before}} = M_* \frac{1}{1+r}$, and r less than the coalescence threshold ($= 1/3$ in our example, Figure 5.5). These expressions allow us to fully define our δ-functions, as they uniquely define the relation between the pre-collision and post-collision dune sizes.

References

Almeida, M. P., Parteli, E. J. R., Andrade, Jr., J. S. & Herrmann, H. J. (2008), 'Giant saltation on Mars', *Proceed. Nat. Acad. Sci.* **105**(17), 6222–6226.

Andreotti, B., Antoine Fourrière, A., Ould-Kaddour, F., Murray, B. & Claudin, P. (2009), 'Giant aeolian dune size determined by the average depth of the atmospheric boundary layer', *Nature* **457**, 1120–1123.

Andreotti, B., Claudin, P. & Douady, S. (2002*a*), 'Selection of dune shapes and velocities, Part 1: Dynamics of sand, wind, and barchans', *Europ. Phys. J. B* **28**, 321–339.

Andreotti, B., Claudin, P. & Douady, S. (2002*b*), 'Selection of dune shapes and velocities, Part 2: A two-dimensional modeling', *Europ. Phys. J. B* **28**, 341–325.

Baddock, M. C., Livingstone, I. & Wiggs, G. F. S. (2007), 'The geomorphological significance of airflow patterns in transverse dune interdunes', *Geomorph.* **87**, 322–336.

Bagnold, R. A. (1941), *The physics of blown sand and desert dunes*, Methuen.

Besler, H. (2002), 'Complex barchans in the Libyan Desert: dune traps or overtaking solitons?', *Zeitschrift für Geomorph. Suppl.* **126**, 59–74.

Besler, H. (2005), The granulometric evolution of aeolian sands – an empirical and statistical approach, *in* R. Garcia-Rojo, H. J. Hermann & S. McNamara, eds, 'Proceedings of Powders and Grains', pp. 973–976.

Besler, H. (2008), *The Great Sand Sea in Egypt: Formation, dynamics and environmental change – a sediment-analytical approach*, Vol. 59 of *Develop. Sediment.*, Elsevier, chapter 4. The granulometric analysis.

Bishop, M. A. (2001), 'Seasonal variation of crescentic dune morphology and morphometry, Strzelecki-Simpson desert, Australia', *Earth Surf. Process. Landforms* **26**, 783–791.

Bishop, M. A. (2007), 'Point pattern analysis of north polar crescentic dunes, Mars: A geography of dune self-organization', *Icarus* **191**, 151–157.

Bishop, S. R., Momiji, H., Carretero-Gonzàlez, R. & Warren, A. (2002), 'Modelling desert dune fields based on discrete dynamics', *Discr. Dyn. Nature and Soc.* **7**(1), 7–17.

Bouchaud, J. P., Cates, M. E., Prakash, J. R. & Edwards, S. F. (1994), 'A model for the dynamics of sandpile surfaces', *J. Phys. I* **4**, 1383–1410.

Bourke, M. C. (2005), Alluvial Fans on Dunes in Kaiser Crater Suggest Niveo-Aeolian and Denivation Processes on Mars, *in* 'Lunar Planet. Sci. Conf. Abstracts', p. 2373.

Bourke, M. C. & Balme, M. (2008), Megabarchans on Mars, *in* 'Planet. Dunes Workshop', pp. 17–18.

Bourke, M. C., Balme, M., Beyer, R. A., Williams, K. K. & Zimbelman, J. (2006), 'A comparison of methods used to estimate the height of sand dunes on Mars', *Geomorph.* **81**, 440–452.

Bourke, M. C., Balme, M. & Zimbelman, J. (2004), A comparative analysis of barchan dunes in the intra-crater dune fields and the North Polar Sand Sea, *in* 'Lunar Planet. Inst, Sci. Conf. Abstracts', p. 1453.

Bourke, M. C., Bullard, J. E. & Barnouin-Jha, O. S. (2004), 'Aeolian sediment transport pathways and aerodynamics at troughs on Mars', *J. Geophys. Res.* **109**, E07005.

Bourke, M. C., Ewing, R. C., Finnegan, D. & McGowan, H. A. (2009), 'Sand dune movement in the Victoria Valley, Antarctica', *Geomorph.* **109**, 148–160.

Bristow, C. S., Augustinus, P. C., Wallis, I. C., Jol, H. M. & Rhodes, E. J. (2010), 'Investigation of the age and migration of reversing dunes in Antarctica using GPR and OSL, with implications for GPR on Mars', *Earth Planet. Sci. Lett.* **289**, 30–42.

Bristow, C. S., Jol, H. M., Augustinus, P. & Wallis, L. (2009), 'Slipfaceless 'whaleback' dunes in a polar desert, Victoria Valley, Antartica: Insights from ground penetrating radar', *Geomorph.* **114**, 361–372.

Bullard, J. (1997), 'A note on the use of the "Fryberger Method" for evaluating potential sand transport by wind', *J. Sediment. Res.* **67**, 499–501.

Burkinshaw, J. R., Illenberger, W. K. & Rust, I. C. (1993), 'Wind-speed profiles over a reversing transverse dune', *Geological Soc., special edition* **72**, 25–36.

Byrne, S., Dundas, C. M., Kennedy, M. R., Mellon, M. T., McEwen, A. S., Cull, S. C., Daubar, I. J., Shean, D. E., Seelos, K. D., Murchie, S. L., Cantor, B. A., Arvidson, R. E., Edgett, K. S., Reufer, A., Thomas, N., Harrison, T. N., Posiolova, L. V. & Seelos, F. P. (2009), 'Distribution of Mid-Latitude Ground Ice on Mars from New Impact Craters', *Science* **325**, 1674–1676.

Calkin, P. E. & Rutford, R. H. (1974), 'The sand dunes of Victoria Valley, Antartica', *Geograph. Rev.* **64**(2), 189–216.

Claudin, P. & Andreotti, B. (2006), 'A scaling law for aeolian dunes on Mars, Venus, Earth, and for subaqueous ripples', *Lunar and Planetary Science Letters* .

Cook, R. U., Warren, A. & Goudie, A. S. (1993), *Desert Geomorphology*, UCL Press.

Cooke, R., Warren, A. & Goudie, A. (1993), *Desert geomorphology*, UCL Press Limited.

Diniega, S., Glasner, K. & Byrne, S. (2010), 'Long-time evolution of models of aeolian sand dune fields: Influence of dune formation and collision', *Geomorph.* **121**, 55–68. Special Issue: Planet. Dune Systems.

Durán, O. & Herrmann, H. J. (2006), 'Modelling of saturated sand flux', *J. Stat. Mech.* p. P07011.

Durán, O., Schwämmle, V. & Herrmann, H. J. (2005), 'Breeding and solitary wave behavior of dunes', *Phys. Rev. E* **72**, 021308.

Edgett, K. S. & Christensen, P. R. (1991), 'The particle size of martian aeolian dunes', *J. Geophys. Res.* **96**, 22765–22776.

Elbelrhiti, H., Andreotti, B. & Claudin, P. (2008), 'Barchan dune corridors: field characterization and investigation of control parameters', *J. Geophys. Res.* **113**, F02S15.

Elbelrhiti, H., Claudin, P. & Andreotti, B. (2005), 'Field evidence for surface-wave-induced instability of sand dunes', *Nature* **437**, 720–722.

Endo, N., Kobu, H. & Sunamura, T. (2004), 'Barchan-shaped ripple marks in a wave flume', *Earth Surf. Process. Landforms* **29**, 31–42.

Endo, N., Taniguchi, K. & Katsuki, A. (2004), 'Observation of the whole process of interaction between barchans by flume experiments', *Geophys. Res. Lett.* **31**, L12503.

Ewing, R. & Kocurek, G. (2010), 'Aeolian dune interactions and dune-field pattern formation: White Sands Dune Field, New Mexico', *Sediment.* .

Feldman, W. C., Bourke, M. C., Elphic, R. C., Maurice, S., Bandfield, T. H., Prettyman, T. H., Diez, B. & Lawrence, D. J. (2008), 'Hydrogen content of sand dunes in Olympia Undae', *Icarus* **196**, 422–432.

Fenton, L. K., Toigo, A. D. & Richardson, M. I. (2005), 'Aeolian processes in Proctor crater on Mars: Mesoscale modeling of dune-forming winds', *J. Geophys. Res.* **110**, E06005.

Frank, A. & Kocurek, G. (1996*a*), 'Airflow up the stoss slope of sand dunes: limitations of current understanding', *Geomorph.* **17**, 47–54.

Frank, A. & Kocurek, G. (1996*b*), 'Toward a model for airflow on the lee side of aeolian dunes', *Sediment.* **43**, 451–458.

Fryberger, H. (1979), *Dune forms and wind regime*, Professional Paper 1052, U.S. Geological Survey, pp. 137–169.

Fryberger, S. G., Al-Sari, A. M., Clisham, T. J., Rizvi, S. A. R. & Al-Hinai, K. G. (1984), 'Wind sedimentation in the Jafurah sand sea, Saudi Arabia', *Sediment.* **31**, 413–431.

Gay, S. P. (1999), 'Observations regarding the movement of barchan sand dunes in the Nazca to Tanaca area of southern Peru', *Geomorph.* **27**, 279–293.

Gaylord, D. R. & Dawson, P. J. (1987), 'Airflow-terrain interactions through a mountain gap, with an example of eolian activity beneath an atmospheric hydraulic jump', *Geology* **15**, 789–792.

Greeley, R., Arvidson, R. E., Elachi, C., Geringer, M. A., Plaut, J. J., Saunders, R. S., Schubert, G., Stofan, E. R., Thouvenot, E. J. P. & Wall, S. D. (1992), 'Aeolian features on Venus – Preliminary Magellan results', *J. Geophys. Res.* **97**, 13319–13345.

Greeley, R., Kuzmin, R. O., Rafkin, S. C. R., Michaels, T. I. & Haberle, R. (2003), 'Wind-related features in Gusev crater, Mars', *J. Geophys. Res.* **108**(E12), 18–+.

Greeley, R., Leach, R., White, B., Iversen, J. & Pollack, J. (1980), 'Threshold windspeeds for sand on Mars: Wind tunnel simulations', *J. Geophys. Res.* **7**, 121–124.

Hansen, C. J., McEwen, A., Okubo, C., Bridges, N., Byrne, S., Gulick, V., Herkenhoff, K., Kolb, K., Mellon, M., Russel, P. & the HiRISE Team (2007), HiRISE observations of Mars' southern seasonal frost sublimation, *in* 'Lunar Planet. Inst, Sci. Conf. Abstracts', p. 1906.

Hayward, R. K., Titus, T. N., Michaels, T. I., Fenton, L. K., Colaprete, A. & Christensen, P. R. (2009), 'Aeolian dunes as ground truth for atmospheric modeling on Mars', *J. Geophys. Res.* **114**(E13), 11012.

Herrmann, H. J., Durán, O., Parteli, E. J. R. & Schatz, V. (2008), 'Vegetation and induration as sand dunes stabilizators', *J. Coastal Res.* **24**(6), 1357–1368.

Herrmann, H. J., Sauermann, G. & Schwämmle, V. (2005), 'The morphology of dunes', *Physica A* **358**, 30–38.

Hersen, P. (2004), 'On the crescentic shape of barchan dunes', *Europ. Phys. J. B* **37**, 507–514.

Hersen, P., Andersen, K. H., Elbelrhiti, H., Andreotti, B., Claudin, P. & Douady, S. (2004), 'Corridors of barchan dunes: stability and size selection', *Phys. Rev. E* **69**(1), 011304.

Hersen, P. & Douady, S. (2005), 'Collision of barchan dunes as a mechanism of size regulation', *Geophys. Res. Lett.* **32**, L21403.

Hesp, P. A. & Hastings, K. (1998), 'Width, height, and slope relationships and aerodynamic maintenance of barchans', *Geomorph.* **22**, 193–204.

Horgan, B., Bell, J. F. & Bourke, M. C. (2010), Dry Flow, Surface Cementation, and Ice Induration Features on Dunes in the North Polar Region of Mars, *in* 'Lunar Planet. Sci. Conf. Abstracts', Vol. 41, p. 1325.

Howard, A. D., Morton, J. B., Gad-el-hak, M. & Pierce, D. B. (1978), 'Sand transport model of barchan dune equilibrium', *Sediment.* **25**, 307–338.

Iversen, J. D. & Rasmussen, K. D. (1999), 'The effect of wind speed and bed slope on sand transport', *Sediment.* **46**, 723–731.

Iversen, J. D. & White, B. R. (1982), 'Saltation threshold on Earth, Mars, and Venus', *Sediment.* **29**, 111–119.

Jackson, P. S. & Hunt, J. C. R. (1975), 'Turbulent wind flow over a low hill', *Quarter. J. Royal Meteor. Soc.* **101**(430), 929–955.

Katsuki, A., Kikuchi, M. & Endo, N. (2005), 'Emergence of a barchan belt in a unidirectional flow: Experiment and numerical simulation', *J. Phys. Soc. Japan* **74**(3), 878–881.

Katsuki, A., Nishimori, H., Endo, N. & Taniguchi, K. (2005), 'Collision dynamics of two barchan dunes simulated using a simple model', *J. Phys. Soc. Japan* **74**(2), 538–541.

Kocurek, G. & Ewing, R. C. (2005), 'Aeolian dune field self-organization – implications for the formation of simple versus complex dune-field patterns', *Geomorph.* **72**, 94–105.

Kok, J. F. (2010), 'Difference in the Wind Speeds Required for Initiation versus Continuation of Sand Transport on Mars: Implications for Dunes and Dust Storms', *Phys. Rev. Lett.* **104**(7), 074502–+.

Koster, E. & Dijkmans, J. W. (1988), 'Niveo-aeolian deposits and denivation forms, with special reference to the Great Kobuk Sand Dunes, Northwestern Alaska', *Earth Surf. Proc. Landforms* **13**, 153–170.

Kroy, K., Sauermann, G. & Herrmann, H. J. (2002), 'Minimal model for aeolian sand dunes', *Phys. Rev. E* **66**(3), 031302–1 – 18.

Lancaster, N. (1985), 'Variations in wind velocity and sand transport on the windward flacks of desert sand dunes', *Sediment.* **32**, 581–593.

Lancaster, N. (1988), 'Variations in wind velocity and sand transport on the windward flacks of desert sand dunes', *Geology* **16**, 972–975.

Lancaster, N. (1995), *Geomorphology of desert dunes*, Routledge.

Lee, J. H., Sousa, A. O., Parteli, E. J. R. & Herrmann, H. J. (2005), 'Modelling formation and evolution of transverse dune fields', *Internat. J. Mod. Physics C* **16**, 1879–1892.

Lettau, K. & Lettau, H. H. (1978), *Experimental and micometeorological studies of dune migration*, University of Wisconsin Institute of Environmental Sciences, pp. 110–147.

Lima, A. R., Sauermann, G., Herrmann, H. J. & Kroy, K. (2002), 'Modelling a dune field', *Physica A* **310**, 487–500.

Lindsay, J. F. (1973), 'Reversing barchans in Lower Victoria Valley, Antarctica', *Geological Soc. Am. Bull.* **84**, 1799–1806.

Livingstone, I., Wiggs, G. F. S. & Baddock, M. (2005), 'Barchan dunes: why they cannot be treated as 'solitons' or 'solitary waves'', *Earth Surf. Process. Landforms* **30**, 255–257.

Lorenz, R. D., Wall, S. & 38 coauthors (2006), 'The sand seas of Titan: Cassini RADAR observations of longitudinal dunes', *Science* **312**, 724–727.

Miyamoto, H., Dohm, J. M., Baker, V. R., Beyer, R. A. & Bourke, M. (2004), 'Dynamics of unusual debris flows on Martian sand dunes', *Geophys. Res. Lett.* **31**, L13701.

Momiji, H. (2001), Mathematical modelling of the dynamics and morphogy of aeolian dunes and dune fields, PhD dissertation, University College London.

Momiji, H., Carretero-González, R., Bishop, S. R. & Warren, A. (2000), 'Simulation of the effect of wind speedup in the formation of transverse dunes', *Earth. Surf. Process. Landforms* **25**, 905–918.

Momiji, H. & Warren, A. (2000), 'Relations of sand trapping efficiency and migration speed of tranvsverse dunes to wind velocity', *Earth. Surf. Process. Landforms* **25**, 1069–1084.

Ni, J., Li, Z. & Mendoza, C. (2004), 'Blown sand transport rate', *Earth. Surf. Process. Landforms* **29**, 1–14.

Nickling, W. G., Mckenna Neuman, C. & Lancaster, N. (2004), 'Grainfall processes in the lee of transverse dunes, Silver Peak, Nevada', *Sediment.* **49**, 191–209.

Owen, P. R. (1964), 'Saltation of uniform grains in air', *J. Fluid Mech.* **20**(2), 225–242.

Palmer, J. (2010), The flow structure of interacting barchan dunes, Masters dissertation, University of Illinois at Urbana-Champaign.

Parsons, D. R., Walker, I. J. & Wiggs, G. F. S. (2004), 'Numerical modelling of flow structures over idealized transverse aeolian dunes of varying geometry', *Geomorph.* **59**, 149–164.

Parteli, E. & Herrmann, H. J. (2003), 'A simple model for a tranverse dune field', *Physica A* **327**, 554–562.

Parteli, E. J. & Herrmann, H. J. (2007), 'Dune formation on the present Mars', *Phys. Rev. E* **76**, 041307–1–16.

Parteli, E. J. R., Durán, O. & Herrmann, H. J. (2006), The shape of the barchan dunes in the Arkhangelsky Crater on Mars, *in* 'Lunar Planet. Sci. Conf. Abstracts', p. 1827.

Parteli, E. J. R., Schatz, V. & Herrmann, H. J. (2005), Barchan dunes on Mars and on Earth, *in* R. Garcia-Rojo, H. J. Herrmann & S. McNamara, eds, 'Proceedings of Powders and Grains', pp. 959–962.

Parteli, E. J. R., Schwämmle, V., Herrmann, H. J., Monteiro, L. H. U. & Maia, L. P. (2005), 'Profile measurement and simulation of a transverse dune field in the Lençóis Maranheses', *Internat. J. Mod. Phys. C* **16**, 1879–1892.

Pelletier, J. D. (2009), 'Controls on the height and spacing of eolian ripples and transverse dunes: A numerical modeling investigation', *Geomorph.* **105**, 322–333.

Perron, J. T., Dietrich, W. E., Howard, A., McKean, J. A. & Pettinga, J. R. (2003), 'Ice-driven creep on martian debris slopes', *Geophys. Res. Lett.* **30**, 1747.

Radebaugh, J., Lorenz, R. D., Lancaster, N., Savage, C. J., Wall, S. D., Stofan, E. R., Lunine, J. I., Kirk, R. L. & Le Gall, A. (2010), Winds and Sand Transport Patterns on Titan from Dune Interactions with Topography, *in* 'Lunar Planet. Inst, Sci. Conf. Abstracts', p. 2513.

Radebaugh, J., Lorenz, R. D., Lunine, J. I., Wall, S. D., Boubin, G., Reffet, E., Kirk, R. L., Lopes, R. M., Stofan, E. R., Soderblom, L., Allison, M., Janssen, M., Paillou, P., Callahan, P., Spencer, C. & The Cassini Radar Team (2008), 'Dunes on Titan observed by Cassini Radar', *Icarus* **194**, 690–703.

Reffet, E., Courrech du Pont, S., Hersen, P. & Douady, S. (2010), 'Formation and stability of transverse and longitudinal sand dunes', *Geology* **38**, 491–494.

Sauermann, G., Andrade Jr., J. S., Maia, L. P., Costa, U. M. S., Araùjo, A. D. & Herrmann, H. J. (2003), 'Wind velocity and sand transport on a barchan dune', *Geomorph.* **1325**, 1–11.

Sauermann, G., Kroy, K. & Herrmann, H. J. (2001), 'Continuum saltation model for sand dunes', *Phys. Rev. E* **64**(3), 031305–1–10.

Schatz, V. & Herrmann, H. J. (2006), 'Flow separation in the lee side of transverse dunes: A numerical investigation', *Geomorph.* **81**, 207 – 216.

Schwämmle, V. & Herrmann, H. J. (2004), 'Modelling transverse dunes', *Earth Surf. Process. Landforms* **29**, 769–784.

Schwämmle, V. & Herrmann, H. J. (2005), 'A model of barchan dunes including lateral shear stress', *Europ. Phys. J. E* **16**, 57–65.

Selby, M. J., Rains, B. B. & Palmer, R. W. P. (1974), 'Eolian deposits of the ice-free Victoria Valley, southern Victoria Land, Antarctica', *New Zealand J. Geo. Geophys.* **17**, 543–562.

Sorensen, M. (2004), 'On the rate of aeolian sand transport', *Geomorph.* **59**, 53–62.

Stam, J. M. T. (1996), 'Migration and growth of aeolian bedforms', *Math. Geology* **28**, 519–536.

Steidtmann, J. R. (1973), 'Ice and snow in eolian sand duns of southwestern Wyoming', *Science* **179**(4075), 796–798.

Sullivan, R., Arvidson, R., Bell, J. F., Gellert, R., Golombek, M., Greeley, R. an dHerkenhoff, K., Johnson, J., Thompson, S. & Whelley, P. an dWray, J. (2008), 'Wind-driven particle mobility on Mars: INsights from Mars exploration Rover observations at "Eldorado" and surroundings at Gusev Crater', *J. Geophys. Res.* **113**, E06S07.

Sweet, M. L. & Kocurek, G. (1990), 'An empirical model of aeolian dune lee-face airflow', *Sediment.* **37**, 1023–1038.

Uno, I., Eguchi, K., Yumimoto, K., Takemura, T., Shimizu, A., Uematsu, M., Liu, Z., Wang, Z., Hara, Y. & Sugimoto, N. (2009), 'Asian dust transported one full circuit around the globe', *Nat. Geosci.* **2**, 557–560.

van Dijk, P. M., Arens, S. M. & van Boxel, J. H. (1999), 'Aeolian processes across transverse dunes. II: Modeling the sediment transport and profile development', *Earth Surf. Process. Landforms* **24**, 319–333.

Walker, I. J. & Nickling, W. G. (2002), 'Dynamics of secondary airflow and sediment transport over and in the lee of transverse dunes', *Progr. Phys. Geo.* **26**(1), 47–75.

Walker, I. J. & Nickling, W. G. (2003), 'Simulation and measurement of surface shear stress over isolated and closely spaced transverse dunes in a wind tunnel', *Earth Surf. Process. Landforms* **28**, 1111–1124.

Wang, X., Dong, Z., Zhang, J., Qu, J. & Zhao, A. (2003), 'Grain size characteristics of dune sands in the central Taklimakan Sand Sea', *Sediment. Geo.* **161**, 1–14.

Weng, W. S., Hunt, J. C. R., Carruthers, D. J., A., W., Wiggs, G. F. S., Livingstone, I. & Castro, I. (1991), 'Air flow and sand transport over sand-dunes', *Acta Mech. Suppl.* **2**(1), 1–22.

Werner, B. T. (1995), 'Eolian dunes: computer simulations and attractor interpretation', *Geology* **23**, 1107–1110.

Werner, B. T. (1999), 'Complexity in natural landform patterns', *Science* **284**, 102–104.

Wiggs, G. F. S. (2001), 'Desert dune processes and dynamics', *Progress in Phys. Geography* **25**, 53–79.

Wiggs, G. F. S., Bullard, J. E., Garvey, B. & Castro, I. (2002), 'Interactions between airflow and vally topography with implications for aeolian sediment transport', *Phys. Geography* **23**, 366–380.

Wilkins, D. E. & Ford, R. L. (2007), 'Nearest neighbor methods applied to dune field organization: The Coral Pink Sand Dunes, Kane County, Utah, USA', *Geomorph.* **83**, 48–57.